Studies on Mechanical, Electrical and Thermal Properties of AlN-SWCNT Composite

Ph.D. Thesis

Ravindra Singh

(2014RMT9519)

December 2019

Department of Metallurgical and Materials Engineering
Malaviya National Institute of Technology Jaipur
Jaipur-302017
INDIA

Studies on Mechanical, Electrical and Thermal Properties of AlN-SWCNT Composite

This thesis is submitted as a partial fulfillment of
the Ph.D. Programme in Engineering

Submitted By:

Ravindra Singh

(2014RMT9519)

Under the supervision of

Prof. U. Pandel

(Supervisor)

Prof. S.K. Biswas

(Co-Supervisor EXT.)

December 2019

Department of Metallurgical and Materials Engineering
Malaviya National Institute of Technology Jaipur
Jaipur-302017

DECLARATION

I, **Ravindra Singh** declare that this thesis titled, **"Studies on Mechanical, Electrical and Thermal Properties of AlN-SWCNT Composite"** and the work presented in it, are my own. I confirm that:

- This work was done wholly or mainly while in candidature for a research degree at this university.

- Where any part of this thesis has previously been submitted for a degree or any other qualification at this institute or any other institution, this has been clearly stated.

- Where I have consulted the published work of others, this is always clearly attributed.

- Where I have quoted from the work of others, the source is always given. With the exception of such quotations, this thesis is entirely my own work.

- I have acknowledged all main sources of help.

- Where the thesis is based on work done by myself, jointly with others, I have made clear exactly what was done by others and what I have contributed myself.

Date:

Place:

Ravindra Singh

(2014RMT9519)

ACKNOWLEDGEMENTS

First and foremost, I have to thank my parents **Mr. Karan Singh** and **Mrs. Mahendra Devi** for their love and support throughout my life. Thank you both for giving me strength to reach for the stars and chase my dreams. My elder brother **Mr. Virendra Singh** and my Sister in law **Mrs. Avinash** who has always put in their best in supporting my ambition and have also proved to be a great motivating factor in overcoming many obvious hindrances and helping me to achieve the desired result. I also dedicate this Ph.D. thesis to my lovely nephew **Ryan**, the pride and joy of my life. I love you more than anything and I appreciate all your patience and support during my Ph.D. studies.

I wish to express my deep regards and a profound sense of gratitude to my reverend and learned supervisor **Prof. Upender Pandel**, Department of Metallurgical and Materials Engineering, Malaviya National Institute of Technology Jaipur, who through his excellent guidance has enabled me to accomplish this work

I wish to express my deep sense of gratitude to my Co- Supervisor (External), **Ex. Prof. Sampad Kumar Biswas**, Department of Metallurgical and Materials Engineering, Malaviya National Institute of Technology, Jaipur under whose supervision and able guidance I had the privilege to carry out my research work. He has been a great source of inspiration for me, all through. I am very grateful to him for guiding me on how to conduct research and how to clearly & effectively present the work done. I am deeply indebted to him for valuable suggestions, sustained encouragement, and inspiration which I received from time to time.

I would like to express my sincere thanks to **Dr. V. K. Sharma, Dr. R. K. Duchaniya** and **Dr. V. N. Nadakuduru** for being my DREC committee as well as for their encouragement, analytical insights, and recommendations.

I would like to express my sincere thanks to **Dr. R.K. Duchaniya (DPGC convener)** for all the encouragement and recommendations to accomplish this work.

I wish to thank **Dr. Dipayan Sanyal** Chief Scientist and **Dr. Dipten Bhattacharya**, Senior Principal Scientist, CSIR-CGCRI, Kolkata for their kind helps in using the

facility of non-oxide ceramics and electrical characterisation respectively and advice on the analysis of the results.

I express my deep appreciation to my friends and co-worker **Mr. Sandeep Dhaka, Mr. Ravindra Singh Shekhawat, Ms. Versha Goyal, Ms. Nitika Kundan, Mr. Ankit Goyal, Mr. Arun Kumar, Mr. Mrigesh Verma, Mr. Prashant Dhakar** and **Mr. Mukesh Kumar** from MNIT, Jaipur campus and **Dr. Amrita Chakravarty, Dr. Ujjal Chowdhury and Mr. Shubhankar Mishra** from CSIR-CGCRI, Kolkata.

MNIT Jaipur for providing scholarship and sponsorship of the work, to all my colleagues and staff of Department of MME and MRC for helping to carry out the work.

To all my friends, thank you for your understanding and encouragement in moments of crisis. Your friendship makes my life a wonderful experience.

Ravindra Singh

This thesis is dedicated to my family.

My Father Mr. Karan Singh

My Mother Mrs. Mahendra Devi

My Elder Brother Mr. Virendra Singh

My Sister in law Mrs. Avinash

My lovely Nephew Ryan

For their endless love, support and encouragement

ABSTRACT

Multifunctional properties of the 1D Single Walled Carbon Nanotube (SWCNT) and interesting properties of Aluminum Nitride (AlN) had been used to explore the mechanical, electrical & thermal properties of novel AlN-SWCNT composites prepared by powder technological method. The thesis will deliberate on a glimpse of the fascinating properties of AlN – SWCNT composites containing 1, 3 and 6vol% SWCNTs prepared by hot pressing method at 1850^{o}C under N_2 atmosphere and 35 MPa pressure with a dwell of 40 minutes using a graphite die and punch. Considerable fracture toughness (K_{IC}) (5MPa.m$^{1/2}$), thermal (62W/m.K) and electrical (200S/m) conductivities and high negative permittivity have been observed in the highly dense AlN-6vol% SWCNT composite. Densification and less grain growth was observed with SWCNT incorporation. Raman spectra were recorded and used to show the survivability of the SWCNTs and perform an assessment of the residual stress within the composite. Hardness and fracture toughness (K_{IC}) were determined by Vicker's indentation. Microstructures analyses by FESEM and TEM show highly connected 3D networks in the grain boundaries. An initial increase in hardness of the composite on 1vol% CNT addition and subsequent decrease on further addition of SWCNTs were observed. Fracture toughness increased by almost 60% (5MPa.m$^{1/2}$) on addition of 6vol% SWCNTs in AlN. Crack deviation along grain boundaries, uncoiling of and crack bridging by nanotubes are being proposed to be the toughening mechanisms of the composites. A residual stress analysis of ASN-6 sample has been carried out with Raman spectra of the polished surface to see the changes on the surface after a Vicker's indentation. Thermal conductivities of the composites show a downward trend with the concentration of SWCNTs in the material. Analysis on the results on electrical conductivities of the nanocomposites has established both variable range hopping and fluctuation induced tunneling among the two modes of carrier transports in the composites. AC impedances and dielectric properties of the composites revealed the presence of tunable negative permittivities in the composites in the radio frequency range between 10MHz to 1GHz.

TABLE OF CONTENTS

LIST OF FIGURES

Figure number with caption **Page No.**

LIST OF TABLES

LIST OF ABBREVIATIONS

AlN	Aluminum Nitride
SWCNT	Single-walled Carbon Nano Tube
MWCNT	Multi-walled Carbon Nano Tube
XRD	X-Ray diffraction
SEM	Scanning electron microscopy
EDS	Energy dispersive X-ray spectroscopy
TEM	Transmission electron microscopy
SAED	Selected area electron diffraction

Chapter 1

Introduction

1.1.Background

Aluminum Nitride (AlN) is a very important ceramics having high thermal conductivity (310W/mK) [1], low thermal expansion co-efficient (CTE), reasonable high temperature strength, low electrical conductivity, dielectric constant and loss which warranted its applications as heat dissipating but electrically insulating substrates in very large integrated circuits (VLSI), window materials for microwave and electron tubes and handling device for plasma display panels (PDPs) [2] apart from refractory applications like components for Aluminum casting. It has also many interesting mechanical properties like brittle to ductile transition at a moderately low confining pressure, absorption of high impact energy with phase change which led to its application in armor [2,3]. However, the principal drawback of AlN ceramic is its possession of low strength (300MPa), fracture toughness ($3MPa.m^{1/2}$) and hardness (10GPa) [4]. Efforts are, therfore, being made to improve the mechanical properties of AlN based materials by the addition of particulates like TiN, TiB_2, SiC, Mo etc with high young's modulus and CTE [4–7] to create thermal microstress in the material for the enhancement of fracture toughness. These particulates are electrically conducting and, therefore, the composites prepared from them have increased electrical conductivity and dielectric loss. Electrical properties of AlN ceramics are very interesting. It is a wide bandgap (5.34eV) semiconducor and has a peizoelectric relaxation frequency from 280MHz to 2GHz [8,9].

Carbon Nanotube (CNT), on the other hand, is one of the recently discovered allotropic forms of carbon which can be classified as single wall carbon nanotubes (SWCNT) and multiwall carbon nanotubes (MWCNT) depending on the number of concentric tubes in their structures. Properties of SWCNTs are superior to those of MWCNTs in many respects such as Young's Modulus, tensile strength, electrical and thermal conductivities [10–17]. Single walled carbon nanotubes (SWCNTs) offer exceptional transport properties in the 1-D nanostructure to the maximum extent among all the varieties of carbon nanotubes and possess high electrical conductivity

(10^6 $S.m^{-1}$) [13] exceptionally high thermal conductivity (6.6 $kWm^{-1}K^{-1}$) [18], elastic moduli (1 TPa) [19] and tensile strength (22 GPa) [20]. Moreover, CNTs are resistant to plasmas[21]. SWCNTs can be metallic or semiconducting in nature depending on the chirality of their structures [19]. Separation of the tubes is needed in addition to purification since as-synthesized SWCNTs contain both metallic and semiconducting varieties as well as huge quantities of amorphous carbon [22]. Metallic SWCNTs possess quasi ballistic transport behaviour with excellent current carrying capacity and the current across different parts of the nanotube is uniform [23]. It has been observed that SWCNT possesses negative permittivity in a wide frequency range and, therefore, considered as metamaterial [24].

The incorporation of CNTs in different ceramic matrices are, therefore, being looked into worldwide since significant improvements in the properties of the composites are achieved by very little addition. However, the mechanism of improvement in properties has not yet been fully understood. Although present state-of-the-art researches have indicated the potential of these CNT containing nanocomposites in many important device applications but, at the same time, illustrated the significant challenges involved in processing of these composites and subsequent achievement of the improved properties [14]. The principal hurdle in processing these composites is the difficulty encountered in the dispersion of the CNTs due to strong attractive van der waals force present among these tubes [25] and the isolation of a particular variety of tubes. Another important difficulty is the purification of the as- synthesized tubes before incorporation into the ceramics by powder processing technique. Lastly, it is very difficult for the tubes to survive during the high temperature sintering step required for the preparation of the composite.

Most of the studies were devoted to prepare and explore the properties of CNT containing nanocomposites of Al_2O_3, Si_3N_4, SiC, MgO, SiO_2 and glass-ceramics. Most of these composites contained MWCNT presumably due to the low cost of these tubes. Spark plasma sintering involving rapid heating technique had been used in most of the studies to minimize the destruction of the tubes at high temperature. No study could be traced in the open literature on the preparation and properties of AlN-SWCNT nanocomposite.

1.2. Objective of the research project

Main objective of the present study is, therefore, to explore the electrical, thermal and mechanical properties of a novel AlN-SWCNT ceramic nanocomposite and find out the mechanism of variation of properties by altering the SWCNT content from 0 to 6 vol%. The SWCNTs were purified and simultaneously enriched with metallic variety tubes before incorporation and dispersion in ceramics. Conventional hot pressing technique has been used in the present study so that a scaling operation could be used in future to manufacture the composite in larger dimensions. The properties studied include mechanical (hardness and fracture toughness), electrical (dc conductivity, dielectric properties with frequencies), thermal (thermal conductivity and thermoelectric power). The thesis, thus, is intended to present how the nanoscale structure of SWCNT influences the bulk properties of the material with special emphasis on metallic nanotube contents.

The thesis also addresses the challenges behind the fabrication of AlN-SWCNT nanocomposites and encountered with the difficulties in handling both AlN and SWCNTs considering the easy hydrolysis of AlN powder under ambient atmosphere and the dispersion of SWCNTs in any medium.

Chapter 2

Literature Review

2.1. Aluminum Nitride

The existence of AlN was discovered in 1862 by F. Briegler and A. Geuther and the first synthesis was realized by J.W. Mallets in 1877 [26]. In 1956 Kohn and associates of U.S. Bureau of Mines incidently obtained small crystals of aluminum nitride while working at high temperature and reported that these crystals were inert to hot and cold mineral acid and alkali solutions. These results show a good potential of aluminum nitride as a refractory material [27].

In 1985-88, the concerns related to heat dissipation of electronic circuits appeared wherein AlN was used in microelectronic packaging, which needs oxidative and hydrolytic stability, thermal conductivity, and cost. High-Quality AlN substrates for packaging purpose emerged in the early 1990s replacing highly toxic BeO. Also, multilayer AlN packaging has been extended and offers an alternative for power purposes. The current state of AlN is more than 20 companies worldwide are developing AlN technology [1,26,28–33].

2.1.1. Properties of AlN

- AlN is resistant to attack by most molten metals, most notably aluminium, lithium and copper.
- It is also resistant to attack from most molten salts including chlorides and cryolite.
- High thermal conductivity for a ceramic material (second only to beryllia)
- High volume electrical resistivity
- High dielectric strength
- It is not attacked by acids and alkalis
- It is susceptible to rapid hydrolysis by water or humidity in the powder form

Some important properties of AlN is presented in **Table 2.1** below.

Table 2.1. Properties of AlN.

Property	
Density ($g.cm^{-3}$)	3.25- 3.34
Modulus of rupture (MPa)	300-350
Modulus of elasticity (GPa)	310
Fracture toughness ($MPa.m^{-1/2}$)	3.35
Compressive strength (MPa)	2070
Hardness (GPa)	11
Coeff of thermal expansion RT- 1000°C ($x10^{-6}$ K^{-1})	4.3
Thermal conductivity (W/m.K)	~310
Specific Heat ($J.kg.K^{-1}$)	780
Volume resistivity (ohm.cm)	10^{10}
Dielectric Strength ($kV.mm^{-1}$)	>20
Dielectric constant	8.6
Loss tangent at 1 MHz	$5x10^{-4}$

2.1.2. Crystal structure of Aluminum Nitride

Aluminum nitride (AlN) is a hexagonal wurtzite 6H crystal structure **Figure 2.1**. and a covalently bonded material. Sintering additives and hot pressing are required to produce such dense and technical grade material. In the binary system AlN is the only stable compound. Al - N and exists in only one crystal structure (wurtzite, hexagonal). A wurtzite structure AB can be regarded as composed of two interpenetrating hexagonal close-packed lattices, one of atoms A, the other of atoms B [26,34–36]. AlN crystallizes at normal pressure in the wurtzite structure (I); space group $P6_3mc$ and the cell parameters are a=3.11 A^{o} and c= 4.98A°. At higher pressure, a transition to the rocksalt structure (II) was observed [36]. The rocksalt structure is a high-pressure phase at a transition pressure of 16–17 GPa according to X-ray data at 300 K at 22.9 GPa, metastable at ambient pressure. At a quasistatic high pressure loading it undergoes a first-order phase transition to the rocksalt structure [37].

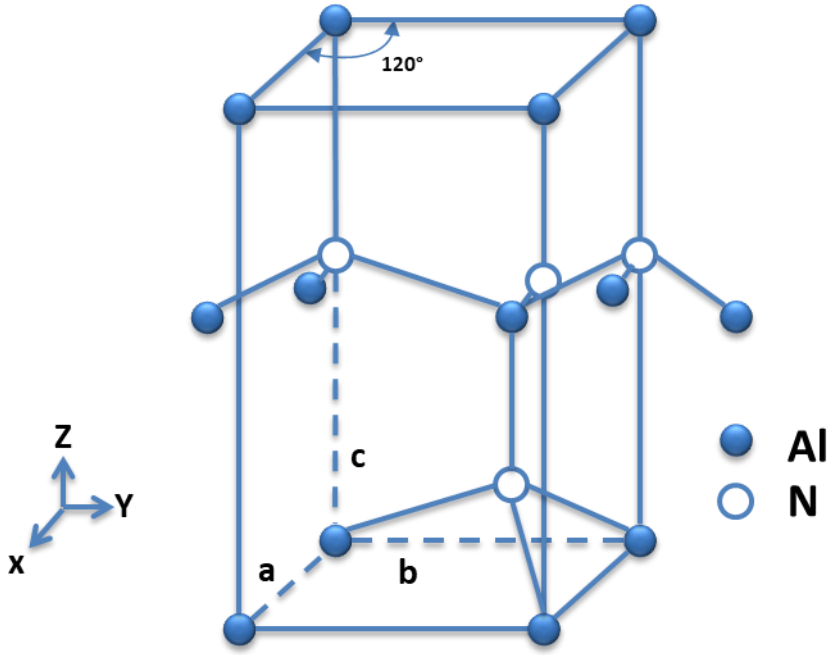

Figure 2.1. Crystal Structure of AlN.

2.1.3. Synthesis methods of AlN powder

There are mainly two methods of synthesizing applied commercially. These are:

(a) Direct nitridation of Aluminum powder and

(b) Carbothermal Nitridation of Al_2O_3

(a) Direct nitridation

A nitrogen atmosphere used in direct nitridation method at a high temperature of 800°C ~ 1200°C, where aluminum powder and aluminum nitride powder directly generate nitrogen compound.

$$Al + N_2 \rightarrow AlN \quad (1)$$

This method is modest and appropriate for mass production, and it has been used in industries. However, since the reaction is difficult to control, the aluminum nitride powder lumps is easily formed, thereby inhibiting the reaction, it is difficult to process the aluminum nitride powder of high purity [38]. The reaction is environmental friendly for no known harmful byproducts or greenhouse gases produced during the reaction. Advantage of direct nitridation is energy efficiency that the exothermic reaction generates ~328 kJ/(mol AlN) at 1,800 K. Aluminum melts at

933 K and the reaction with nitrogen begins at ~1,073 K, making it a self-sustaining process [39].

(b) Carbothermal nitridation

The carbothermal reduction reaction occurs at high temperature by reduction of metallic aluminum and nitrogen. Chemical equation for process is shown in eq.2.

$$Al_2O_3 + 3C + N_2 \rightarrow AlN + CO \quad (2)$$

Advantages of this method are fine granularity, wide material source, low cost and also suitable for mass production. The disadvantage is that long production cycle, low efficiency, low production out of the purity of the product, easy to form metal carbides [38].

2.1.4. Sintering of AlN

Sintering is the process where particle coalescence of a powdered aggregate by diffusion that is accomplished by firing at an elevated temperature [40].

2.1.4.1. Pressureless Sintering

Pressureless sintering is the sintering of a powder compact at high temperatures (~0.9 mp.) without any applied pressure. It avoids density variations and minimum anisotropy in the final component which occurs with hot pressing methods. Efficiency of pressureless sintering depends on the diffusivity of the atoms at high temperature.

Solid state sintering of non-oxide ceramics is difficult due to the covalent nature. A sintering additive is added which forms liquid phase at high temperature and helps sintering by particle rearrangement, solution re-precipitation and pore elimination steps. The process is called liquid phase sintering and is usually used in case of AlN. Sintering additives like Y_2O_3, CaO form Y-Al-O-N liquid phase at high temperature by reacting with Al_2O_3 present on the surface of AlN [37,41–44].

2.1.4.2. Hot Pressing

An externally applied pressure normally provides the major contribution to the driving force of sintering. The pressure is applied over a significant period of the heating process as in hot pressing and hot isostatic pressing. Surface curvature also

provides a contribution to the driving force, but for most practical situations it is normally much smaller than that provided by the external pressure [45]. Hot pressing technique involves the simultaneous use of external heat & uniaxial pressure to enhance the densification. In this technique powder is placed between a suitable die with a uniaxial pressure to form a compact. **Figure 2.2** is the schematic of hot pressing technique.

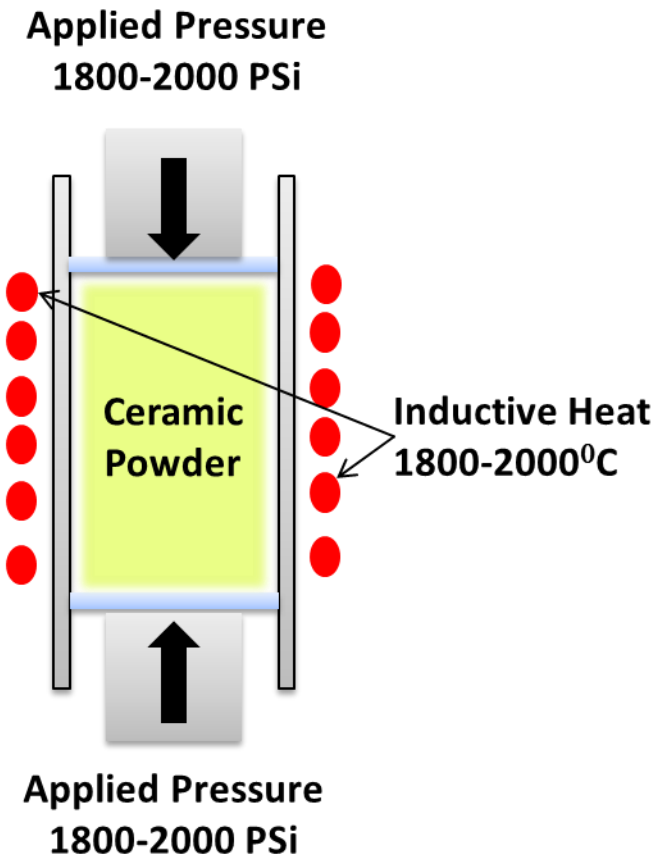

Figure 2.2. Hot pressing.

Hot pressing is generally used when the diffusion of atoms is very slow even at high temperature like those in covalent solids like nitrides, carbides and borides. Advantage of hot-pressing is the rapid densification leading to low grain growth and requirement of very little sintering additive.

2.2. Carbon Nano Tubes

Carbon Nanotube (CNT) is an allotrope of Carbon with a structure formed by graphene sheet rolled up in different directions. Carbon nanotubes are of different types according to their structure and chirality. It can be arm chair, zig zag or helical type structures **Figure 2.3.** CNTs have been the focus of frontier research. It has opened enormous areas of research which also include nanoscale reinforcements in composites to mend their mechanical, thermal and even electrical properties since their discovery [46,47].

CNTs are classified as single wall carbon nanotubes (SWCNT) and multiwall carbon nanotubes (MWCNT) depending on the number of concentric tubes in their structures. Multiwalled carbon nanotubes (MWNT) were the first to be discovered. These are close to hollow graphite fibers, except that these have a much higher degree of structural perfection. MWNTs are formed as concentric cylinders with a spacing between the layers close to that of the interlayer distance in graphite (0.34 nm). This interlayer spacing in MWNT is slightly larger than the single-crystal graphite value (0.335 nm) since in these tubes there is a strict geometrical constraint when forming the concentric seamless cylinders while maintaining the graphite spacing between them. The three-dimensional structural correlation that prevails in single crystal graphite (ABAB stacking) is lost in the nanotubes, and the layers are rotationally disordered with respect to each other. The second variety which is single-walled nanotube (SWNT) is close to an ideal fullerene fiber; in size they are close to fullerenes and have single-layer cylinders extending from end to end. SWNTs possess good uniformity in diameter (0.4-5 nm [25]). When produced in the vapor phase, the SWNT self-assemble into larger bundles (ropes) that consist of several tens of nanotubes. The tubes assemble into a one-dimensional triangular lattice structure with a lattice constant of 1.7 nm and tube-tube separation of 0.315 nm. This organization of nanotube units into a crystal structure was predicted earlier by theory. Both varieties of nanotubes can be considered as aggregates of nanotube units (cylinders). The aspect ratios of both MWNT and SWNT are high length is in several micrometres. MWNTs diameters typically range from 2 to 25 nm.

Properties of SWCNTs are superior to those of MWCNTs in many respects such as Young's Modulus, tensile strength, electrical and thermal conductivities [10–17]

Properties of SWCNTS could be modified by functionalization. Single walled carbon nanotubes (SWCNTs) offer exceptional transport properties in the 1-D nanostructure to the maximum extent among all the varieties of carbon nanotubes and possess high electrical conductivity (10^6 $S.m^{-1}$) [13] exceptionally high thermal conductivity (6.6 $kWm^{-1}K^{-1}$) [18], elastic moduli (1 TPa) [11] and tensile strength (22 GPa) [20]. Moreover, CNTs are resistant to plasmas [21]. SWCNTs can be metallic or semiconducting in nature depending on the chirality of their structures[19]. Separation of the tubes is needed in addition to purification since as-synthesized SWCNTs contain both metallic and semiconducting varieties [48]. Metallic SWCNTs possess quasi ballistic transport behaviour with excellent current carrying capacity and the current across different parts of the nanotube is uniform [23]. SWCNT achieved tremendous progress recently in nanodevices and nanocircuits showing remarkable logic and amplification functions. SWCNTs are also under intensive study as efficient storage devices, both for alkali ions for nanoscale power sources and for fuel cell applications [49].

2.2.1. Electronic structure of Carbon Nanotubes

Theoretical models were given by various researchers predicting rare electronic properties for this very novel class of materials after Iijima's detailed explanations [46]. CNTs were predicted to be either metallic or semiconducting according to the exact arrangement of their carbon atoms [50–54]. At that time, the impression of testing such predictions seemed unbelievable imaging these wires required the highest resolution transmission electron microscopes (TEMs). Historically, the first electrical measurements were performed on multi-walled nanotubes (MWNTs) [55], nanotubes composed of multiple concentric graphitic shells. However, the electrical characterization of nanotubes began in earnest in 1996, following the distribution of single-walled nanotubes (SWNTs) [13]. The simpler, single-walled morphology is more theoretically tractable, and electronic devices composed of SWNTs turn out to be sufficiently complicated without any additional shells of conducting carbon [56].

The electronic band structure of a nanotube can be defined by considering the bonding of the carbon atoms arranged in a hexagonal lattice. Carbon has four valence orbitals: 2s, $2p_x$, $2p_y$ and $2p_z$. Each carbon atom (Z = 6) is covalently bonded to three neighbor carbons via sp^2 molecular orbitals. The fourth valence electron, in the p_z orbital,

hybridizes with all the other p_z orbitals to form a delocalized π-band. As the unit cell of graphene has two carbon atoms an even number of electrons are contained in the basic nanotube structure, which consequently can be metallic/semiconducting [50–53]. explained using tight-binding electronic structure calculations with help of relationship between the coefficients (*n*1 and *n*2) of the translational vector $C_h = n_1a_1 + n_2a_2$, which connect two crystallographically equivalent sites, determines the conducting properties When $2n_1 + n_2$ is an integer multiple of three, the CNT exhibits metallic behavior while nonmetallic/semiconducting behavior, with conduction band gap (Eg), is obtained in all other cases. (This can also be stated as: mod($n_1 - n_2$, 3) = 0, 1, 2, where mod1 and mod2 SWNTs are semiconducting while mod0 SWNTs (*n*1 < *n*2) are metallic at room temperature, and exhibit a small chirality-dependent energy gap, corresponding to quasi-metallic conduction, at lower temperatures, the case *n*1 = *n*2 signifies armchair nanotubes that are truly metallic) [57]. If all values of the chiral vectors were equally probable, it would be expected that 1/3 of the total SWNTs would be metallic while the remaining 2/3 would be semiconducting, which is indeed what is found in synthesis [47].

2.2.2. Unique Properties of Carbon Nanotubes

CNTs are 1D nanostructure with dimensions of ~1 nm diameter (~10 atoms around the cylinder) [57]

Some important properties of carbon nanotubes are presented below in **Table 2.2.**

Table 2.2. Important properties of Carbon Nanotubes.

Property		**Value**
Average Diameter of SWNT's		0.4-5 nm [25]
C - C Tight Bonding Overlap Energy		~ 2.5 eV[58,59]
Young's Modulus (SWNT)		~ 1 TPa [60–64]
Young's Modulus (MWNT)		1.28 TPa [62]
Tensile Strength		~30 GPa[11]
Resistivity		10^{-4} Ω-cm[13]
Density:	(10, 10) Armchair	1.33 g/cm^3[60]
	(17, 0) Zigzag	1.34 g/cm^3[60]
	(12, 6) Chiral	1.40 g/cm^3[60]
Lattice Parameter:	(10, 10) Armchair	16.78 Å[60]
	(17, 0) Zigzag	16.52 Å[60]
	(12, 6) Chiral	16.52 Å[60]

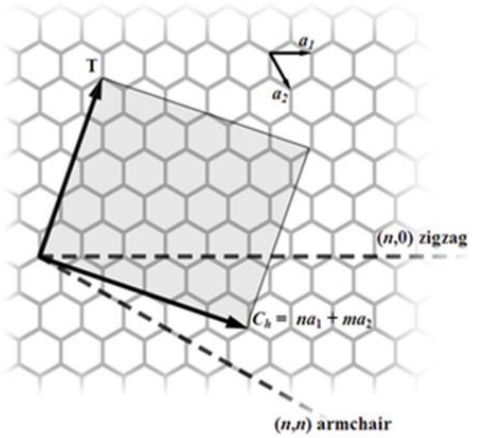

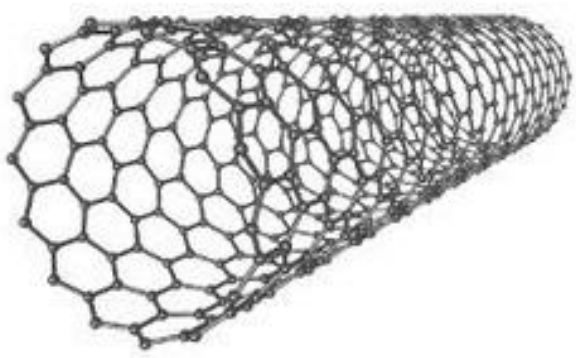

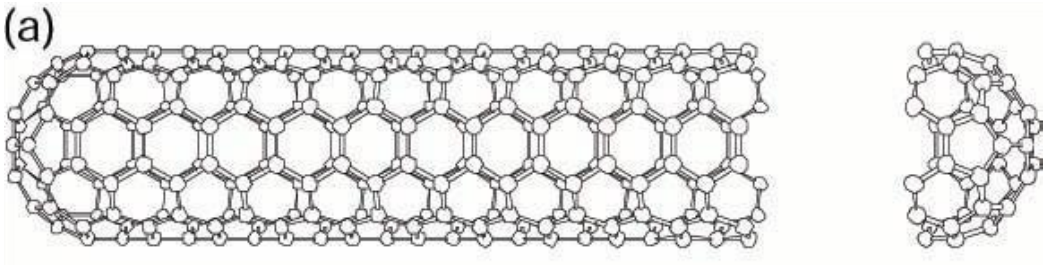

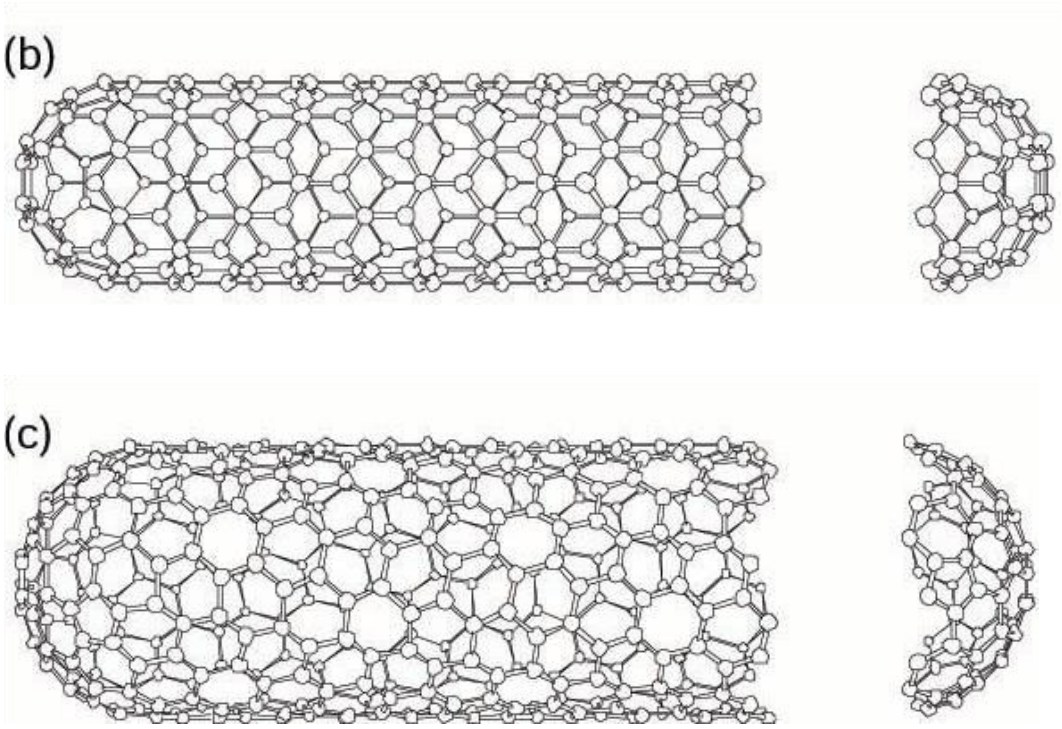

Figure 2.3. Graphene sheet rolled up to construct SWCNTs (a) armchair (b) zig zag (c) chiral [65].

2.2.3. Electronic properties of Carbon Nanotubes

In theory, metallic nanotubes can carry an electrical current density of 4×10^9 A/cm^2 which is more than 1,000 times greater than metals such as copper [66]. Due to their nanoscale dimensions, electron transport in carbon nanotubes takes place through 1D quantum effects and will only propagate along the length of the tube.

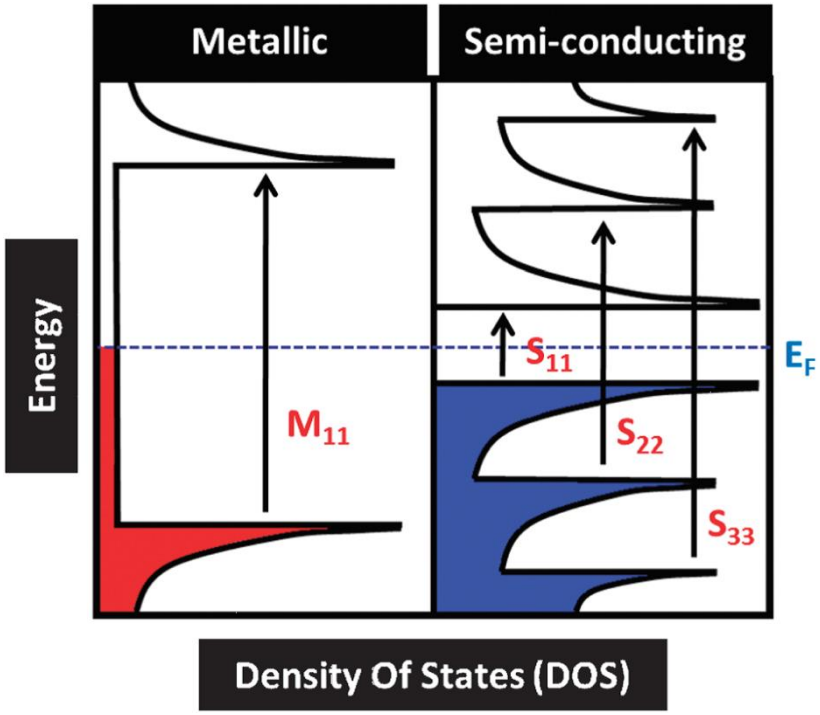

Figure 2.4. Schematic representation of van Hove singularities (vHS) and Fermi level positions (E_F) indicated by dashed blue line. Allowed electronic transitions between van Hove singularities are indicated by black lines. M_{11} and S_{11} denote lowest characteristic electron transition of the metallic and semiconducting SWCNTs respectively [14].

Density of States (DOS) of SWCNTs is defined by the van Hove Singularities (vHS) and schematically explained in **Figure 2.4** van Hove singularities are determined by the circumferential wave vector. A continuous DOS could be observed in armchair metallic SWCNTs which are very close to Fermi level. Very small band gap (50 meV) are observed in other metallic tubes which are usually neglected. In contrast, semiconducting SWCNTs have very high band gap (500meV). Position of the Fermi level varies with the doping and diameter [14].

Individual metallic SWCNTs conduct ballistic transport and act as molecular quantum wires [67–69]. Metallic SWCNT bundles show an initial decrease and then flattening of conductivity values with temperature increase. Low temperature region shows the predominance of tunneling mechanism while high temperature region the tunneling is mostly influenced by the thermally activated behavior [67]. Semiconducting nanotube bundles showed thermally assisted tunneling all through the temperature range and therefore, a Schottky barrier induced transport was concluded [67]. It had also been observed that SWCNT mats containing several individual CNTs having both metallic

and semiconducting tubes behave differently than the individual basic units and a mixed metallic/non-metallic model had been proposed which could explain the temperature of the dc- electrical conductivities of the tube involving a defect scattering during the transport [67]. The conductivity characteristics differ with the thickness of the mat and changes from semiconducting to metallic as the thickness increases and the hopping mechanism is involved at the junction of metallic and semiconducting tubes [67]. The peak is near room temperature when the scattering process dominates with further increase of temperature.

Metallic SWCNTs have high dielectric constant (ε>3000) while semiconducting tubes have lower value (<10) [14]. Larger the diameter the dielectric constant becomes greater. Polarizability of metallic tube is much greater than that of semiconducting tubes due to the presence of more mobile charge carriers [70].

2.2.4. Thermal Properties of CNTs

All nanotubes are expected to be very good thermal conductors along the axis, while less conducting along the cross section of the tube. Balandin(2011) has presented a thorough review on the thermal properties of CNTs [70]. High thermal conductivity is due to the presence of maximum conjugation of electronic orbitals (sp^2) in the structure enabling the transmission of thermal energy by phonons very fast [70]. It had been predicted theoretically that the thermal conductivity of SWCNTs is 6600 $W/m^{-1}K^{-1}$ [18] while that of MWCNT is 3000 $W/m^{-1}K^{-1}$ at room temperature which are very high in comparison to that of Copper, a metal well-established for its high thermal conductivity (385 $W/m^{-1}K^{-1}$) [71,72]. Lower conduction in MWCNT is due to the increased interaction of phonons with electrons in the multiple layers [70].

Temperature dependence of thermal conductivity of SWCNT is very interesting and complex to understand. Many studies could be noticed to understand the phonon conduction behavior in SWCNTs [73–75]. Thermal conductivity of SWCNT(metallic) increases ballistically with the least scattering of phonons at low temperatures below 300K. Only scattering that takes place is on the surface of the tubes [73]. More phonon modes contribute towards further increase of temperature and the conductivity increases with specific heat unless a peak in thermal conductivity is attained when the optical phonons and the scattering become active [73]. High

temperature data for thermal conductivity of the CNTs, at least upto 1000K is essential for the application of ceramic nanocomposite systems but rarely available [73–75]. Thermal conductivity of SWCNT (metallic 10,10) had been calculated by the simulation of thermal transport with Molecular Dynamics (MD) upto 400K [76]. Subsequent scaling to higher temperature and tube length showed that the peak temperature shifts higher with the decrease of length of the tube [76]. Shorter tube length does not allow for sufficient phonon-phonon collision and needs longer amplitude phonons for the scattering to occur at higher temperature, thus, making the level off at higher temperature. As the tube length increases chances of phonon-phonon collision increases and further scattering by the larger amplitude phonons at higher temperature and attaining the maximum at lower temperature. Overall ballistic transport and consequently the thermal conductivity is higher in the longer tube [76]. However, Thermal conductivities of CNT mats/networks have poor thermal conductivity value, almost a decade less than the single individual tubes even though it is higher than most of the polycrystalline ceramics measured [73].

This is one of the reasons why researchers are interested to incorporate CNTs in materials to increase the thermal conductivities. Thermal conductivity of CNT decreases with the diameter of the tube [77]. However, the mechanism of phonon conduction in composites is very complex and will be discussed later in chapter 7 section 7.2

Carbon nanotubes can be stable upto 2800^{o}C in vacuum and about 750^{o}C in air [78].

Thermoelectric effect (Seebeck Coefficient) is related very much to the roll up direction of the graphene sheet to form SWCNT structure. The low temperature Seebeck coefficient (α_i) could be expressed as,

$$\alpha_i(E_f) = -\frac{\pi}{3}\frac{\kappa_B}{e}\kappa_B T\left[\frac{\partial \ln[N(E)]}{\partial E}\right]E = Ef \qquad (3)$$

Where, 'κ_B'is Boltzman constant, 'e' is the elementary charge, 'N(E)' is density of states and 'Ef' is the Fermi energy.

Thermopowers in the range of 11 to 160μV.K^{-1} had been observed in SWCNTs [70]. Metallic tubes have low thermopower explained by the constant density of states between widely spaced occupied and unoccupied vHS. Experimental value in the

range of 10-20 $\mu V.K^{-1}$ have been obtained [79]. On the other hand, semi conducting tubes show much higher thermopowers (80-160 $\mu V.K^{-1}$) [79]. Thermopower of SWCNTs depends on the resistances offered by intertube junctions. Random network of SWCNT mats offer more number of tube junctions and increases the thermopower than that of the individual tubes [79].

2.3. Ceramic-CNT nanocomposite

Nanocomposites are multiphase solid material in which one of the components is in nano dimension (1-100 nm). Nanocomposite materials received a lot of attention in recent years by scientists and engineers. By using building block nanomaterials it is possible to design and create new materials with exceptional and tunable properties. These advance nanocomposites can achieve interesting functional properties for high end applications. The multifunctional behavior of such material unravels often new phenomena which is different than the individual components. For example, porous ceramic- CNT composites not only show negative permittivity and permeability but also Fano type resonance at high frequency which were absent in the individual components. Following sections will provide an up-to-date status of researches on the properties of ceramic nanocomposites containing CNT.

2.4. Mechanical Properties of Ceramic-CNT nanocomposite

The unique mechanical properties of Carbon nanotubes discussed in **Table 2.2** have been exploited by earlier researchers to enhance the mechanical properties like strength and fracture toughness (K_{IC}) of brittle ceramics. Positive effect of CNT reinforcement could be clearly visible on the strength and toughness increase of glass-ceramic-CNT composite where the microstructural features like grain interfaces were absent [80]. **Table 2.3** provides brief results of earlier studies on mechanical properties of different ceramic nanocomposites.

Table 2.3. Literature review on mechanical properties of ceramic CNT composite

Sr. No.	Matrix	CNT Content	Processing Route	Method	Hardness (GPa)	K_{IC} ($MPa \cdot m^{1/2}$)	Toughness Mechanism	Ref. (Year)
1	SiO_2	MWNT 6 wt%	Sol-gel method	Vickers indentation	3.432	-	Pull-out, Crack Bridging	[81] (2001)
2	SiC	MWCNT 1-5 vol. %	Sol-gel method	Vickers indentation	30.6	5.4	Pull-out, Crack Bridging	[82] (2007)
3	SiC	7vol%	Spark Plasma Sintering	Vickers Indentation	10 to 18.3	3.3	Crack deflection	[83] (2017)
4	SiC	CNT 10 vol%	Spark Plasma Sintering	Vickers indentation	-	4.4	Pull out, bridging	[84] (2018)
5	SiC	7 vol.% CNT	Spark Plasma Sintering	Vickers indentation	18.3 ± 0.8	3.2	Crack deflection	[83] (2017)
6	Al_2O_3-5SiC	1-2 vol % CNTs	Spark Plasma Sintering	Vickers indentation	19.77-19.11	3.89-4.2	Crack deflection, Crack bridging	[85] (2016)
7	Al_2O_3	SWCNT 10 vol.%	Powder processing	Vickers indentation	15.78	9.7	Crack bridging, CNT pull-out, Crack deflection and residual stress	[86] (2007)
8	Al_2O_3	SWCNT 1 vol %	Spark Plasma Sintering	Vickers indentation	-	4.2	Interfacial debonding/decohesion, crack deflection and interlocking of grains	[87] (2018)
9	Al_2O_3	CNT (1–3 wt%)	Spark Plasma Sintering	Micro-indentation test	-	6.4	CNT yarning, pull out	[88] (2018)
10	Al_2O_3	0.1 wt% MWCNT	Spark Plasma Sintering	Vickers indentation	19.0±1.54	1.5	Crack bridging, Pull out	[89] (2016)
11	Al_2O_3	0.1 wt% SWCNT	Spark Plasma Sintering	Vickers indentation	18.0±2.19	2.0	Crack bridging, Pull out	[89] (2016)
12	Al_2O_3	CNT 2 wt.%	Spark Plasma Sintering	SENB	19.1±1.6 (VH)	3.9	Crack-bridging, Pull out	[90] (2013)
13	Al_2O_3	CNT 3.1 wt.%	Spark Plasma Sintering	Vickers indentation	13.8 ± 1.5	-	Crack-bridging, Pull out	[90] (2013)
14	Al_2O_3	5.7 vol% SWCNT	Spark plasma sintering	Vickers indentation	20.0	7.9	Crack deflection	[91] (2003)
15	Al_2O_3	5 vol% CNT	Pressureless sintering	Vickers indentation	12.6	3.6	crack deflection and crack bridging	[92] (2010)

16	Al_2O_3	7.39 wt.% CNT	Spark plasma sintering	Vickers indentation	9.98	4.7	CNTs pull-out	[93] (2009)
17	TiC-3.5 wt% WC	2 wt% CNT	Spark Plasma Sintering	Vickers indentation	33.5 ± 4.5	7.8	CNT bridging, crack bifurcation and CNT pull out	[94] (2017)
18	3YTZP-SWCNT	2.5 to 10vol% CNT	Spark Plasma Sintering	Vickers indentation	13 to 9.2	6.1 to 5	Crack bridging, deflection and uncoiling of CNT	[95] (2014)
19	3YTZP	1 vol % SWCNT	Spark Plasma Sintering	Vickers indentation	9.6 ± 0.9	-	-	[96] (2016)
20	3YTZP	MWCNTs (4 wt%)	Spark Plasma Sintering	Vickers indentation	11.39±0.42	-	CNT pull-out and Crack deflection	[97] (2015)
21	3YTZP	MWCNTs (6 wt%)	Spark Plasma Sintering	Vickers indentation	11.06±0.49	-	CNT pull-out and Crack deflection	[97] (2015)
22	ZrB_2-20 vol% SiC	15 vol% MWCNT	Spark Plasma Sintering	SENB	15.5±0.7 (VH)	6.9	Crack deflection, pull-out	[98] (2015)
23	Si_3N_4	CNT 1 wt.%	Hot Pressing	Vickers indentation	~15.5	~6.25	Crack deflection, pull-out	[99] (2018)
24	Si_3N_4	5.3 vol% MWCNT	Spark plasma sintering	Vickers indentation	12.6	4.2	-	[100] (2009)
25	Si_3N_4	CNT 5 wt.%	Hot Pressing	Vickers indentation	~13.25	~5.75	Crack deflection, pull-out	[99] (2018)
26	WC	1.0 wt% CNT	Spark plasma sintering	Vickers indentation	22.25±0.53	8.92	Crack Bridging, pull-out, and crack deflection	[101] (2018)
27	Si_2BC_3N	1-3 vol% MWCNT	Spark plasma sintering	SENB	~5.25 ~3.5 (VH)	5.54-4.31	Crack bridging, pull-out, crack deflection	[102] (2018)
28	TiB_2–20 vol % SiC	15 vol% CNT	Spark plasma sintering	SENB	-	10.4	Crack deflection, crack bridging, CNTs debonding and pull-out.	[103] (2017)
29	Alumino Borosilicate Glass Ceramics	5 to 15wt% CNT	Hot Press	SEVNB	10.4 to 7.2	1.6 to 1.25	Crack Bridging	[80] (2010)
30	3YSZ	0.5 to 5wt% CNT	Spark plasma sintering	Vickers Indentation and SEVNB	12 to 12.75	5.5 to 11 6 to 8	Crack Bridging Uncoiling of CNT	[104] (2011)

It could be observed from **Table 2.3** that the toughening mechanism in ceramic nanocomposites consists of several mechanisms.

1. Crack bridging by nanotube bundles
2. Crack deflection at grain boundaries
3. Pull out of CNTs
4. Residual stress toughening
5. Uncoiling and stretching of CNTs

A fracture toughness, as high as 9.7MPam$^{1/2}$, was first reported by Zhan et al. 2003 [105] in Al_2O_3 –SWCNT composite which is almost 3 times that of the corresponding Al_2O_3 matrix. Load transfer in an entangled network of nanotubes surrounding the Al_2O_3 grains and crack deflection are the main mechanism of toughening proposed by them. Strategy of their achievement was to use starting Al_2O_3 particles whose average size was in nanometer range (primary particle size 40nm and 30nm for α- and γ-varieties) and purified SWCNT with maximum dispersion. Early researches on the development of ceramic-CNT nanocomposite also indicated increase in fracture toughness of the composites [106–108]. Most of the works were carried out with Al_2O_3, CaO or Y_2O_3 stabilized ZrO_2, SiC and Si_3N_4 ceramics. A 33% increase in K_{IC} value have been observed when CNTs (7vol%) were incorporated in nano SiC matrix [83]. Strong interfaces between nanotubes and matrix interfaces have been believed to be the reason behind the toughness increase in in-situ composite compared to ex-situ Si_3N_4-CNT (12vol%) composite [109]. However, both the fracture toughness and hardness is lower than that of matrix (Si_3N_4) [109] It has also been observed that Si_3N_4-SWCNT composite exhibit lower toughness values than the monolithic Si_3N_4. Thus, the toughening effect of CNTs depends on the toughening mechanism of the ceramic matrix. Si_3N_4 is known for in-situ toughening created by a non-equiaxed microstructure through the presence of elongated β- Si_3N_4 spikes. Presence of CNTs hinders the α to β conversion and reduces the growth of β- Si_3N_4 grains which, reduces the toughness of the composite. Crack deflection was first observed in the earliest work [106] and believed to be the toughening mechanism in SiC matrix. Cho et al. [110] have shown that K_{IC} increases with the SWCNT content in glass ceramics system and measurement by indentation fracture method produced almost the same trend with the CNT content as those measured by Chevron notch method. However, the values obtained by indentation fracture method are overestimated by a factor of

two and hence absolute value could not be produced by the indentation fracture method. A residual stress toughening arising out of the difference in thermal expansion co-efficients between Al_2O_3 and CNTs has been assigned for the increase in fracture toughness with the addition of CNTs [86] although its contribution seems to be less when the difference in CTE between matrix and CNT is less like that of ABS glass ceramics- CNT nanocomposite [80]. High fracture toughness has been observed with ZrO_2 sample [111]. A crack bridging model had been proposed by Mukhopadhyay et al. (2010) [80] from the SEM examination of an advancing crack. Although frictional pull-out of CNTs during the fracture of the composite had been proposed by several authors [86,111] but it had been questioned by several others [80,104,112,113] on the ground of small dimension and flexibility of the tubes principally existing along the grain boundaries where the friction is less for the pull-out to take place. Unfurling/uncoiling of the nanotube ropes and subsequent stretching of them perpendicular to crack surface had been observed from in-situ observation from SEM and proposed to be the main toughening mechanism in Al_2O_3 – SWCNT and Al_2O_3-MWCNT composites [112,113]. These stretched bridges finally fail with further loading by non-frictional pull-out.

Hardness values of ceramic-CNT composites obtained by earlier results are also presented in **Table 2.3**. It could be observed that hardness decreases from the value of the monolithic matrix ceramics on addition of CNTs in most of the cases. Nevertheless, baseline hardness of the matrix is the controlling value of the hardness of the composites but not always governed by the rule of mixture (ROM) applied by taking into account of those of the individual components. Another important factor to be noticed, in this context, that the grain sizes decrease on addition of CNTs in the matrix and accordingly hardness should have been increased in accordance with the Hall-Petch relation, which does not follow in the case of ceramic-CNT composite. A clear theoretical understanding in this context is not available in literature.

2.5. Electrical properties of Ceramic Nanocomposite

2.5.1. Electrical Conductivity (dc)

Ceramic-CNT composites are gaining importance over the last two decades due to improved electrical properties over their monolithic matrix for multifunctional

applications like smart structures, heaters, electromagnetic shields and supercapacitors and ease of machining by electrodischarge machining (EDM) [16,109,110,112,114,115]. EDM machining of any material demands the conductivity to be at least in the semiconducting region [116]. Percolation of electrical conductivity takes place at a very low concentration of CNT in the matrix since there is huge difference in electrical conductivity between the matrix and the tubes. Percolation is the sudden change in bulk properties of materials when a network of the dispersoids form in the matrix at a critical concentration of the diespersoids called "Percoation Threshold" [116]. The first study on percolation threshold (0.64%) was reported by Rul et al [117] in SWCNT-$MgAl_2O_4$ composite. CNTs conduct electricity along their length with tiny resistance and a SWCNT rope has a longitudinal conductivity of 10^6 S/m at 300 K [13] as discussed in section 2.2.2. It has also been discussed earlier in section 2.2.1. that SWCNT may be either metallic or semiconducting depending on the chirality within the structure [19]. Properties of ceramic-CNT composites could be tailored by choosing the types of SWCNT (metallic or semiconducting) [19]. No report could yet be noticed highlighting the development and properties of the ceramic nanocomposites containing a particular electrical variety of the SWCNT. Understanding the functional properties of these composites is, therefore, very important and very little work could be observed in the literature [109,117–120]. Earlier results on the studies of electrical properties of the ceramic-CNT composites are presented in **Table 2.4.**

Zhan et al. reported the highest electrical conductivity of Al_2O_3- SWCNT and 3Y-TZP/CNT/Al_2O_3 bulk composites prepared through spark plasma sintering (SPS) [91,121].

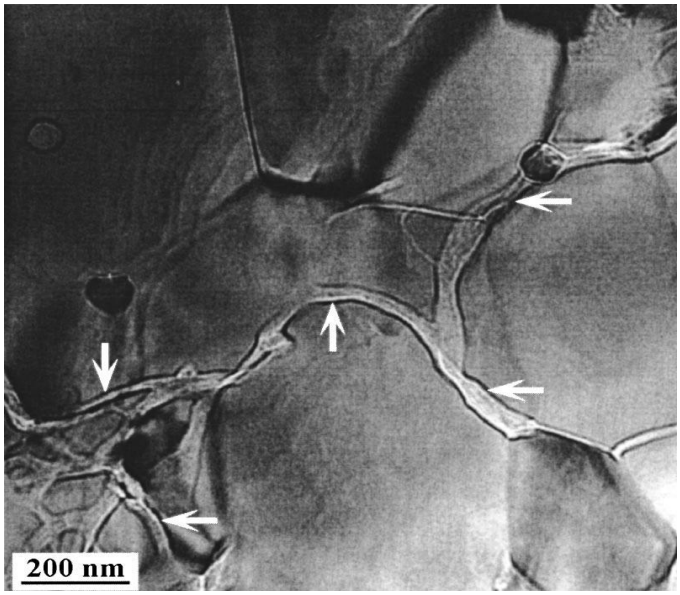

Figure 2.5. TEM image of the 5.7-vol % SWCNT/Al_2O_3 nanocomposites showing intertwining network structure of carbon nanotubes in the matrix. SWCNT ropes are indicated by white arrows [118].

Figure 2.5 shows the interconnecting structure of carbon nanotubes in the Al_2O_3 matrix. Alumina is an insulator material with extremely low electrical conductivity (~10^{-12} S/m). It is interesting to note that the SWCNT/Al_2O_3 composites become much more electrically conductive(3345 S/m) when 5.7 vol% amounts of SWCNTs were incorporated into alumina [118].

Conductivity measurements were made by using a four- probe method at four temperatures -196, -61, 25, and 77 °C. It was found that the electrical conductivity rises with temperature exhibiting semiconducting behavior of the material [84]. The three compositions of their study reported an increase of conductivity with increasing temperature on an average. It could be observed from the microstructure of these composites is that the grain size of the sintered product is very small and, therefore, helps the CNT mat to form network all around the grains and increase the electrical conductivity. Different property windows were gradually opened and detail studies were followed by later studies on multifunctional properties of the composites. For example, K. Ahmad et al [119] prepared Al_2O_3/MWNT composites with different MWNT contents varying from 0.5 to 10 vol % by spark plasma sintering (SPS) technique. The dc electrical conductivity and dielectric properties of the composites were investigated and the percolation theory was applied to demonstrate the electrical property transition from insulator to conductor. A significant increase of DC electrical

conductivity of around eight orders of magnitude from 5.15 $X10^{-12}$ to 8.93 $X10^{-4}$ S/m had been found between 0.7 and 0.87 vol % of MWNTs. They had also shown that dielectric constant increased at low frequency in percolation threshold regime and reached around 5000 in the volume fraction of 1.7% [119]. It was for the high aspect ratio of CNT the percolation threshold is low and the electrical conductivity increased to a great extent when compared to sperical carbon black particles [118,122]. It was also shown that the conductivity increased with the grain size for a constant concentration of CNT [122]. Most of the studies made earlier was on oxide ceramics-CNT composites and especially on Al_2O_3 – CNT composites. Si_3N_4 and SiC are the matrix material mostly studied among non-oxide ceramics. High thermal conductivity (16.72 W/m-K) had been achieved in bulk 3D MWCNT material bonded with SiC [120]. The composite exhibited semiconducting behavior, which is explained with 3D variable range hopping mechanism [120]. Similar charge transport and hopping mechanism in Si_3N_4-CNT composite material [109]. Most of the works on CNT composites was based on MWCNT. Very few studies could be traced on non-oxide-SWCNTcomposites. The reason may be due to high cost of SWCNTs and difficulty in dispersions.

Table 2.4. Literature review on Electrical properties of Ceramic CNT composites

Sr. No.	Method of Preparation	Composite	CNT Vol%	Electrical Conductivity	RD (%TD)	References (Year)
1	Spark plasma sintering	Al_2O_3 -SWCNT	5.7- 15vol %	1050-3345 S/m	100	[118] (2003)
2	Spark plasma sintering	Al_2O_3-MWCNT	0.7-vol%	$5.15*10^{-12}$ S/m	-	[119] (2006)
3	Spark plasma sintering	Al_2O_3-MWCNT	0.87-vol%	$8.93*10^{-4}$ S/m	-	[119] (2006)
4	Spark plasma sintering	Al_2O_3-MWCNT	10 wt %	140 S/m	-	[123] (2012)
5	Spark plasma sintering	Al_2O_3-5SiC-CNT	1-2 wt%	4.28-8.85 S/m	97.7%	[124] (2017)
6	HP	$MgAl_2O_4$-MWCNT	1.16 vol%	0.4 s/m	-	[117] (2004)
7	HP	Borosilicate glass-MWCNT	10 wt%	0.076 S/cm	91 ± 2 87 ± 2	[125] (2007)
8	Spark plasma	SiC-MWCNT	2.1 vol%	1538 S/m	-	[126]

	sintering					(2005)
9	Spark plasma sintering	SiC-MWCNT	-	21.18 S/m	-	[120] (2015)
10	Pressureless sintering	3Y-TZP/MWCNTs(3 mol% Y_2O_3 stabilized ZrO_2)	1 wt% MWCNT	132 ± 4.12 S/m		[127] (2006)
11	Spark plasma sintering	3YTZP-SWCNT	1.5 vol%	$6*10^{-6}$ S/cm	-	[122] (2015)
12	HP	ZrO_2–CNT	1.07 wt.%	9.524±0.05 S/cm		[128] (2008)
13	Spark plasma sintering	SiO_2- MWNT	10 vol.%	65 S/m		[129] (2007)
14	Spark plasma sintering	Si_3N_4- SWCNT	1 vol%	$4.7*10^{-5}$ S/m	95.4	[114] (2011)
15	Spark plasma sintering	Si_3N_4-SWCNT	2 vol%	$4.7*10^{-5}$ S/m	91.0	[114] (2011)
16	Spark plasma sintering	Si_3N_4-SWCNT	6 vol%	92 S/m	91	[114] (2011)
17	Hot pressing	Si_3N_4 -MWNT	5% wt%	130 S/m	-	[130] (2006)
18	GPS followed by HIP	Si_3N_4- CNT	1.8 wt %	30 S/m	-	[131] (2005)
19	HIP	Si_3N_4-CNTFs	1.8 wt %	79 S/m		[131] (2005)
20	Sintering	Si_3N_4- CNTFs	7 wt %	1.03×10^2 S/m		[132] (2018)
21	Pyrolysis	Polysilazane (Ceraset)- SWNTs	1 wt%	0.06 S/cm		[133] (2017)
22	Sintering	Bismuth telluride - CNT	0.15 wt%	670 S/cm	0.81	[134] (2018)
23	Sol Gel+HP	Aluminoborosilicate glass/MWCNT	15 wt%	200 S/m		[135] (2015)

Main challenges observed by earlier researchers is the homogenization of SWCNT in ceramic matrices [110,122]. Many attempts had been made for the maximum dispersion of SWCNTs in ceramic matrices. Mukhopadhyay et al. [135] started with ceramic precursor and steam purified MWCNTs for the maximum dispersion of CNTs in Aluminoborosilicate Glass Ceramics prepared by sol-gel process and

subsequent hot pressing. They obtained high electrical conductivity (200 S/m) with 15 vol% CNT addition. Poyato et al. had pointed out that percolation threshold becomes higher when agglomeration and interconnectivity of the agglomerates show higher values of conductivity at a higher CNT concentrations [122] A colloidal technique and ultrasonic agitation had been used to prepare the pre-sintering powders of 3YTZP –SWCNT composites [136]. A colloidal aqueous processing technique with zeta potential monitoring had been successfully accomplished with subsequent SPS to prepare dense SiC-MWCNT composite ceramics [90].

2.5.2. Dielectric properties (Impedance, Reactance Permittivity)

Complex impedance analysis of polycrystalline ceramics provides the information on the electrical conduction and subsequent loss in grains and grain boundaries by using the model of equivalent circuits. The present review will be restricted to the earlier studies on dielectric characterization of ceramic – CNT composites. Different types of polarizations becomes active with the change of frequencies and could be realized from the impedance spectroscopy. Cole-Cole plot involving complex impedance planes Z″ vs. Z′ presents the details electrical conduction characteristics. Semicircles in these plots indicate the grain and grain boundary contributions on the total conductivity. It had been concluded from the relaxation frequencies calculated from the semicircles obtained in the impedance spectra that the relaxations are primarily controlled by the nanotube bundles present in the grain boundaries [109].

Importance of Impedance Spectroscopy increased recently with the recognition of metacomposite characteristics in Carbon containing ceramic composites [137]. Two types of negative permittivity behaviours have been observed in Al_2O_3 – MWCNT composites [137]. Negative permittivity due to Lorenz type resonance below the percolation level and plasma like negative permittivity behavior above the percolation level have been observed in these composites [137]. Negative permittivity has been observed in AlN composites with high loading of graphene platelet (19.5wt%) [138].

The present thesis reports the analysis of electrical properties in AlN -SWCNT, a new nanocomposite which has been prepared by conventional hot pressing from commercial AlN powder and SWCNTs enriched with metallic variety tubes. The combination of AlN and SWCNT is chosen since both of these materials have high thermal conductivity and improvement in electrical conductivity could lead to several

applications where heat dissipation is a great concern. Analyses of the temperature dependences of the dc-electrical conductivities and the microstructure of the composites are presented to explore the mechanism of transport in the composite. The SWCNT addition in AlN ceramics promises not only an increase in the electrical conductivity of the material but a plasma like negative permittivity as observed from the impedance spectroscopy.

2.6. Thermal properties of ceramic nanocomposite

The Fourier's law of heat flow under non-uniform temperature defines the macroscopic thermal conductivity and the steady state heat flow $\overrightarrow{J_q}$ is attained by keeping the system and reservoirs in contact,

$$\overrightarrow{J_q} = -\Lambda \nabla T, \tag{4}$$

Where, Λ = thermal conductivity tensor, and $\overrightarrow{J_q}$ = heat current produced by the temperature gradient ∇T.

Fourier's law of heat flow can be derived from linear response theory [139]. For isotropic systems, the conventional thermal conductivity λ is given by,

$$\lambda = \frac{1}{3} \mathrm{Tr} \Lambda \tag{5}$$

Ceramics, in general, are bad conductors of heat. Some ceramics like AlN (hexagonal) and SiC(hexagonal) have high thermal conductivity because of their adiamantine crystal structures.

High thermal conductivity of AlN(310 W/m-K) is the principle attribute which makes the material highly demanding for thermal packaging purposes. A high thermal conductive substrate obviates the necessity of external cooling and facilitates packages development with high chip density as mentioned earlier [44].

Similarly, an unusually high thermal conductivity(~6600 W/m-K) of Carbon Nanotubes [18] gives the promise of preparing a composite material having both highly thermal and electrical conducting. Carbon nanotubes are also capable of being used as thermoelectric generators as mentioned earlier section 2.2.4. CNT- composites should provide additional opportunities to engineer critical interfaces toward even higher performance [140]. The high thermal conductivity of carbon nanotube depends

very much on the size, structure and defects which interact with the conduction of phonons [141]. Ceramic nanocomposites containing CNTs show higher electrical conductivities and lower thermal conductivities and should be promising for increasing thermopower of the material. A brief review of the results obtained by earlier researches on thermal properties of ceramic-CNT nanocomposites is presented in **Table 2.5.**

Table 2.5. Literature review on Thermal properties of ceramic composite.

Sr. No.	Matrix	CNT vol/wt%	RD	Method of preparation	Seebeck coefficient	Thermal conductivity W/mK	Figure of merit (ZT)	Ref. (year)
1	SiC	8 vol % CNT	0.93	SPS	-	14.9	-	[142] (2018)
2	SiC	CNT	-	SPS	-	16.72	-	[120] (2015)
3	SiC	CNT	-	pyrolysis	-	6.59	-	[143] (2013)
4	SiC	CNTs 0.05 wt%	-	electrophoretic deposition	-	14.3	-	[144] (2017)
5	Bismuth telluride	0.15-0.30 CNT wt%	0.81 0.86	Sintering	−115 µV/K −163 µV/K	1.1 1.2	0.25 0.23	[134] (2018)
6	Bi_2Te_3	1 wt % MWCNT		Hydrothermal technique	−121 µV/K	~1.3	-	[145] (2017)
7	Bi_2Te_3	3 vol.% MWCNT	96 ± 1.0	SPS	−113 µV/K	1.0	0.28	[146] (2013)
8	Al_2O_3	8 vol % MWNT	0.79	Hot pressing	-	7.8	-	[147] (2015)
9	Al_2O_3	10.4 vol % MWCNT	-	SPS	-	~12.5	-	[148] (2014)
10	Al_2O_3	8 wt % MWNT	-	DC arc plasma spraying	-	6.1	-	[149] (2005)
11	Al_2O_3-10SiC	2 vol % CNT	95.40	SPS	-	17.81		[124] (2017)
12	Al_2O_3	10 vol.% SWNT	>98%TD	SPS	27 µV/K	0.2	0.018	[121] (2006)
13	$BaTiO_3$	2.45 vol % MWNTs	0.99	SPS	-	2.98	-	[150] (2005)
14	SiO_2	10 vol.% MWCNT	0.1	SPS	-	4.08 ± 0.01	-	[151] (2007)
15	TiN	5 wt% MWNTs	0.98	SPS	-	~33.096	-	[152] (2008)
16	B_4C	10 vol % CNT	-	Hot pressing	-	30.6	-	[153] (2013)
17	Si_3N_4(β-44 to 38 vol%)	1.8, 5.3,8.9	-	SPS	-	9 -13	-	[154] (2012)
18	Si_3N_4	CNT 22.9 wt%	-	reaction-bonded	-	2.8	-	[155] (2019)

				sintering process				
19	ZnO	MWCNT	-	flame transport approach	-	0.46 ± 0.04	-	[156] (2019)
20	Zn0.98Al0.02O	0.1 wt.% MWCNT	94 ± 2%.	SPS	-40 lV/K	26	0.08	[157] (2016)
21	$Bi_2Ba_2Co_2O_y$	1.0wt% CNT		Solid-state reaction method	-	0.39	-	[158] (2017)

It could be observed from **Table 2.5** that the thermal composite becomes lower when CNTs are incorporated into the matrix whose thermal conductivities are high although CNTs have very high thermal conductivity as mentioned in Section 2.2.4. Thermal conductivity increases in very low thermal conductivity glass-ceramics and SiO_2 materials on addition of CNTs. Principal reason for the decrease in conductivity is the increase in thermal resistances by grain CNT interface alongwith the intertube resistances. Zhan et al [17] have observed decrease of thermal diffusivities in dense Al_2O_3-SWCNT composites along transvers direction (parallel to pressing direction) with the increase in content of SWCNTs (10 and 15 vol%) and temperature. The decrease of thermal conductivity with the SWCNT contents were attributed to the lower thermal conductivity of the bundles containing bends and twists of the tubes than the basic elements, tub-tube thermal junctions causing scattering of phonons [18] and thermal resistance due to ceramic grain and bundle interfaces (Kapitza effect). Phase assemblage of ceramics after high temperature processing contributes in a complex way to the thermal conductivity of the composite. For example, Si_3N_4 usually is available as feedstock in α-phase and undergoes transformation to β-phase during high temperature processing [159,160]. β- content in the material increases thermal conductivity as observed by Miranzo et al (2007) [154] Rapid heating processes like hot pressing and SPS reduces the transformation and consequently the thermal conductivity of the base matrix. Additionally the incorporation of MWCNT reduces the thermal conductivity [154].

One of the hurdles in calculating the thermal conductivities of the composites from the Eqn.35 is the estimation of the specific heat values of the tubes and mats. There is very little information available on the heat capacity and thermal diffusivity of CNT at high temperature as informed in earlier Section 2.2.4. Many estimations have, therefore, been made earlier by using the value of graphite, a structurally similar material [148,154].

Chapter 3

Materials and Methods

This chapter describes the materials and methods implemented for the present study on the development and characterization of AlN-SWCNT nanocomposite.

3.1. SWCNT purification and enrichment with metallic tubes

Development of an efficient process for chemical treatments that can control the quality of the CNT samples and induce both their dispersion and partial or complete unbundling remains highly challenging [161]. Most of the pristine nanotubes synthesized contain huge amount of amorphous carbon and metallic and ceramic impurities. Removal of these impurities is very difficult and often damages the tubes. Several techniques were applied to obtain impurity free SWCNTs [162]. Moreover, as synthesized SWCNTs contain both metallic and semiconducting nanotubes. A protocol has been established earlier [163] to optimize the acid purification process so that the content of the metallic tubes increases to a great extent. Same procedure has been applied in the present study to purify SWCNTs and enrich the tubes with metallic variety and briefly discussed below. SWCNT used in this study is a commercial variety (Elicarb) and has been procured from Thomas Swann & Co. Ltd, UK. Purification of pristine single-walled carbon nanotubes (SWCNT) and simultaneous enrichment with metallic nanotubes required HNO_3 (Merck, 98% GR), a moderate speed centrifuge **Figure 3.4** (PR – 24, Remi) and ultrasonic probe (230W, PR – 1000 MP, Oscar Ultrasonics) with Titanium horn. Conductivity grade water (<0.5 μS/cm) was produced from a quartz double distillation plant (AQDD.XL.RSH, Bhanu) and used for the acid treatment procedure.

Pristine SWCNTs (1gm) were added with 100ml Nitric acid(11 M) in a round bottom flask and attached with a reflux condenser. The solution was then refluxed using a heating mantel at 50°C for 20 hours. The setup was built in a fume -hood to exhaust acid fumes. The suspension was cooled to room temperature and centrifuged at 3500 rpm for 10 min after the reflux. The centrifugate was discarded, and the residue was redispersed in conductivity grade water (<0.5 μS/cm) produced from a quartz double distillation plant (AQDD.XL.RSH, Bhanu) and the residue was redispersed in distilled water by ultrasonication with ultrasonic probe, 230 watt (PR – 1000 MP,

Oscar Ultrasonics) and the step was repeated five times before the sol was centrifuged again at a higher speed of 10,000 rpm for 10 min for washing of SWCNTs. The process was repeated 5 times till no settlement found in the bottom of the centrifuge tube. The final sol has been observed to be stable **Figure 3.2** and was dried at 70°C and the solid samples were deposited on the petri dish as Bucky paper and marked as M-SWCNT (**Figure 3.3**).

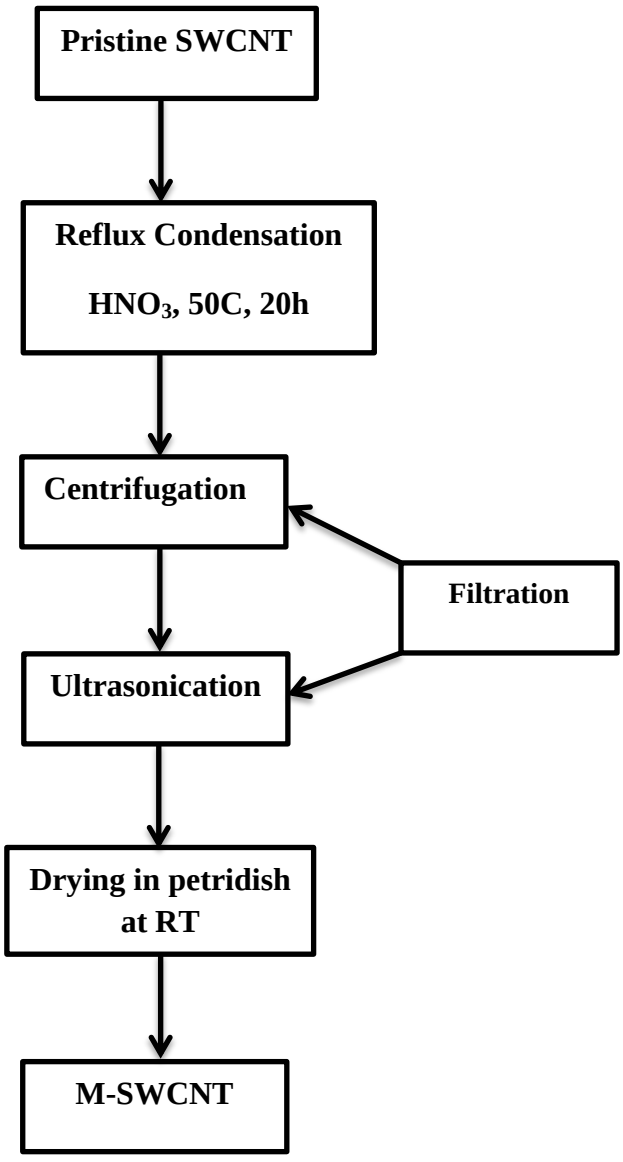

Figure 3.1.Flow Diagram of SWCNT purification

The enrichment of metallic SWCNTs (68%) in the product were confirmed from the analyses of Raman and optical spectra and the dc conductivity measurements [163].

Stabilities of the SWCNT sol in water is very high as observed from high ζ - potential value (-53mV) measured in Zetasizer (**Figure 3.7**).

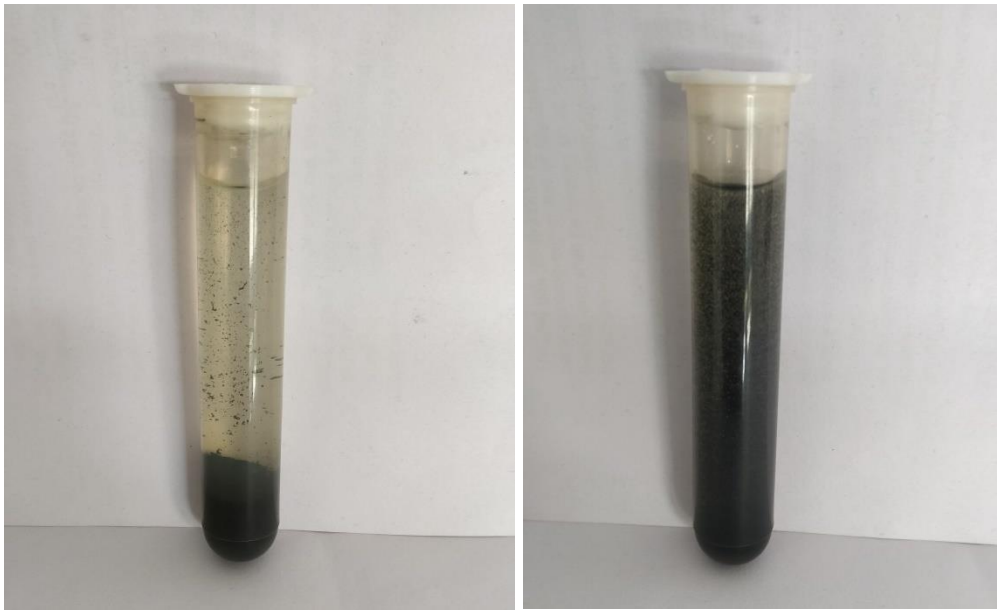

Figure 3.2. SWCNT dispersions (a) before and (b) 24h after purification.

Figure 3.3. SWCNT bucky paper (M-SWCNT) dried in ambient air after purification. The paper has been observed to have torn into pieces during transfer and have high reflectivity.

Purity and morphology of the tubes were also checked with a Transmission Electron Microscope (Tecnai G2 F30 ST 300kV, FEI).

Figure 3.4. REMI PR-24 Centrifuge.

Figure 3.5. Oscar Horn ultrasonicator with Titanium Probe.

3.1.1. FTIR Spectroscopy

Vibrational transitions of molecules or a combination of atoms in a molecule from lower to upper energy state is usually accompanied by an energy in the infrared (IR) region of the electromagnetic radiation. Energy absorbed (E_ν) could be written as,

$$E_\nu = h\nu \tag{6}$$

Where 'h' is the Planck constant and 'ν' is the frequency of the radiation.

Vibrational energy levels could be calculated for the molecular system from the equation of simple harmonic oscillator,

$$F = kx = -dV/dx \text{ or} \tag{7}$$

$$V = {}^{1}/_{2}\, kx^2 \tag{8}$$

Where 'F' is the restoring force 'x' is the displacement and 'k' is the force constant and 'V' is the potential energy.

Solving the Schrödinger Equation for the particle the permitted energy levels are

$$Ev = \left(v + {}^{1}/_{2}\right)\hbar\omega \tag{9}$$

Where, v= vibrational quantum no. and takes the value 0, 1, 2, 3……; $\omega = (k/m)^{1/2}$ and 'm' is the mass of the particle. For diatomic molecule of masses m_1 and m_2 the value of m will be the effective mass of the system 'm_{eff} '. Thus, the energies in terms of wavenumbers [G(ν)] becomes

$$Ev = hc\, G(v) \text{ and} \tag{10}$$

$$G(v) = (v + {}^{1}/_{2})\bar{\upsilon} \text{ where} \tag{11}$$

$$\bar{\upsilon} = 1/2\pi c(k/m_{eff})\, {}^{1}/_{2} \tag{12}$$

However, all molecular vibrations cannot be detected by infrared radiation. Selection rule governing the absorption of radiation states that only those vibrations are infrared active in which the electric dipole moment of the molecule changes during the displacement of the atoms relative to one another. Detection of '$\bar{\upsilon}$' is carried out in IR spectrometer by directing a source of radiation (HeNe Laser in the present study) to the sample and the absorption is measured by a detector which measures the intensities of the radiations at different frequencies generated by a dispersing element [164]. In Fourier Transform Infrared Spectrometer (FTIR) a Michelson interferometer is used to split the incoming beam to the detector into two components having a phase difference during their recombination. A path difference (p) is introduced in one of the components to split the beams and the detected signal oscillates as the two

components come into and out of phase as the path difference is changed. The corresponding radiation intensity in the wavenumber range $\bar{\upsilon}$ and $\bar{\upsilon}+\Delta\bar{\upsilon}$ may be written as

$$I(p,\bar{\upsilon})d\bar{\upsilon} = I(\bar{\upsilon})\,(1+\cos 2\pi\bar{\upsilon}p)\,d\bar{\upsilon} \tag{13}$$

The signal consists of radiations spanning a large number of wavenumbers and the total intensity at the detector is a combination of contributions from all the wavenumbers present in the signal.

$$I(p) = \int_0^\infty (p,\bar{\upsilon})d\bar{\upsilon} = \int_0^\infty I(\bar{\upsilon})(1+\cos 2\pi\bar{\upsilon}p)d\bar{\upsilon} \tag{14}$$

Finally, Fourier transformation is performed by means of a software and computer to find out *I*(p) from the equation

$$I(\bar{\upsilon}) = 4\int_0^\infty I(p) - \frac{1}{2}I(0)\cos 2\pi\bar{\upsilon}pdp \tag{15}$$

Fourier Transform Infrared Spectra (FTIR) has been obtained to find out the functional groups attached with the sidewalls and defect sites of SWCNTs. FTIR spectra of the SWCNT samples have been collected from Perkin Elmer, Spectrum 100 instrumemt. The instrument can operate over a range of 7800cm^{-1} to 370cm^{-1} with a resolution of 0.5cm^{-1}. It has a $LiTaO_3$ detector. A He-Ne Laser source of 633nm wavelength (max power Output 1mW) is used in the spectrometer [165]. Samples for FTIR analysis had been prepared by mixing thoroughly with KBr and then forming pellets.

3.1.2. Zeta Potential

Zeta potential is defined as the electric potential developed across the slipping plane surrounding the diffuse double layer of the sol particles relative to the bulk of the medium. Zeta potentials characterize primarily the stabilities of the dispersions in water and other media which were checked by Zetasizer NANO (ZSP) (Malvern) equipment. The equipment essentially operates by measuring the velocity (U_E) of the sol particles by laser Doppler velocimetry using Henry's equation 16.

$$U_E = \frac{2\varepsilon\zeta f(Ka)}{3\eta} \tag{16}$$

Where, U_E = Electrophoretic mobility of the charged particle

ε = Dielectric Constant

ζ = Zeta Potential

η = viscosity of the medium

f(Ka)= Henry's function (1.5 in the present case)

The zeta potential or charge of particles and molecules is determined by measuring their velocity (U_E) while they are moving towards an electrode due to electrophoresis if a field is applied. We simply measure the speed of movement, using laser Doppler electrophoresis, and then apply established theories to calculate the zeta potential. The zeta potential is an index of the magnitude of the electrostatic interaction between colloidal particles.

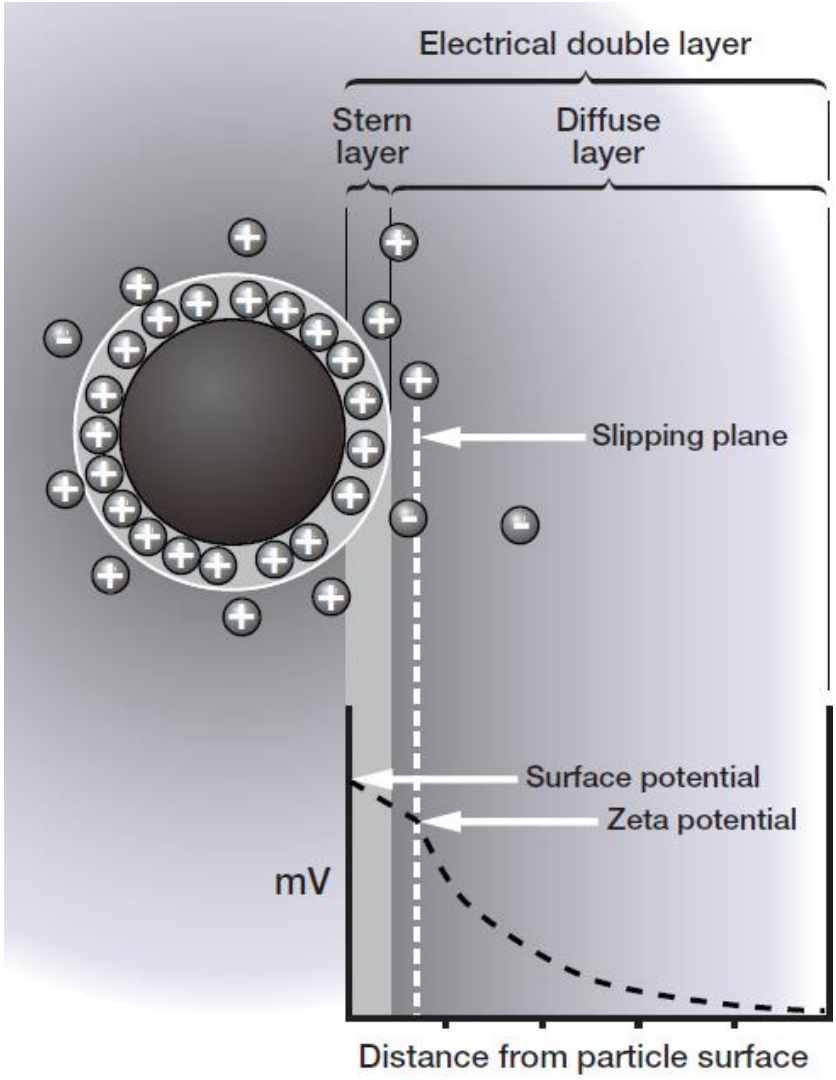

Figure 3.6. Schematic diagram of Electric Double Layer and Zeta potential [166].

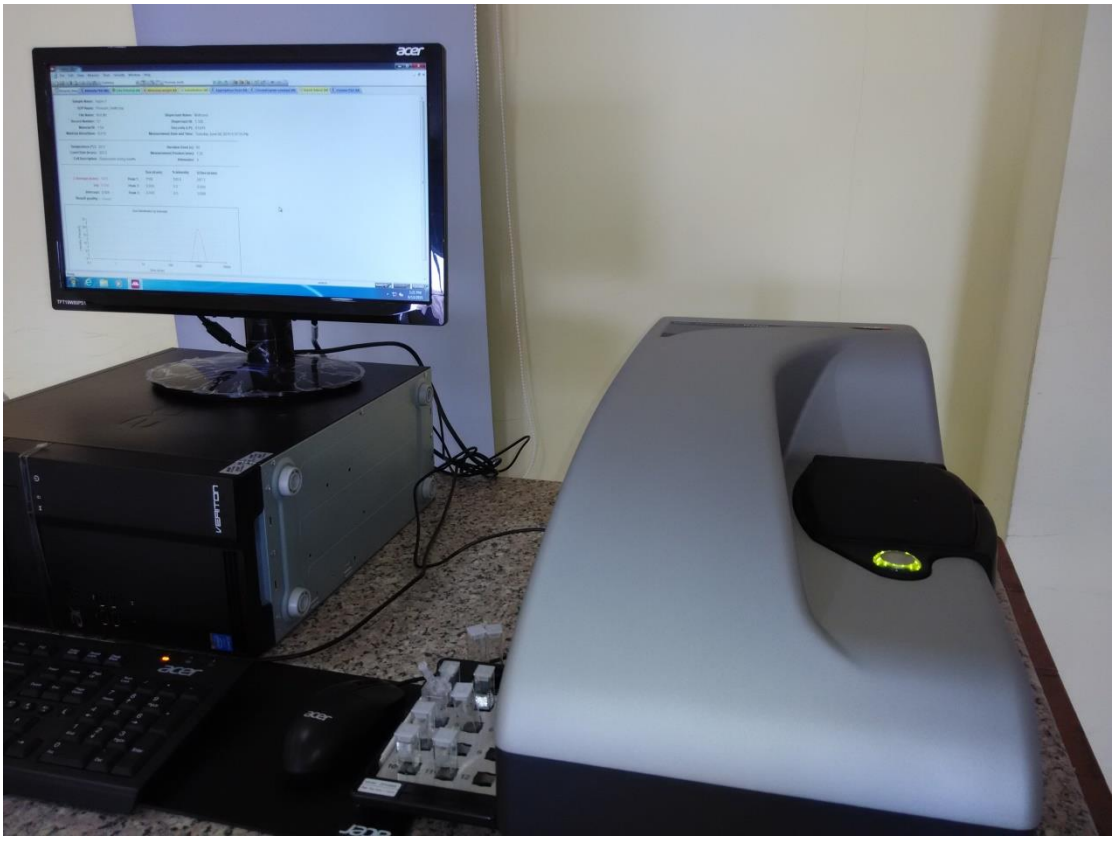

Figure 3.7. Zetasizer Nano ZSP (Malvern inc.).

3.1.3. Raman Spectroscopy

Raman spectroscopy of SWCNTs and the nanocomposites, a very useful tool for the characterization, has been used in the present study not only to characterize the nanotubes and the matrix material (AlN) but also to measure the residual stresses in the nanocomposite samples. Resonance Raman spectroscopy, in which the scattering efficiency gets enhanced by matching the laser excitation energy with that of the allowed optical transitions of electrons in SWCNTs is used for the analysis of samples in the present study. Raman spectroscopy is based on inelastic scattering of monochromatic radiation on the material. During this process energy is exchanged between the photon and the molecule such that the scattered photon is of higher or lower energy than the incident photon. The difference in energy is made up by a change in the rotational and vibrational energy of the molecule and gives information on its energy levels. When normal modes of vibration of molecules create change in polarization they become Raman active.

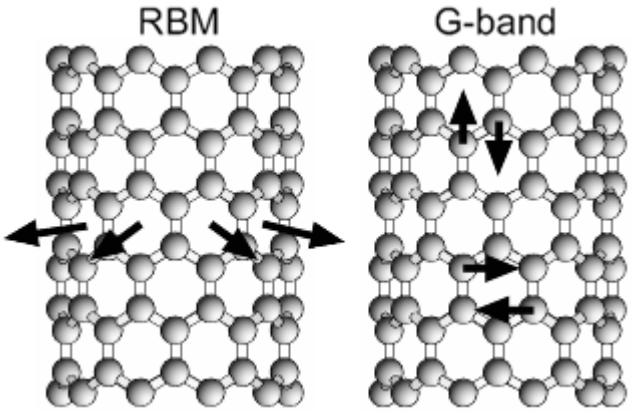

Figure 3.8. Atomic vibrations in SWCNTs for (a) Radial Breathing Mode and (b) Graphitic band (G- band) mode [167].

and a Confocal Raman optical Microscope (AIRIX Corp) with laser frequency of 530 nm respectively. The former one was mainly used to characterize the structure of the nanotubes and sintered AlN while the later was used to measure the residual stresses on the surfaces of the polished samples of the composites. A portion of Bucky paper prepared by the acid treatment method was deposited on a glass slide and examined under Raman microscope after focusing and scanning over the surface till good signals are obtained. The specifications for the Via Raman spectrophotometer are: Wavelength range: 200 nm to 2200 nm, Lasers supported: 229 nm to 1064 nm, Spectral resolution: 0.3 cm^{-1} (FWHM), spatial resolution (lateral) 0.25m, Spatial resolution (axial) < 1 m Highest typically necessary: 1 cm^{-1}, stability < ±0.01 cm^{-1}.

Confocal Raman optical Microscope AIRIX Corp had a laser frequency of 785 & 530 nm (532nm DPSS laser controller) laser spot size <1micron, laser depth size <2 micron [168].

Figure 3.9. STR 500 Confocal micro Raman spectrometer

Figure 3.10. Raman spectrometer attached with CCD

Polished samples of AlN and the nanocomposites were examined by focusing the plain surface and indents produced by a Vicker's diamond pyramid.

3.2. Preparation of AlN-SWCNT Composite

3.2.1. Pre hot pressing powder processing

AlN (HC Stark, Grade C), Y_2O_3 (99%, Indian Rare Earths Ltd.), Ethanol (Merck, GR) were used in this study. For preparing the initial dispersions of the ingredients, dried ethanol was chosen as the medium due to (i) its protic character and (ii) negligible hydrolysis of AlN particles in it. No external dispersant was added to minimize the impurity content in the material as much as possible. A horn sonicator (230W, Oscar Ultrasonics) was used to prevent the formation of agglomerates and a laboratory V-blender (Steadfast International) was used to disperse the powders in the media as much as possible for a duration of 18h. The stabilities of the dispersions of AlN, SWCNT, and Y_2O_3 in ethanol were checked by determining their zeta-potential values in Zetasizer Nano ZSP, Malvern. A rotary evaporator (Superfit) has been used to remove the solvent quickly with constant rotation and heating and a laboratory oven for final drying of the semi-dried mass at 70^oC for an hour. A controlled atmosphere glove box (Labconco) was used for the preparation of sols and suspensions under nitrogen atmosphere.

AlN powder (a typical batch of 14.5 gms) was mixed with dried ethanol and initially stirred with a magnetic stirrer (Remi). Purified SWCNT paper enriched with metallic variety tubes were also dispersed in ethanol separately with constant stirring by ultrasonication. Similarly, a sol of Y_2O_3 (1 vol% of Ethanol and 3.8vol% of AlN) was prepared in ethanol by dispersing with the help of magnetic stirrer and ultrasonication. The AlN dispersion was added to SWCNT sol (0.1% v/v) with constant stirring for 1h and a final ultrasonication having a pulse on-off time of 1min for a period of further 1h for maximum homogenisation. Y_2O_3 sol was then mixed with the homogenized suspension for a further period of 30min with constant stirring and subsequent ultrasonication for 1h. Upto this stage the processes were carried out in a controlled atmosphere glove box (Labconco, USA) to minimize the hydrolysis of AlN. The suspensions were sealed in polypropelene bottles containing Al_2O_3 grinding media inside the glove box and then transferred to a laboratory V- Blender. Blending was carried out for a period of 18h. Dried powder feedstocks were preserved under

nitrogen atmosphere in a controlled atmosphere Glove Box (Labconco, USA).AlN dispersion was added dropwise to the M-SWCNT sol (0.1 vol%) under continuous ultrasonication at a pulse on/off interval of 1 minute for a period of 1 hour at 27°C and finally the AlN-M-SWCNT dispersion was ultrasonicated for a further period of 30 minutes to ensure maximum homogenization. Y_2O_3 sol (1 vol% of ethanol and 3.8 wt% to AlN content) prepared in ethanol media separately was added slowly to the AlN-M-SWCNT dispersion with continuous stirring and sonication. The dispersion was further ultrasonicated for 30 minutes, ball milled using Al_2O_3 grinding media for 18 hours, and dried at 70°C in a rotary evaporator. The dried powder was hot pressed at 1850°C under N_2 atmosphere (FCT system) with 40 minutes dwell in a graphite die and punch (dia 36 mm) with a pressure of 35 MPa. Materials are labeled as ASN-0, ASN-1, ASN-3, and ASN-6 for 0, 1, 3, and 6 vol% loading of M-SWCNTs, respectively. Flow chart of process is presented in **Figure 3.11** below.

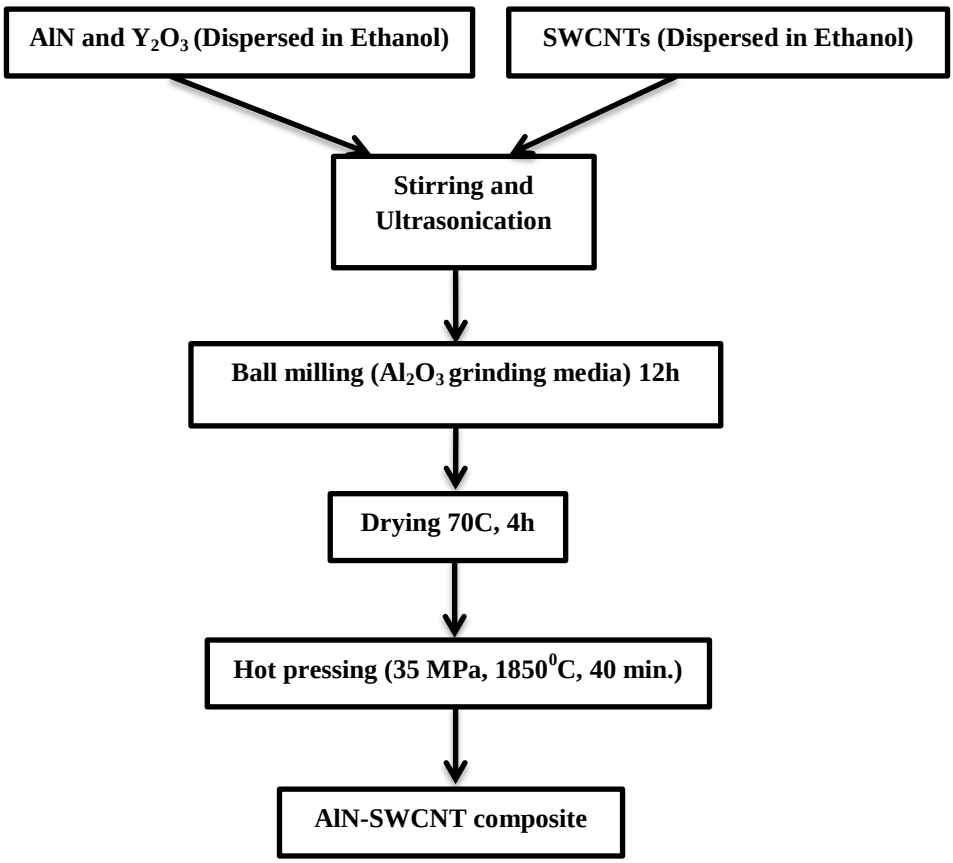

Figure 3.11. Flow chart for hot pressing of samples.

3.2.2. Hot pressing of powders

A high temperature vacuum hot press (**Figure 3.12**) (Model No. HPW315/400-2200-1000/PS, FCT System) was used to consolidate the powders under Nitrogen gas

(BOC, XL grade high purity nitrogen) and graphite die and punch (**Figure 3.13**). The hot press can operate upto 2200^{o}C under vacuum and controlled inert atmosphere (Ar/N_2) with the help of a graphite resistance heater. A graphite die (dia 36mm) and punch (**Figure 3.13**) was used for hot pressing the samples. The pressure on the punch was applied by means of a hydraulic assembly. The furnace is cold walled and the temperature is monitored and controlled by a W/W-Re thermocouple upto 1500^{o}C and then by a two color optical pyrometer. The whole process is automatic and programmable and controlled by a PLC controller.

Figure 3.12. FCT Hot press.

Figure 3.13. Graphite die with punch.

Hot pressing of samples were carried out by conventional method under high purity nitrogen atmosphere. Initially, after coating the inside wall of the die and the outside wall of the punches with BN suspension thin graphite foil (SIGRAFLEX®) was wrapped on the walls of the die. The feedstock powders were then introduced into the die and the punch was placed very slowly into the die so that the trapped air moves out. Graphite foil and BN coating were used to prevent any sticking of the die and punch during the hot pressing. The graphite die-punch assembly was then placed within the hot press and the alignment of the ram was checked. The furnace was then evacuated and purged with nitrogen gas thrice before filling it up with Nitrogen gas (XL grade BOC, India). The heating and cooling cycle is provided in **Figure 3.14** below. Pressure was applied through the ram slowly from 1600°C onwards. The pressure was released when the furnace started cooling.

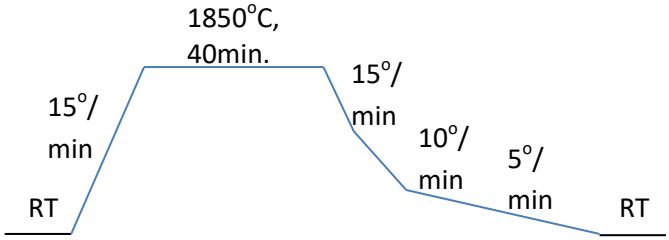

Figure 3.14. Program Cycle for the furnace heating and cooling during the hot pressing of samples.

Monolithic AlN samples containing no SWCNT and hot pressed under similar conditions are labelled as ASN-0 while the AlN-SWCNT nanocomposites as ASN-1, ASN-3 and ASN-6 for 1,3 and 6 vol% SWCNT addition. The hot pressing schedule **Figure 3.14** was chosen primarily after a few trial runs and the hot pressing and sintering temperature (1900^{o}C) usually followed earlier to sinter AlN [37,44], A moderately high heating and cooling rate (15^{o}C/min) and a temperature lower than the sintering temperature (1850°C) is chosen to minimize the damage of the tubes as far as possible.

3.3. Characterization of AlN-SWCNT nanocomposite

Different characterization techniques were used to analyze the AlN-SWCNT composite. The methods are discussed in subsequent subsections:

3.3.1. Density measurement

Bulk densities were measured by the Archimedes method with the help of a Mettler ME 100 balance with a hanging arrangement made for the purpose. The densities were measured after grinding the surfaces and peripheries of the discs to remove the graphite paper and other materials adhered to the surfaces and then cutting the hot pressed discs for obtaining square samples of dimensions appx 10mm x 10mm x 5mm. Distilled water (specific gravity=1.0) was used for the determination of bulk density by water displacement method.

$$\text{Bulk density} = \frac{\text{Dry weight}}{(\text{Soaked weight} - \text{immersed weight})}\,\text{gm/cc} \qquad (17)$$

Procedure for measuring density by Archimedes's principle is given below.

- Dry weight (W_1)
- With wire immersed weight(W_2)
- Wire weight (W_3)
- Actual Immersed weight (W_4) = W_3 - W_2
- Soaked weight (W_5)
- Bulk density = W_1 / W_5 - W_4
- Relative density = Bulk density / theoretical density * 100 %

Theoretical densities were calculated from the rule of mixture (ROM)

$$TD = V_{AIN} \cdot \rho_{AIN} + V_{SWCNT} \cdot \rho_{SWCNT} \qquad (18)$$

Here V_{AlN} = Volume fraction of AlN, V_{SWCNT} = Volume fracion of SWCNT, ρ_{AlN} = Density of AlN(3.21 g/cm^3) and ρ_{SWCNT} = Density of SWCNT(1.74 g/cm3) [169].

3.3.2. Phase identification using XRD

Phase analyses of ASN samples were carried out using X-ray diffraction measurements (XRD) in a X-ray diffraction (XRD) unit (PANAlytical) in the 2θ range from 0° to 90°. Cu Kα radiation was used for the analysis.

X-ray diffraction analysis utilizes the Bragg's equation for determining the atomic planes of a crystal which cause an incident beam of X-rays to scatter.

$$n\lambda = 2d\sin\theta \quad (19)$$

Where n=1,2,3……., for 1st, 2nd, 3rd etc. orders of transitions, 'd' is the lattice spacing and 'θ' is the glancing angle or Bragg angle. Constructive interference only occurs for certain θ's correlating to a (hkl) plane, specifically when the path difference is equal to 'n' wavelengths

Experimentally, the Bragg law can be utilized in two ways. By using x-rays of known wavelength λ and measuring θ, we can determine the spacing 'd' of various planes in a crystal [170].

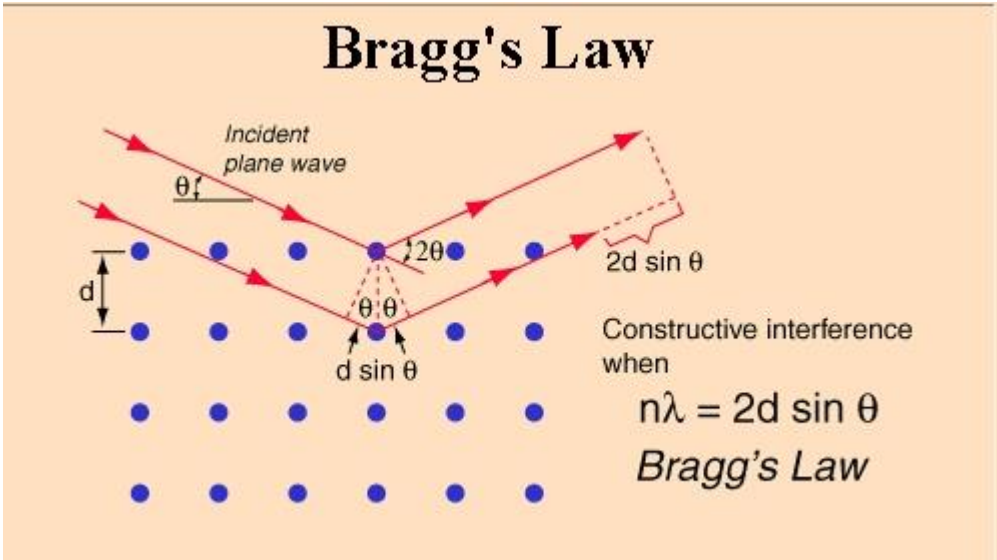

Figure 3.15. Schematic representation of X-ray diffraction [171].

3.3.3. Specimen preparation

Specimen preparation from the hot pressed nanocomposite discs for various characterizations was carried out by initially grinding the surfaces of the hot pressed discs with SiC and Diamond paper and then as follows:

(a) Sectioning

Diamond wafer cutting method has been used to cut the samples in 10x10x 5 mm dimensions for electrical characterization using "Buehler Diamond wafering blade series 15 LC Diamond" at 70 RPM for precise cut of samples. Small specimens were prepared for microstructure analysis by SEM and TEM as well as indentation hardness testing and fracture toughness measurements. For microstructure analysis and indentation hardness testing the following procedures were adopted.

(b) Mounting

Cold mounting method was used to mount the AlN and AlN-SWCNT composite. Araldite CY 230-1 (Huntsman) epoxy resin and Ardur HY 951(Huntsman) hardener were used in 8:1 ratio to cold mount the samples and after 24hr curing at room temperature mounted samples were further cured at 60^{o}C for 1 hr in oven to harden further during cooling. Cold mounted samples shown in **Figure 3.16** below.

Figure 3.16. cold mounted samples.

An automatic grinding and polishing unit **Figure 3.17** was used for ceramographic specimen preparation.

(c) Grinding and Polishing

The grinding procedure involved several stages, using a finer paper (higher number) each time. Each grinding stage removes the scratches from the previous coarser paper. This can be easily achieved by orienting the specimen perpendicular to the previous scratches. Between each grade the specimen is washed thoroughly with soapy water to prevent contamination from coarser grit present on the specimen surface.

Sectioned samples were ground and polished using Buehler Automet 250 automatic grinding polisher (**Figure 3.17**) Diamond grinding paper having grit sizes 30, 15, 9, & 6 µm and Buehler Micropolish II Alumina 0.3µm paste were used for grinding and polishing. A typical grinding and polishing schedule is presented in **Table 3.1** below.

Table 3.1. Grinding and polishing parameters.

Sr. No.	Grinding paper	load	RPM base	RPM head	time
1	30 micron	150 N	150	60	5 min
2	15 micron	150 N	150	60	5 min
3	9 micron	150 N	150	60	10 min
4	6 micron	150 N	150	60	5 min
Polishing					
5	1 micron	60 N	150	60	20 min
6	0.3 micron	60 N	150	60	15 min

Figure 3.17. Automatic grinding polishing.

3.3.4. Microstructure of nanocomposites using FESEM

An electron beam focuses onto the sample in a Scanning Electron Microscope (SEM). Simultaneously the beam scans across a selected sample area and signals are generated and being recorded by detectors forming an pixel by pixel image thereby. Valuable information about morphology, surface topology and composition was obtained SEM analysis. The characterization of CNTs and their distribution and homogeneity are significant concerns in the present study.

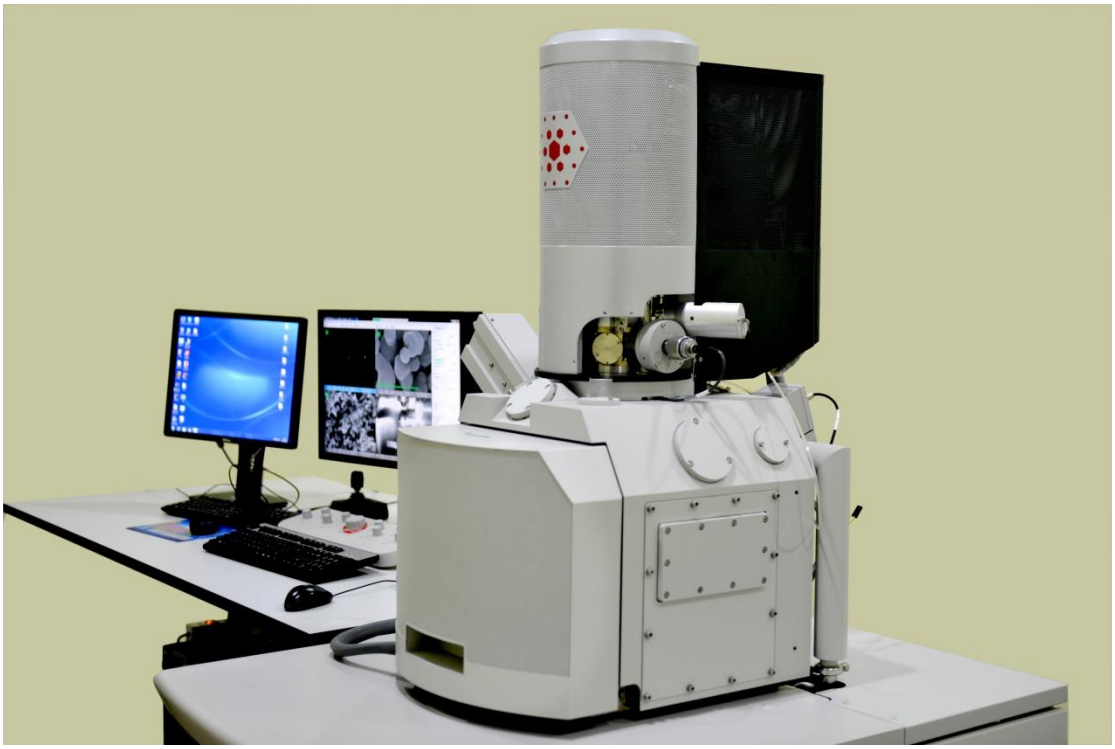

Figure 3.18. FESEM (Nova Nanosem 450).

Fracture surface topography of the composites have been analyzed by a Field Emission Scanning Electron micrographs (Zeiss Supra 35VP and Nova Nanosem 450 instruments) attached with Bruker EDS system for elemental analysis. Both Everhardt-Thornley (ETD) and In-Lens (TLD) secondary electron detectors were used for the voltage optimization (5–15kV) and contrast studies to obtain clear images of SWCNTs in fracture surface and grains in polished surface. Grain size measurements were carried out by lineal intercept method from the SEM micrographs of polished sections of the samples. The details of the method and results are provided in Appendix. Samples were polished by Buehler Automet 250 automatic grinding

polisher using Buehler Micropolish II Alumina 0.3µm paste as well as ion beam etching (GATAN Ilion II model 697) to reveal the grain boundaries.

3.3.5. Microstructure of nanocomposites using Transmission Electron microscopy(TEM)

TEM examinations of SWCNTs were obtained by placing very little portion of SWCNTs sandwitched between two holey copper grids. Thin foil specimens of the ceramics for the Transmission Electron Microscope (TEM) (Tecnai G2 F30 ST 300kV, FEI) images were prepared by standard techniques involving grinding (GATAN Disc Grinder 623), ultrasonic cutting (GATAN model 601), dimpling (Dimple grinder model 656) and ion beam etching (GATAN PIPS II model 695) of the samples.

Figure 3.19. Transmission Electron Microscope.

3.3.5.1. TEM sample preparation

TEM examinations of SWCNTs were obtained by placing very little portion of SWCNTs sandwitched between two holey copper grids.

Transmission electron microscopy (TEM) specimen must be of a suitable thickness in range of several hundred nanometers which also depend on the operating voltage of

the instrument. An ideal specimen is thin electronically transparent [172], representative of the bulk sample, stable, clean, flat with parallel sides and free of surface segregation. The sample preparation technique varies according to the nature of the material. Several steps were followed to prepare the thin foil samples of AlN-SWCNT composite for transmission electron microscopy.

1. **Preparation of thin slices**
2. **Preparation of 3mm discs**
3. **Thinning of discs**
4. **Dimpling**
5. **Ion beam etching**

1. Preparation of thin slices

Firstly the ceramic samples were cut into thin slices 10 x10 x2 mm using a diamond cutter. These samples were mounted on transparent glass slides using Araldite resin & hardener and then the samples on the slides were ground in a disc grinder on a diamond paper of 30 microns **Figure 3.21** till 300micron thickness is reached.

2. Preparation of 3mm discs

Ultrasonic cutter (Gatan model 601) is used for cutting the ceramic samples into 3mm dia which is shown in **Figure 3.20** below. Circular thin disc of 3mm diameter were ultrasonically cut using silicon carbide powder (40-50 micron) 320 grit size.

Figure 3.20. Ultrasonic cutter.

3.Thinning of discs

3mm discs were ground from 300 micron to ~80micron thin using (GATAN Disc grinder 623) in steps of 30, 15, & 6 micron diamond paper. Disc grinder with diamond paper on glass discs is shown below in **Figure 3.21.**

Figure 3.21. Disc grinder for TEM samples.

4. Dimpling

Mechanical dimpler (GATAN) uses a small radius tool to grind and polish the ceramic disc and form a crater having a fixed radius of curvature at the centre of the specimen. The dimple grinder is capable of producing final thickness <3μm in the center of the dimpled region. One can control the load, precisely and determine the depth of the dimple and interrupt the process to remove the sample for closer examination before continuing further.

5. Ion beam etching

Further thinning of the specimen was carried out in a Precision Ion Polishing apparatus (**Figure 3.22**, PIPS-II, GATAN). Ion milling is a sputtering technique in which the specimen is the target material and the process involves bombarding thin TEM specimens with energetic ions or neutral atoms (Ar) and sputtering out material from the specimen thin foil until it is thin enough to be studied in the TEM. The variable which can be controlled is voltage, temperature of the specimen, the nature of ion and the geometry (the angle of incidence). An accelerating electron of 2-5 KeV is used in the apparatus for penetration depth to the sample. A higher beam angle increases the ion induced surface damage, at low beam energies, commonly used for this specific application (<0.5 keV), stopping and range of ions in matter (SRIM) models show that the sputtering yields are very similar at high and low angles. The

ion beam will always penetrate the specimen to some extent which is minimized by inclining the incidence ion beam to the surface of specimen. Typical parameters are 5Kev in the earlier stage, 4Kev & 2 Kev, Gun tilt angle at 4degree, one gun at 2 degree for final stage polishing [173].

Figure 3.22. Ion beam polishing instrument

3.4.Electrical Properties

3.4.1. dc Resistivity measurement

Electrical resistivity (ρ) measurements were carried out by the standard four-probe method. Equally spaced four probes are connected with specimen with help of silver paste (Tedpella inc.) for better connectivity to measure I-V measurement. A schematic diagram of the setup is shown in **Figure 3.23**.

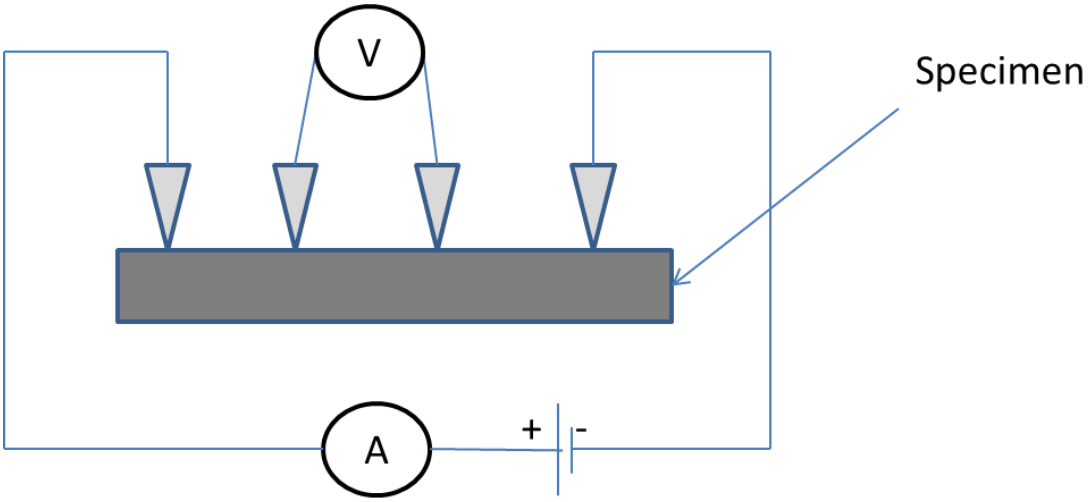

Figure 3.23. Schematic representation of four probe method.

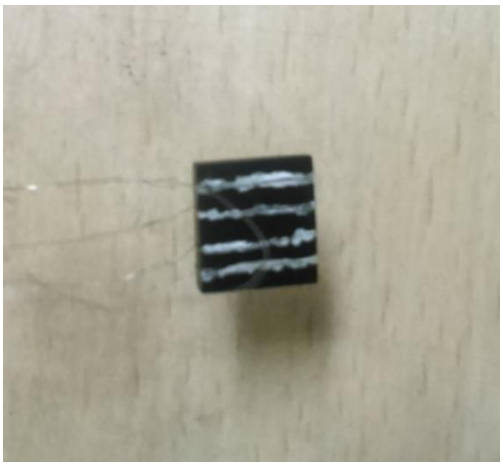

Figure 3.24. ASN-6 Sample with electrodes using silver paste.

DC resistivities of the polished samples (10×10×3mm) were measured by 4 probe technique using a precision current source (Keithley 6220) and a voltage measuring multimeter (HP3458A) connected with a cryostat. Electrode on samples were made using silver paint and silver wire used as electrodes and to dry electrodes curing was done under Na lamp. I-V characteristics were observed and then resistivity calculated using formulae i.e;

$$V = I * R \tag{20}$$

$$R = \rho \frac{l}{A} \tag{21}$$

Where R= resistance, I=Current applied, V=Voltage, ρ=Resistivity, l=length between electrodes & A=area of sample

3.4.2. Impedance measurement

Impedance and permittivity of the samples were measured with an impedance analyzer Agilent- E4991A equipped with a 16092A dielectric test fixture (**Figure 3.25**) in the frequency range (10^7 – 10^9 Hz). The dimensions of the samples are roughly 10mm X 10mm X 5mm. The terminal copper wires were connected with silver pastes on the sample surfaces. Three repeat experiments of the samples of each nanocomposite were analyzed to maximize the reliability of the data. A potential of 100mV was applied for the measurements.

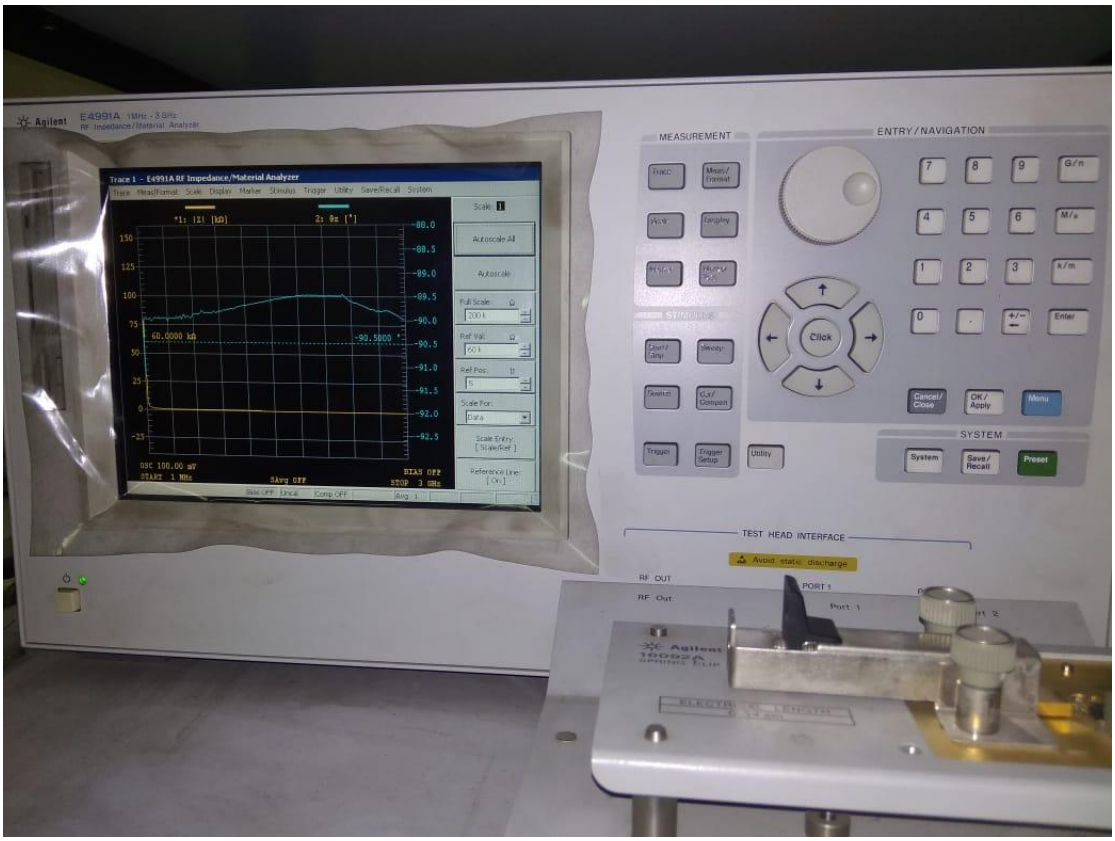

Figure 3.25. Agilent E4991A Impedance Analyser.

3.5. Thermal Conductivity measurement

Thermal conductivities were estimated from the diffusivity measured by laser flash technique (Flashline 4010, Anter Corporation, USA) after coating the samples with gold and subsequently with carbon paint at room temperature to 900°C. The samples for the thermal diffusivity measurements were prepared by slicing from the hot pressed disks, grinding and polishing of the cut specimens and subsequent coating of the samples with gold and carbon paints. Care was taken to make flat and parallel the

two opposite faces of the sample and accurate dimensions for precise measurements. The samples were of dimensions 10mm x 10mm x 3mm. Thermal conductivity has been calculated from the relation,

$$k = \rho C \alpha \quad (22)$$

where ρ is the sample density measured by water immersion method, C is the specific heat of the samples and α is the thermal diffusivity. Flashline 4010 has a facility to determine specific heat of the material by a comparison with standard graphite sample and ultimately produce the thermal conductivity alongwith the thermal diffusivity measurement.

The thermoelectric properties were measured by ZEM-3 ULVAC RIKO [**Figure 3.26**])

Figure 3.26. ZEM-3 ULVAC RIKO thermoelectric measurement instrument.

The efficiency of the conversion of thermal energy to electrical energy in thermoelectric devices is a function of several variables and has two components, the Carnot efficiency, which is the ratio of the temperature differential to the absolute temperature at the hot junction, and a dimensionless parameter known as the thermoelectric figure of merit, which is represented by ZT. Here,

$$Z = S^2 \sigma / k \quad (23)$$

where S is the thermoelectric power or Seebeck coefficient, σ and k are the electrical and thermal conductivities, respectively, and T is the absolute temperature [121].

3.6.Mechanical properties

3.6.1. Hardness measurement

Hardness is the resistance of materials to localized plastic deformation. Vickers micro hardness method is used to measure the hardness of ceramic samples. The technique employs the application of a load by a square based pyramid shape diamond indenter onto the surface of a test specimen. The shape of the indenter is shown in **Figure 3.27** below.

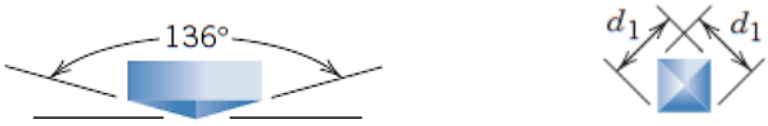

Figure 3.27. Shape of the indenter

We used the dwell time for diamond indenter 10 seconds and indentation speed 50µm/sec to perform the hardness test in a UHL, VMHT Instrument. The Vickers method involves an optical measurement system. Hardness value is calculated using the formula below:

$$HV = \frac{f}{A} = 1.854 * \frac{f}{{d_1}^2} \quad (24)$$

Where 'HV' is Vickers Hardness, 'f' is the applied load 'A' is the contact area of the pyramid and 'd_1' is the diagonal length usually in 'µm' in ceramics. The value '1.854' is the geometrical constant for a regular square based pyramid having apex angle 136^o in **Figure 3.27** An average of six measurements has been taken for determining the hardness in a particular load in the present study.

Figure 3.28. (a) Vickers micro-hardness instrument (b) Mounted Sample for measurement

Vicker's indentations were made onto the well-polished flat ceramic surfaces. Length of the diagonals and the cracks developed from the corners of the indents were measured by micrometer eyepieces of the instrument through the help of an, in-built, software and the images were stored in a computer.

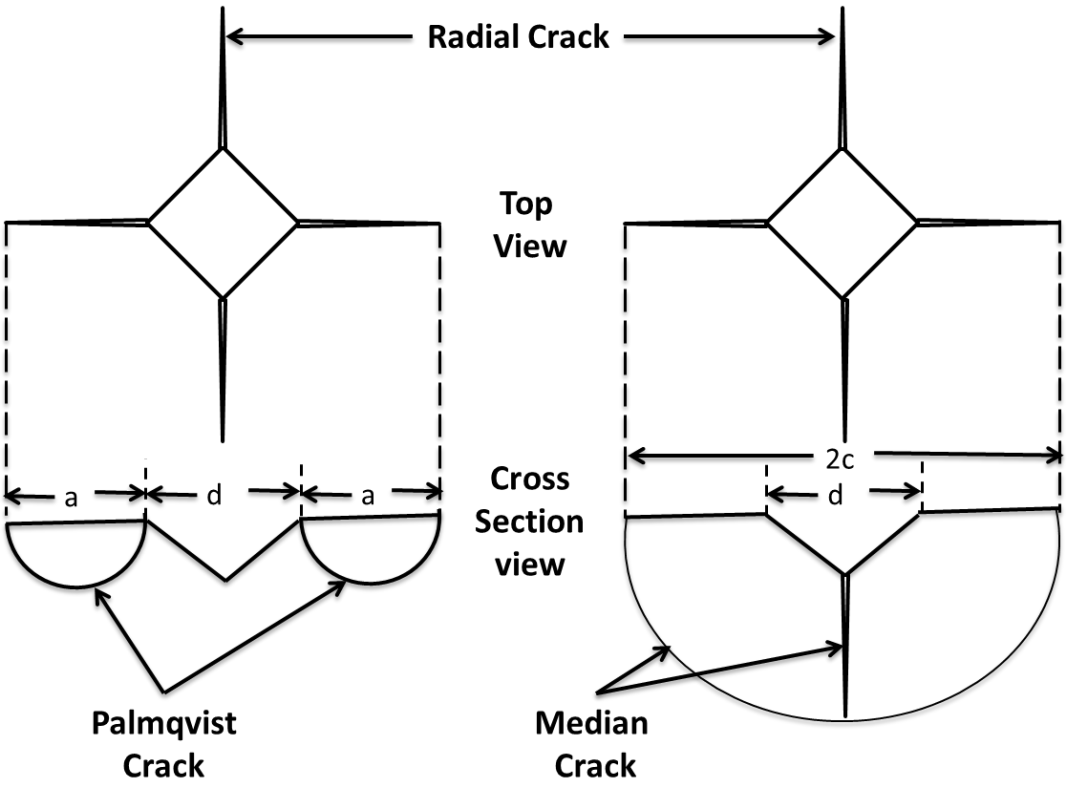

Figure 3.29. A typical Vickers indent[174]

A schematic Vicker's indent along with the cracks are shown in **Figure 3.29.**

3.6.2. Fracture Toughness

The fracture toughness (K_{IC}) of ceramic systems are evaluated using the direct crack measurement (DCM), indentation strength in bending (ISB) and single edge notched beam (SENB) methods. Conveniently, the fracture toughness of ceramics is measured by using a Vickers indentation known as "indentation fracture toughness". Considering the ease of determination of fracture toughness by indentation fracture method and the requirement of very small specimen size of the material a preliminary analysis of the fracture toughness (K_{IC}) of the AlN-SWCNT nanocomposites and the comparison with that of monolithic AlN processed under similar conditions has been performed in this study. This method is based on the size of median/radial cracks emanating from the median planes containing the applied load axis. The cracks are measured from the two extreme ends passing through center of the indent at loads beyond the critical load required for crack initiation. Finally, clear radial/mean cracks were considered for the measurement since it had been established that lateral cracks

often interfere in measuring K_{IC}. In this technique, the fracture toughness could be calculated using Anstis equation (Eq. 25) [175]:

$$K_{IC} = 0.016 \frac{E^{1/2}}{H} \frac{P}{C^{3/2}} \quad (25)$$

Where '2c' is the crack length from the centre of the indent, 'E' is the elastic modulus, 'P' is the indentation load and 'H' is the hardness. Thus, 'K_{IC}' has the unit $MPa.m^{-1/2}$. Hardness, 'H' is determined from equation (24) while Young's modulus has been estimated by rule of mixture from the bulk density and experimental density obtained for of AlN/3.8wt% Y_2O_3 (300MPa) [37] and SWCNT (1TPa) [11].

.

Chapter 4

Densification and Microstructure of AlN-SWCNT nanocomposites

This chapter discusses about the densification and microstructure development of AlN-SWCNT nanocomposite in the present study. Preparation of aluminum nitride (AlN)-single walled carbon nanotube (SWCNT) ceramic-matrix composite containing 0,1,3 & 6 vol% SWCNT by hot pressing and the development of microstructure thereby have been discussed in Chapter 3.

4.1. Introduction

Densification of ceramic-CNT composites is very difficult unless special techniques of sintering like hot pressing or spark plasma sintering is applied in which rate of heating could be very high so that the CNTs are not destroyed during sintering. Apparently, CNT retards grain growth during the sintering process [83,100,176,177]. It has been argued that CNT having a large aspect ratio imposes different constraining effect by forming networks surrounding the grains of Al_2O_3 which leads to maximum reduction of the grain growth in comparison to spherical carbon black inclusion [177]. CNT addition has been shown to reduce the sintering temperature of Al_2O_3 for complete densification [177]. Recent study shows that the grain growth rate exponent during the sintering of PSZ-MWCNT composite is almost 3 and, therefore, follow a model considering the drag of CNT resisting the densification [178].

4.2. Characterization of SWCNT

4.2.1. Zeta Potential measurement

The stabilities of the dispersions of AlN, SWCNT and Y_2O_3 in ethanol were checked by determining their zeta-potential values (Zetasizer ZSP, Malvern). A high negative zeta potential value of -38 mV of the ethanol sol of SWCNTs indicated negative surface charge created by the $–COO^-$ ions and the consequent electrostatic stabilization of the SWCNT sol in protic ethanol. The zeta potentials of AlN and Y_2O_3 were positive and the values are +20mV and +24mV respectively in Ethanol. Since the SWCNTs after HNO_3 treatment shows negative charge on its surface and AlN and Y_2O_3 both shows positive charge so it helps in immobilization of SWCNTs on AlN powder and homogeneous mixing. The electrostatic attraction between $–COO^-$

groups on the surface of SWCNTs and $AlOH_2^+$ present on the surface of AlN particles in protic solvents should lead to better bonding of the SWCNTs with the AlN particles under controlled colloidal procedure adopted in the present protocol.

4.2.2. FTIR Spectroscopy of SWCNT

FTIR spectroscopy has been performed in the range 500 to 4000/cm^{-1} for the identification of the functional group attached on the surface of the SWCNTs. The structural characteristics of the molecules has been understood with FTIR results. Acid treatment produced $–COO^-$ ions on the surface of SWCNTs as indicated from the peak at 1732 cm^{-1} in the FTIR spectra shown in **Figure 4.1** below. Apart from $–COO^-$ group presence of OH, C-H, N-O and C-O vibrations are also present.

Thus, FTIR spectrum indicates the presence of –COOH functional group in the purified SWCNTs.

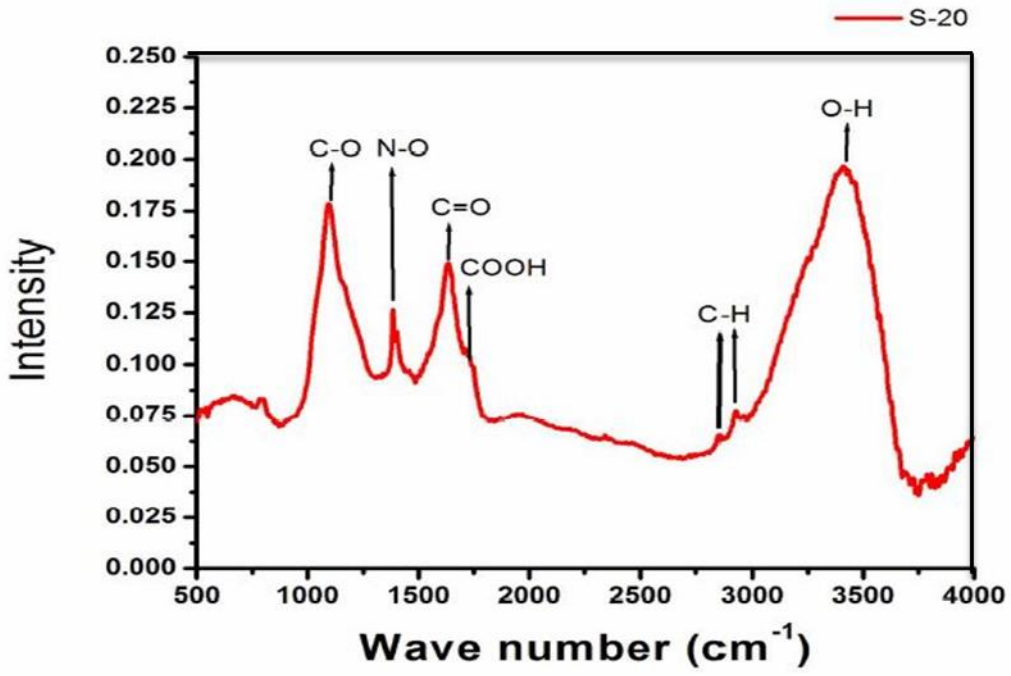

Figure 4.1. FTIR spectrum of SWCNT after purification

4.2.3. Raman Spectroscopy of SWCNT

Raman spectra of the SWCNT samples were analyzed using a Renishaw-in Via Raman microscope with a laser frequency of 785nm. The samples were at first focused in the microscope and then the Raman scattering data was collected when the peaks are strong enough to distinguish during scanning over the surface.

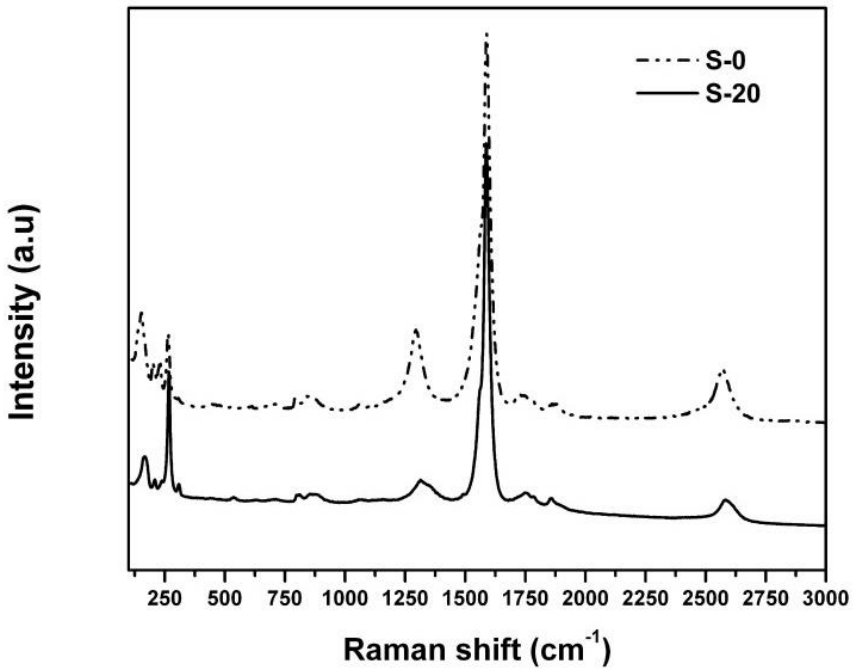

Figure 4.2. Raman spectra of pristine and purified SWCNT.

Raman spectra show that the peak due to ideal graphitic lattice band (G-band) appeared at 1588cm^{-1} while the disordered lattice band at 1300cm^{-1}. The ratio of the intensities of these two bands (I_D/I_G) is a measure of the disorderness in the structure of the nanotube and presence of amorphous impurities in the sample [167]. The ratio is 0.05 for the purified nanotubes (S-20 in **Figure 4.2**) and 0.19 for the pristine tubes (S-0 in Figure 4.3) which indicate that the parameters of the reflux process adopted in the present study did not damage the structure of the nanotubes but removed the carbonaceous impurities to a great extent. Thus, Raman spectra analysis show the production pure SWCNTs by the optimized process of acid treatment in the present study. Radial Breathing Mode (RBM) Raman lines are used to determine the diameter of the SWCNTs by the relation, $d_t = 248/\omega_{RBM}$ [179,180] after deconvolution of the peaks assuming Lorenzian line shapes (**Figure 4.3**).

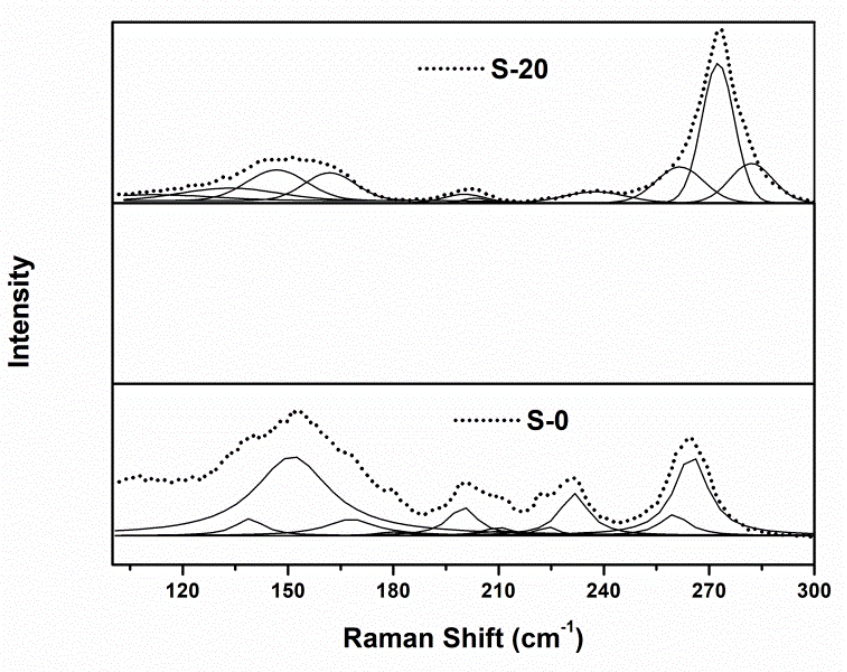

Figure 4.3. Deconvoluted RBM Raman peaks of pristine (S-0) and purified SWCNTs [163].

It could be noticed from **Figure 4.3** that the distributions of tube diameters are changed after purification. Both pristine and purified tubes have similar range of diameters from 0.9 to 1.78nm while the purified tubes (S-20) have mostly small diameter (~0.9nm) and narrow size distribution the pristine tube varieties (S-0) have mostly around 1.68nm diameter.

4.2.4. Optical Spectra

Finally the metallic character of the tubes was determined from the optical spectra. Optical spectra (UV-Vis) of aqueous dispersion of the nanotubes have been obtained by dilution and transferring of the suspensions to a concentration of 3microgram/mL. The spectra were acquired with a scan speed of 125nm/min. The data were corrected for π-plasmon background as reported in earlier publications [163]. The spectra show the appearance of strong peak at 405nm which corresponds to M_{11} transitions of metallic SWCNTs in the purified samples (S-20).

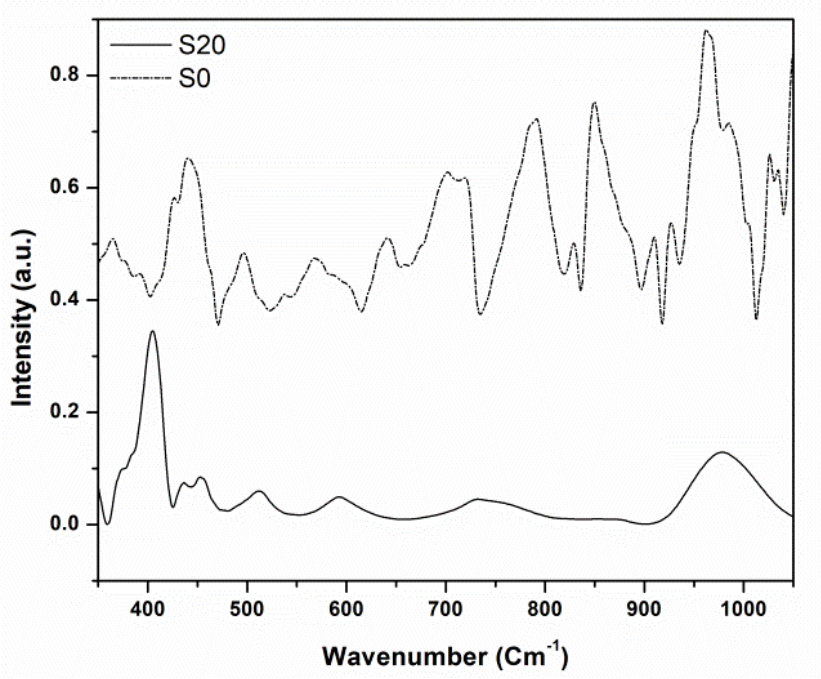

Figure 4.4. UV-Vis spectra of pristine (S0) and purified (S20) SWCNTs.

4.2.5. Transmission Electron Microscopy (TEM) of SWCNT

TEM image of purified SWCNTs were compared with pristine SWCNTs in **Figure 4.5.**

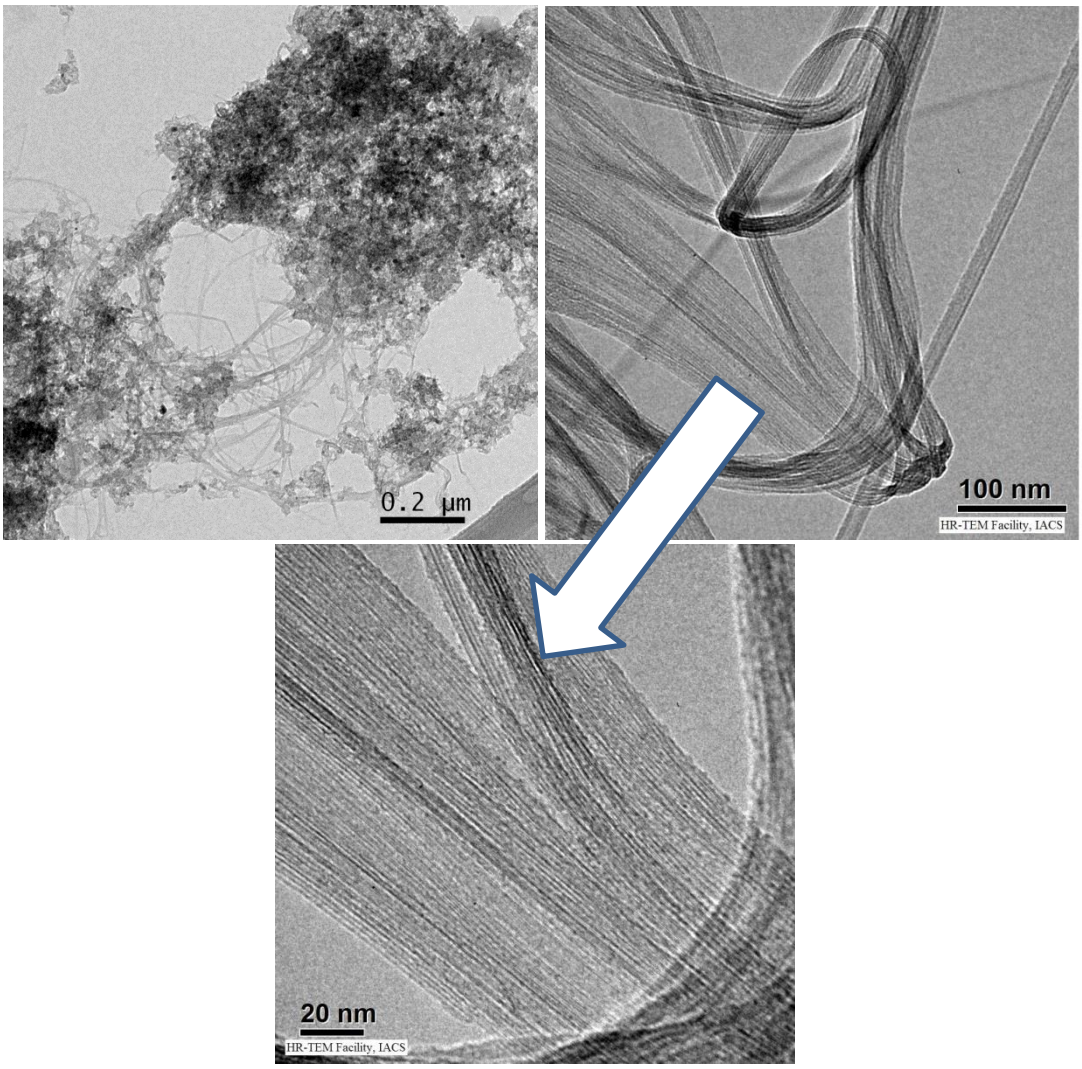

Figure 4.5. TEM images of (a) Pristine (b) purified SWCNTs and (c) High Resolution images of a magnified portion of (b) indicated by white arrow.

Thus, FTIR, Raman, UV spectra and TEM images show that the starting feedstock SWCNTs in the present study are purified and functionalized with $-COO^{-}$ groups which enable high dispersion of the tubes in protic solvents as evident from the zeta potential measurements. Moreover, these tubes contain higher metallic varieties and lower diameter than those of pristine sample.

4.3.Hot Pressing of samples

Figure 4.6. Hot pressed sample

4.3.1. Density of the hot pressed material

Hot pressed AlN-SWCNT composite disc is shown in **Figure 4.6**. Bulk densities of the nancomposite samples (**Table 4.1**) show that highly dense composite samples were obtained after hot pressing. Density of monolithic AlN material (ASN-0) hot pressed under similar conditions are also provided for comparison. Five measurements were taken to arrive at the average values of the densities. Calculated theoretical densities of the samples are also presented in **Table 4.1** below.

Table 4.1. Densities of AlN and AlN-SWCNT nanocomposites

Sample Name	Theoretical density	Experimental bulk density	Relative Density (%)
ASN-0	3.33	3.27	98
ASN-1	3.31	3.28	99
ASN-3	3.28	3.26	99
ASN-6	3.23	3.22	99

Similar high relative densities (>95%) were obtained by many authors to prepare composites like Si_3N_4-MWCNT [100] and Al_2O_3 – MWCNT [181]. Higher sintering temperatures (>1900°C) are needed for obtaining >99% RD in sintering monolithic AlN with the addition of similar amount of additive (~4 wt%) in the literature [37,182]. Almost 99% relative density has been achieved in hot pressing AlN powder

(d_{50}- 1µm, purity - 99.99%) at 1700°C with a hold of 60min [183]. Hot pressing of AlN powder (particle size -0.8 – 1.5 µm) with 5wt% Y_2O_3 and 10wt% Graphene particles at 1900°C for 2h produced a 99% RD [184]. We have intentionally kept the temperature almost 100°C below the usual sintering temperature (1900 -1950°C) of AlN [37,182,184] so that the effect of the addition of SWCNTs could be distinctly visualized. Primary reason for the high densification is the lower grain coarsening and growth in the process adopted in the present study as discussed earlier [185].

4.3.2. Phase Evaluation by X-ray Diffraction (XRD)

X-ray diffraction patterns of ASN-0, ASN-1, ASN-3, and ASN-6 samples are shown in **Figure 4.7**. Inverted arrow markers represent the reflections from the planes of cubic $Y_3Al_5O_{12}$ (YAG) (JCPDS Card No. 01-088-2047) and indexing of AlN by JCPDF card no. 00-008-0262 in **Figure 4.7** below. YAG is formed at high temperature by the chemical reaction of Y_2O_3 and Al_2O_3 formed on the surface of AlN particles at high temperature in accordance with the binary phase equilibrium Y_2O_3- Al_2O_3 [186].

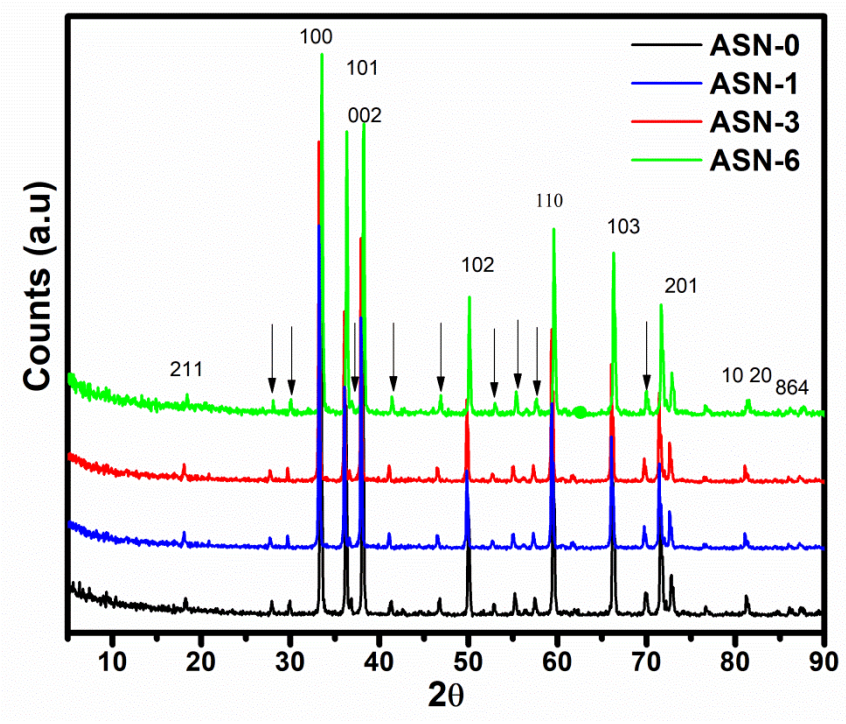

Figure 4.7. XRD patterns of ASN-0, ASN-1, ASN-3 and ASN-6.

4.3.3. Raman spectroscopy of AlN-SWCNT nanocomposites

Raman signals of M-SWCNTs (S-20) and the AlN composites with 0, 1, 3 & 6 vol% addition of SWCNT's are presented in **Figure 4.8**. AlN materials for the purpose to define SWCNT survivability after high temperature hot pressing and for stress studies were done using piezo spectroscopic means.

The ratio of the normalised intensities (I_D/I_G) of the D–band (1300 cm^{-1}) and G–band (1588 cm^{-1}), an indicator of the presence of either defect structure or amorphous carbonaceous material are 0.05, 0.05, 0.16 and 0.21 for S-20, ASN–1, ASN–3 and ASN–6 samples respectively. Other Raman lines include the zone center phonon frequencies of AlN (hexagonal wurtzite) represented by A1 (TO) at 611 cm^{-1} and E2 (High) at 657 cm^{-1} in **Figure 4.8** below. Thus, Raman spectra clearly show high survivability of SWCNTs in the composites during high temperature hot pressing conditions.

.

Table 4.2. I_D/I_G ratio

I_D /I_G	**Sample**
0.05	Purified SWCNT
0.05	ASN -1(1 vol% SWCNT)
0.16	ASN-3 (3 vol% SWCNT)
0.21	ASN-6 (6 vol% SWCNT)

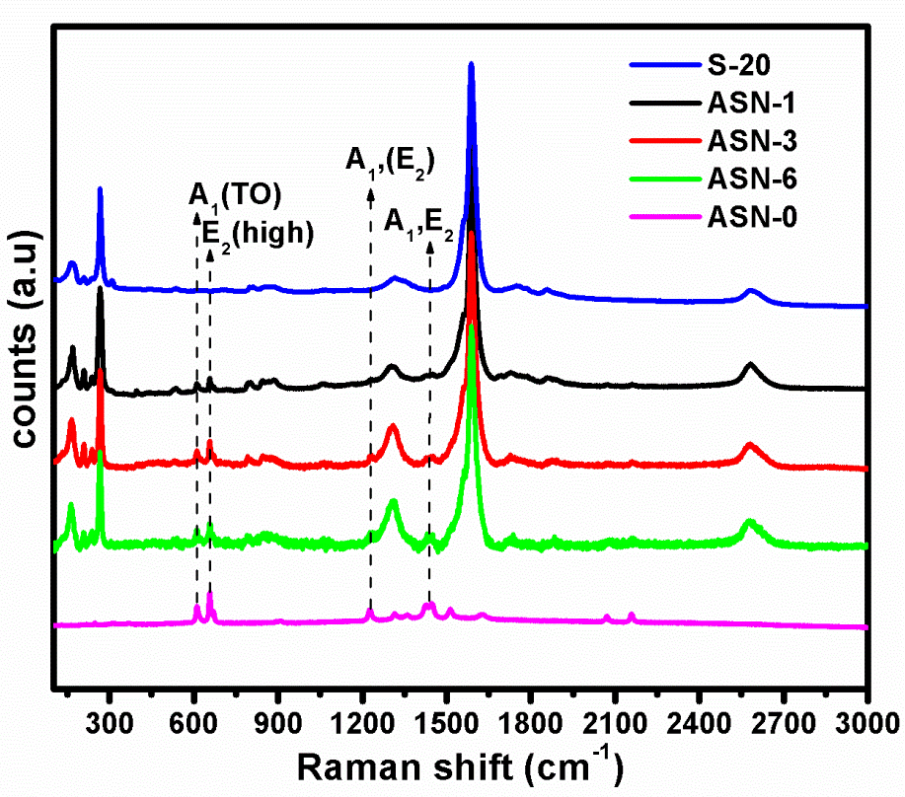

Figure 4.8. Raman spectra of composite samples.

4.3.4. Scanning Electron Microscopy

Fracture surfaces of hot pressed samples are shown in **Figure 4.9** below which confirms the densification and decrease of porosity with the addition of SWCNT in AlN matrix supporting the trend in relative densities revealed by density determination by water displacement method described in Section 3.3.1.

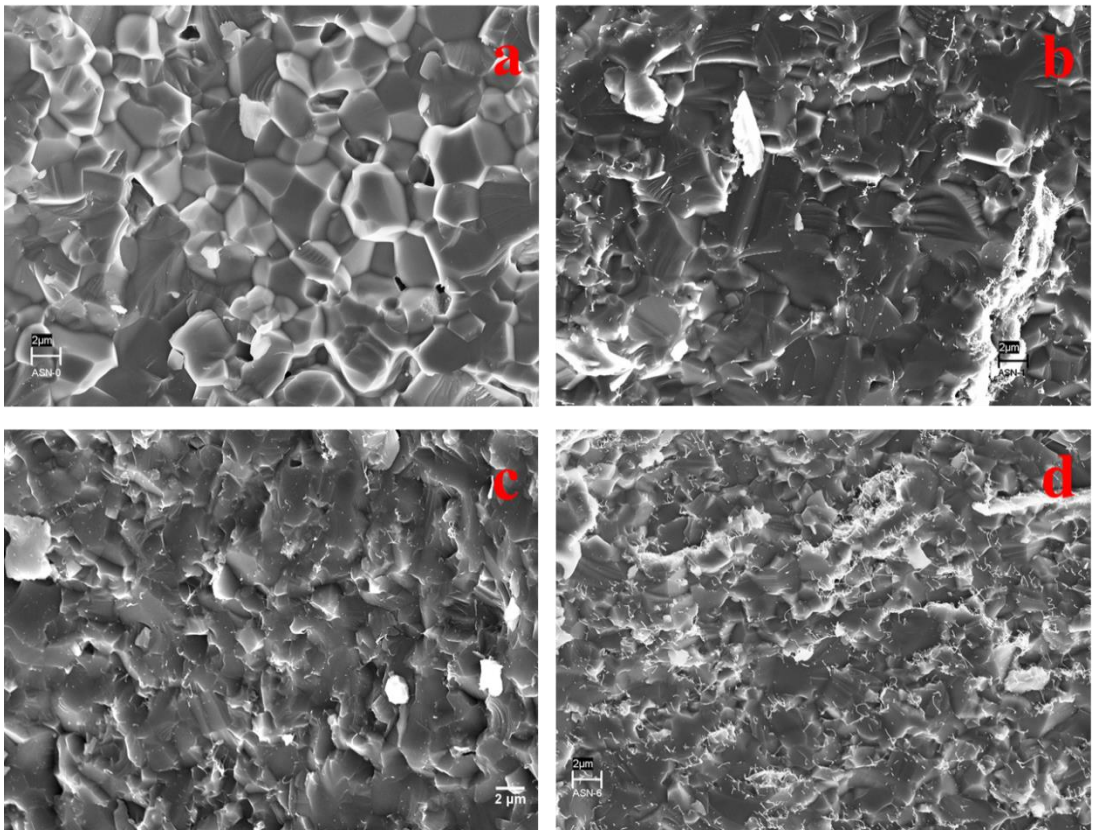

Figure 4.9. SEM Micrographs of fracture surfaces of samples

(a) ASN-0, (b) ASN-1, (c) ASN-3, & (d) ASN-6.

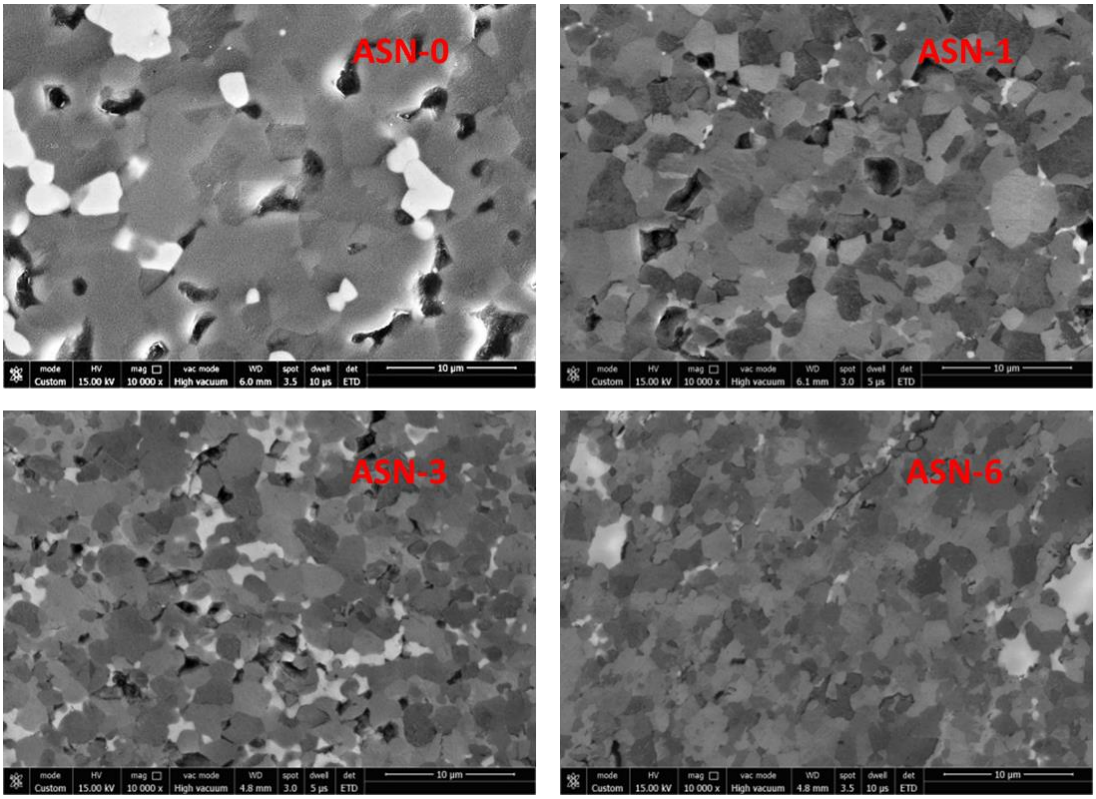

Figure 4.10. SEM Micrographs of polished sections of samples (a) ASN-0, (b) ASN-1, (c) ASN-3, & (d) ASN-6

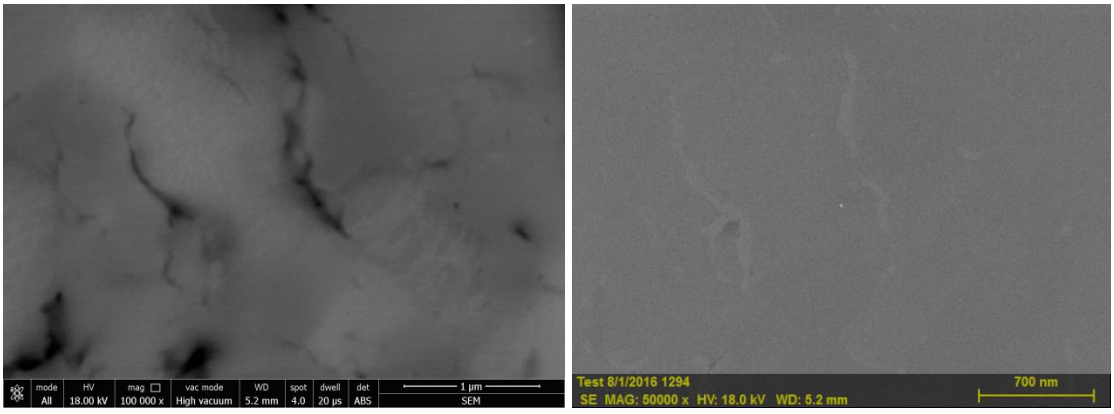

Figure 4.11. SEM micrograph polished section of ASN-6 in (a) BSE and (b) EDS mode showing occurrence of long SWCNT ropes.

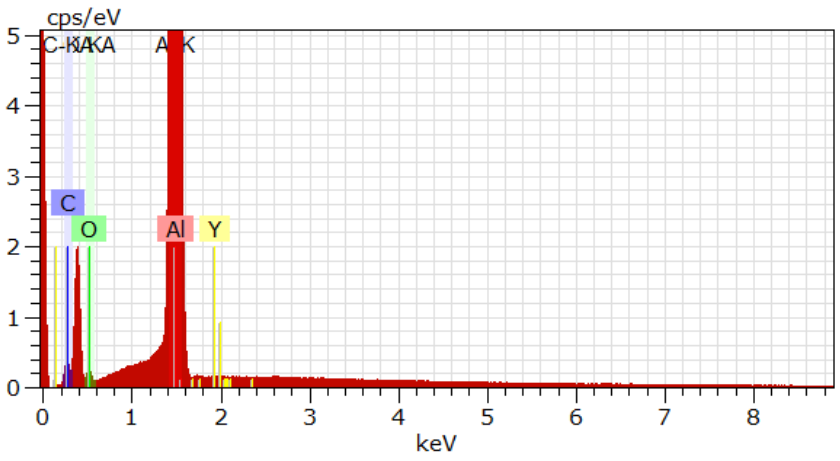

Figure 4.12. EDS spectra of **Figure 4.11**.

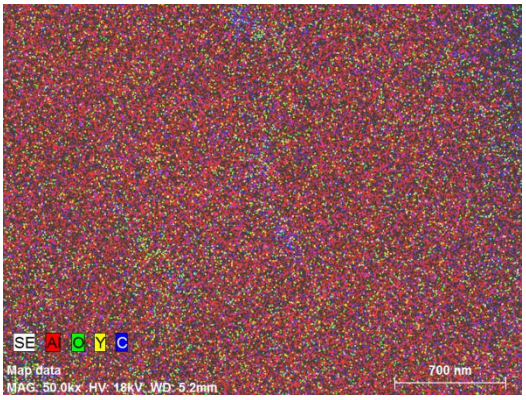

Figure 4.13. Overall EDS mapping showing long SWCNT bundle present occasionally in ASN-6.

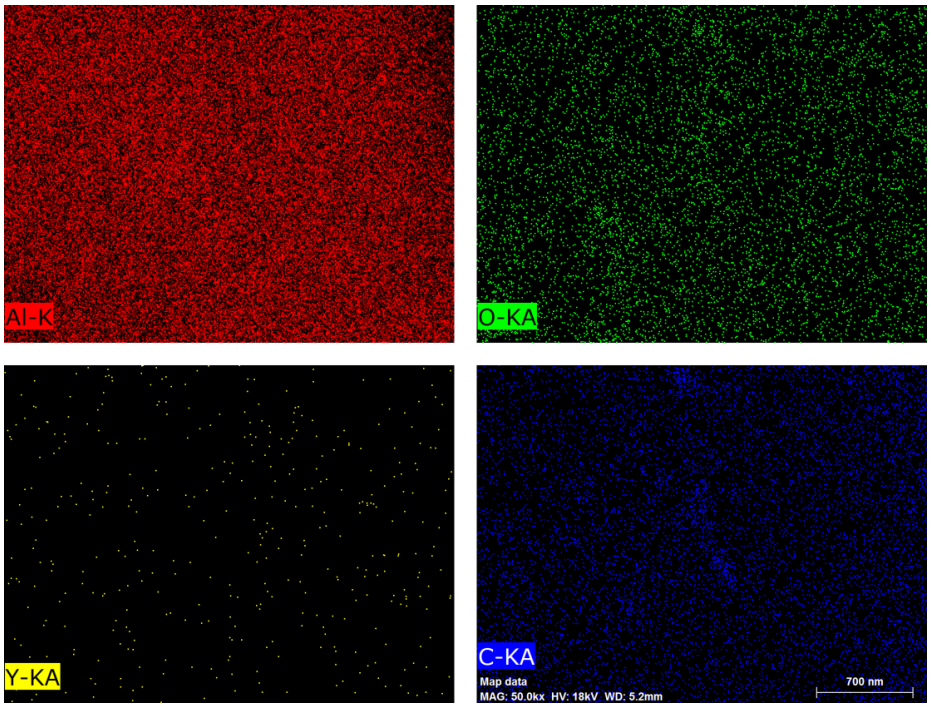

Figure 4.14. EDS elemental maps for Al, O, Y and C.

4.3.5. TEM (Transmission electron microscopy)

Transmission electron microscope images of thin foils of the nanocomposites are presented in **Figure 4.15**. It could be observed that SWCNT ropes/nets are spread along the boundaries of AlN grains. Lattice fringes of HRTEM image were confirmed with AlN JCPDF card 00-008-0262.

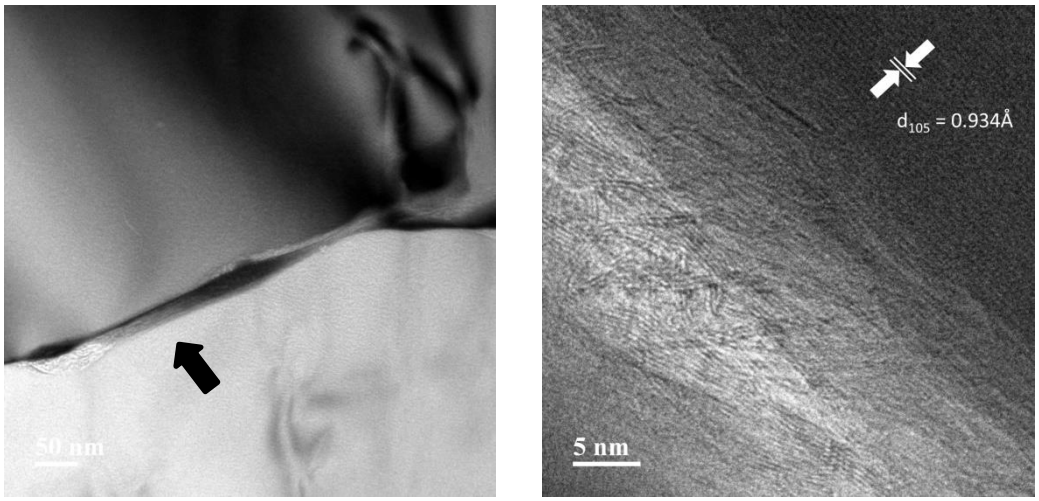

Figure 4.15. (a) TEM image of cross section of ASN-6 (b) HRTEM image of the grain boundary marked with black arrow in (a). The sample has been sliced parallel to the hot pressing axis.

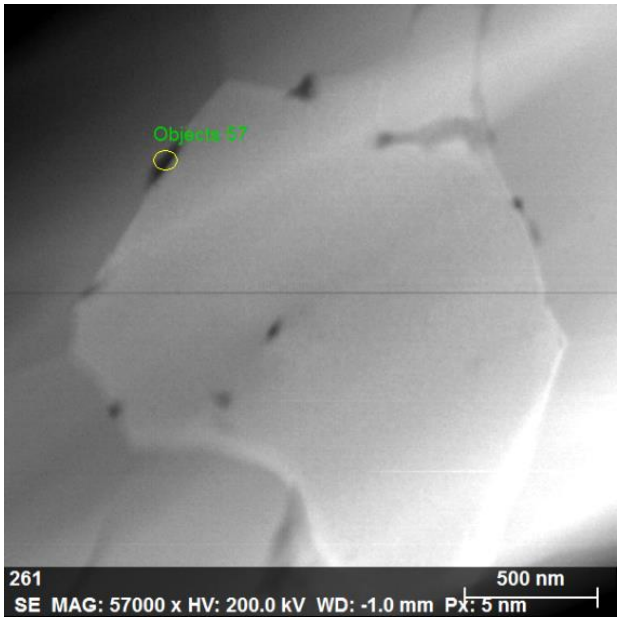

Figure 4.16. TEM EDS.

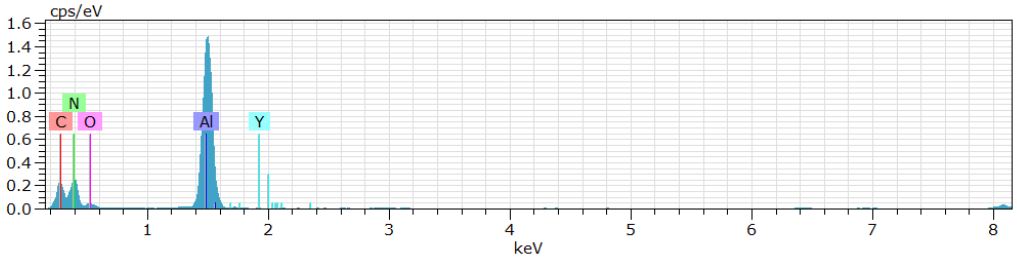

Figure 4.17. TEM EDS of selected area.

Table 4.3. Elemental analysis of **Figure 4.16**.

El	AN	Series	unn. C [wt.%]	norm. C [wt.%]	Atom. C [at.%]	Error (1 Sigma) [wt.%]
C	6	K-series	48.70	48.70	62.23	2.06
Al	13	K-series	34.44	34.44	19.59	1.11
N	7	K-series	15.24	15.24	16.70	0.64
O	8	K-series	1.51	1.51	1.45	0.13
Y	39	K-series	0.11	0.11	0.02	0.07
		Total:	100.00	100.00	100.00	

High carbon content and a little Y_2O_3 could be noticed from the EDS results on the grain boundary shown in **Figure 4.17**. Thus, the EDS results indicate the possibility of the presence of a Y-Al-O-N liquid formation at high temperature which is transient

and assists the rearrangement and intermediate diffusion assisted material transport from the high to low energy regions.

It could be observed from the density values and microstructure analysis by SEM that the sintering kinetics improved significantly with the addition of SWCNTs since the relative density of AlN is lower than those of the nanocomposite samples. Closed pores are clearly visible in the SEM micrograph of the fracture surface of monolithic AlN (ASN-0), which are almost absent in the nanocomposite samples. Sintering temperature is, therefore, much reduced for the composites. Similar results have been observed in densification Si_3N_4-nitrogen doped CNT composite by earlier researchers [187]. Particle rearrangement induced by the liquid phase formation had been attributed for the lowering of sintering temperature [187]. A point may be mentioned, in this respect, that the distribution of Yttrium containing phases identified by white areas in the micrographs of polished sections **(Figure 4.10**) is more in the nanocomposites than in the monolithic AlN where large patches are present. SWCNT bundles might have acted as conduit for the transport of liquid phases in the grain boundaries by acting as channels. Secondly, the grain sliding during hot pressing is smoother in composites than that in the monolithic AlN. High compressibility of SWCNTs makes the sliding of grains in the composite much easier while the sliding gets hindrance from the higher friction of the AlN grains in monolithic AlN similar to that proposed earlier during the preparation of ZrO_2-CNT composites [188]. Grain growth is also reduced with the addition of SWCNTs which helps the densification. CNT drag may be a reason for the grain growth inhibition. I_D/I_G ratio remaining low even after the addition of 6vol% SWCNT and TEM examination of the grain boundary phases clearly indicate the survivability of the structure and intertwining of the SWCNTs along the grain boundaries.

Chapter 5

Electrical Properties of AlN-SWCNT composite

The addition of CNTs for improving electrical conductivity of ceramics is widely appreciated. Aluminum Nitride is inherently an wideband gap semiconductor (electrical conductivity: 10^{-12} S/m). Adding a small amount of CNT (1 vol%) to AlN can make it electrically conductive (6 S/m). A detailed literature review is presented elsewhere (section 2.5.1). This chapter discuss about, the electrical properties of aluminum nitride – SWCNT nanocomposite. The effect of grain size and temperature conditions on the electrical conductivity of the aluminum nitride – SWCNT nanocomposites was also studied. For AlN – SWCNT nanocomposites, electrical conductivities were also measured as a function of temperature. Impedance spectroscopy also performed to check the circuit design into composite.

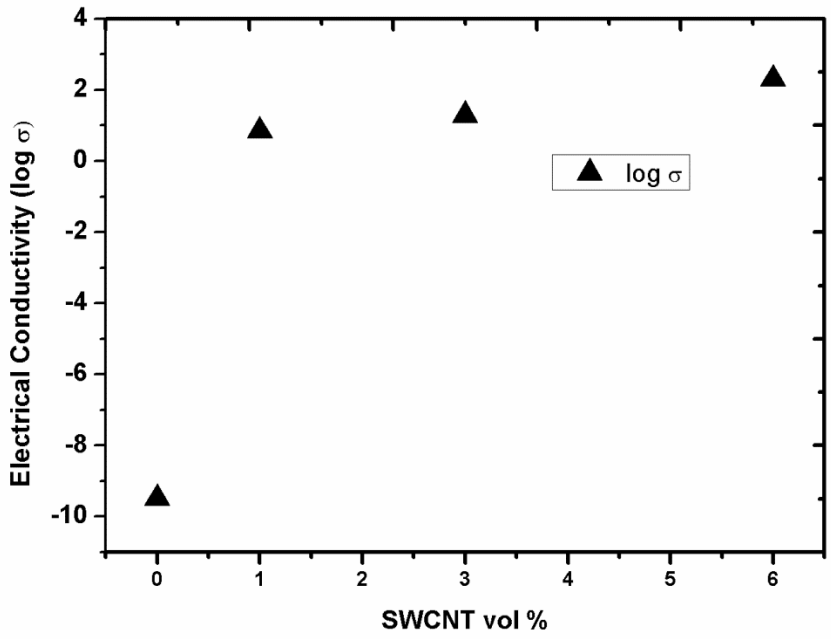

Figure 5.1. Electrical conductivity at room temperature.

Electrical conductivity of ASN-6 is 200 $S.m^{-1}$ (Highest electrical conductivity among non-oxide ceramics- SWCNT composites).

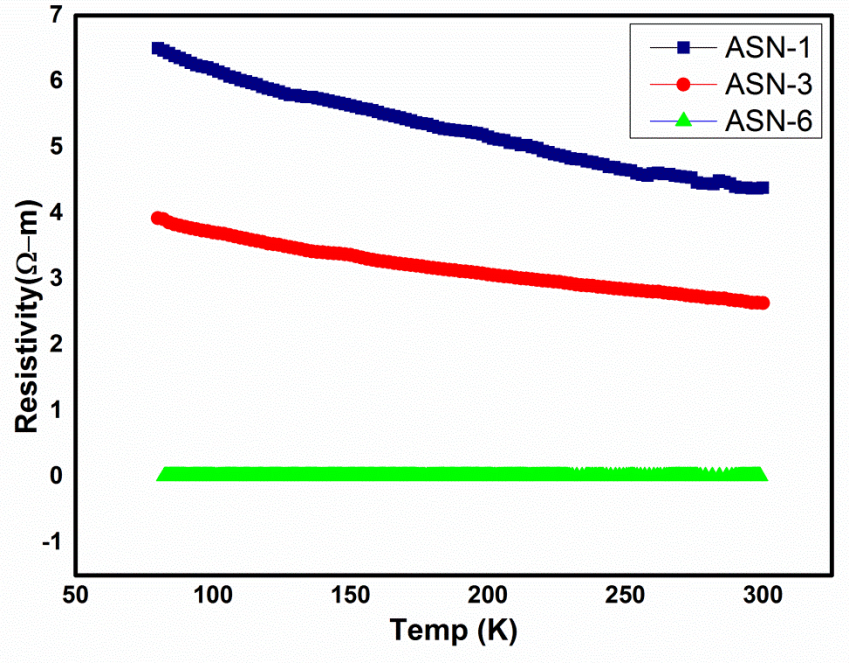

Figure 5.2. Variation of dc electrical resistivities with temperature.

3D connectivity of the ropes could be established from the images taken both in parallel and perpendicular to the hot pressing direction **Figure 5.9**. Thus, the electrical conduction in these composites seems to be dominated by these conducting pathways made by SWCNTs along the boundaries of AlN grains [marked by white arrows in **Figure 5.6**]. Presence of large diameter ropes in some of the areas along grain boundaries [**Figure 5.9(c)**] might have led to fluctuations in the conductivity values.

5.1. Variable Range Hopping model

Variable range hopping (VRH) models to envisage the electron hopping mechanism in composites, Variable range hopping mechanism was given by N.F Mott. (1969) [189] to explain dimensionality of conduction in material at low temperature.

When conduction between localized states near fermi level E_f is by hopping is mott conductivity, the temperature dependence of the conductivity is given by

$$\sigma = \sigma_o e^{-\left(\frac{T}{T_o}\right)^{-\frac{1}{(n+1)}}} \quad (26)$$

VRH was proposed by Mott in 1969 [189]. VRH models were obtained by plotting $\ln(\rho T^{-1/2})$ as a function of $T^{-1/(n+1)}$, where n = 1, 2, or 3 indicate the dimensionality of the sample

AlN- SWCNT matrix composites conductivity plots shows 3D conductivity in VRH models

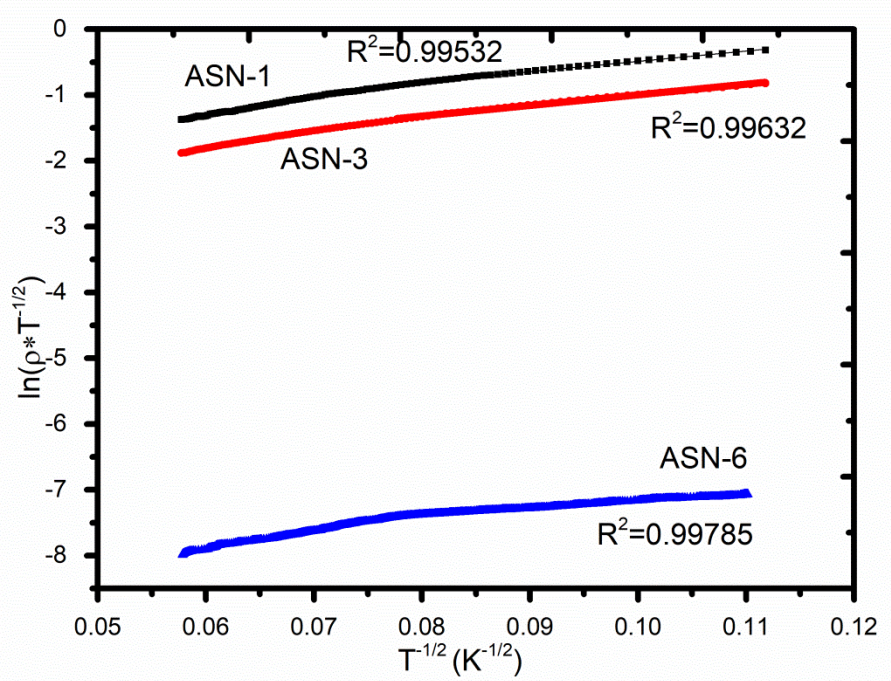

Figure 5.3. Resistivity values in accordance with 1D VRH model.

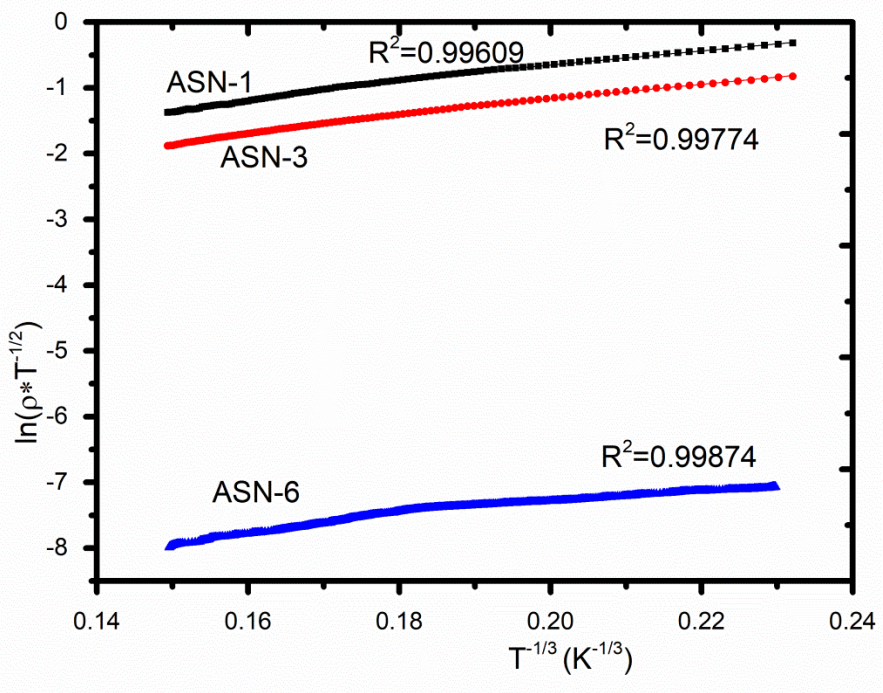

Figure 5.4. Resistivity values in accordance with 2D VRH.

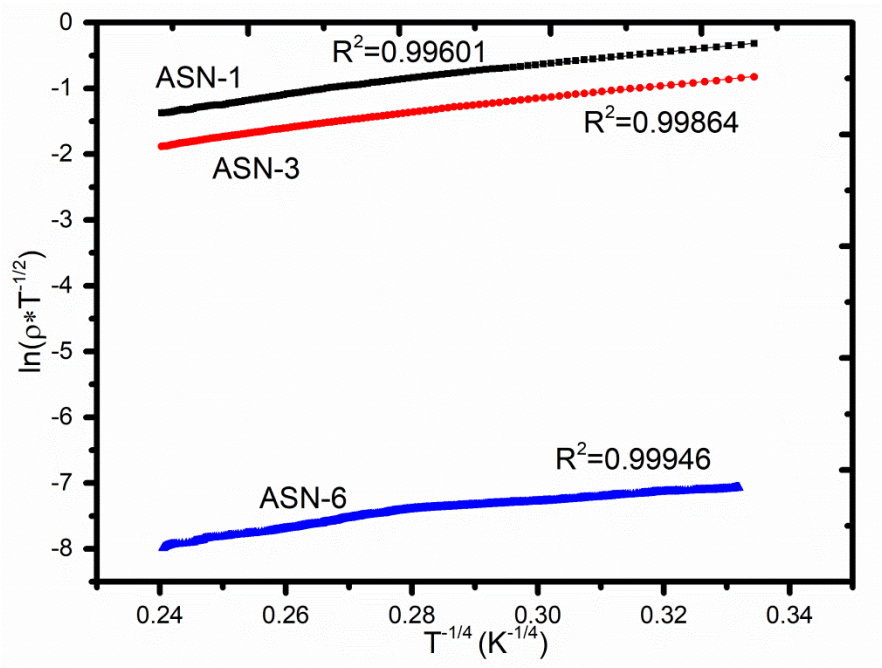

Figure 5.5. Resistivity values in accordance with 3D VRH model.

as shown in **Figure 5.5**. Fitting the linear region of the preceding plot provides an understanding into the conductivity mechanism that prevails within the sample. The most effective fit corresponds to the one with the best correlation (R^2). For the AlN–SWCNT composite, the value of the regression coefficient was found to be highest for the linear portion in the 3D VRH model fitting, indicating that the electron hopping mechanism in the AlN–SWCNT composite occurs in three dimensions which is confirmed by SEM and TEM images. Formerly reported studies with reference to electron conduction mechanisms in ceramic-CNT composites, 1D VRH is the most noticeable form of charge transport [190]. This arises from the expected charge tunneling property of CNT. Charge transport is assisted in the bulk sample through these 3D charge paths as a result of the homogenization mixing of SWCNT in AlN matrix.

5.2.Percolation Theory

A significant theory for understanding conductivity within composite materials, especially where the ceramics matrix and the dispersoids have very different characteristics, is the concept of percolation. Percolation theory [191] suggests the increase of the electrical conductivity σ of the composites with the increasing CNT volume fraction should follow to the scaling law $\sigma = k(p - p_c)^t$, with p the volume

fraction of CNT and p_c the critical volume fraction corresponding to the percolation threshold. The exponent " t " reflects the dimensionality of the system.

A percolating level below 1vol% SWCNT content in the composite and a high value of the dc electrical conductivity ($200Sm^{-1}$) in ASN-6 sample have been observed [185]. The value is highest among the published results for non-oxide ceramic-SWCNT composites containing 6vol% SWCNT [185]. Conductivity increase with nanotube contents in the composite could be explained by the reduction of intertube spacing, higher connectivity of the conducting network and increased intertube tunneling of electrons as proposed earlier for a percolative behavior [109,192]. The temperature dependences of the electrical conductivities have been analysed to gain better insight of the mechanism of the electrical conduction in our samples.

Figure 5.2 shows the least dependence of electrical resistivities of ASN-6 samples with temperature while electrical conductivities of ASN-1 and 3 increases with temperature indicating a behaviour similar to the semiconductors. **Figure 5.7** shows that the conductance of the composites normalized with the value at 300K with temperature increases with temperature. Interestingly the conductivities of all the composites could be extrapolated to non-zero values at 0K indicating free charge carriers requiring no thermal activation. This is a signature of the metallic behaviour of the composites. Temperature independent conductivity has been observed in ASN-6 upto 175K and then an increasing trend or hopping behaviour.

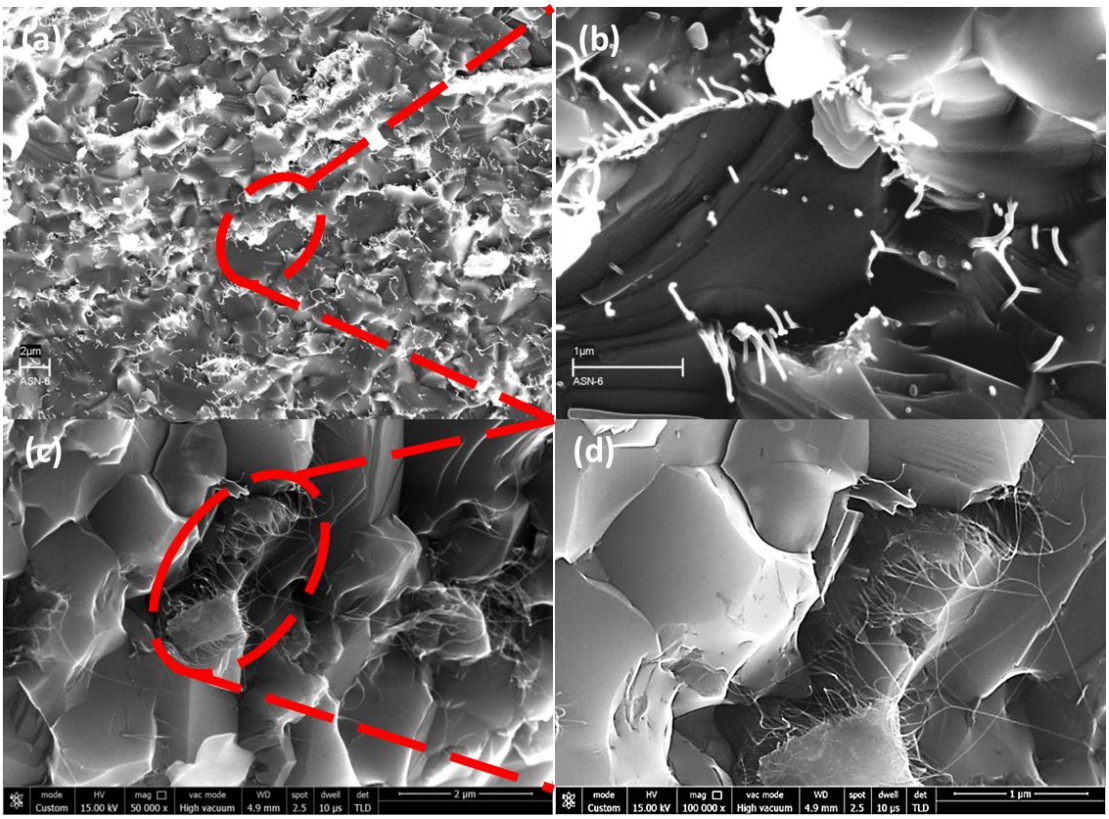

Figure 5.6. FESEM micrograph of the fracture surface of ASN-6 showing formation of nanotube nets around grains of AlN. Micrographs taken from (a) ETD detector at 20kV and (c) from TLD detector at 15kV. Red circles indicate the positions of enlargements for higher magnification micrographs (b) and (d).

The electrical conduction in the present AlN-SWCNT composite is, therefore, similar to that of SWCNT nets or mesh and follow a hopping transport indicating an increase of conductivity with temperature Ropes of SWCNTs form 2D architecture in the form of nets or mesh. These nets surround the grains of polycrystalline ceramics building a 3D network [67]. The formation of nanotube nets at grain boundaries could be confirmed from the FESEM micrograph **Figure 5.6**.

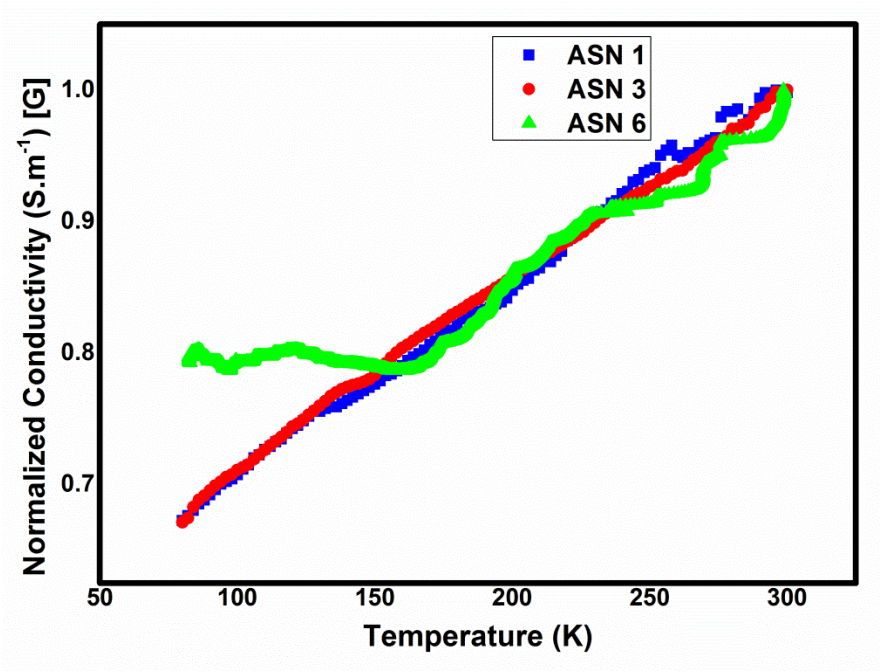

Figure 5.7. Variation of normalized conductance of the composite samples with temperature.

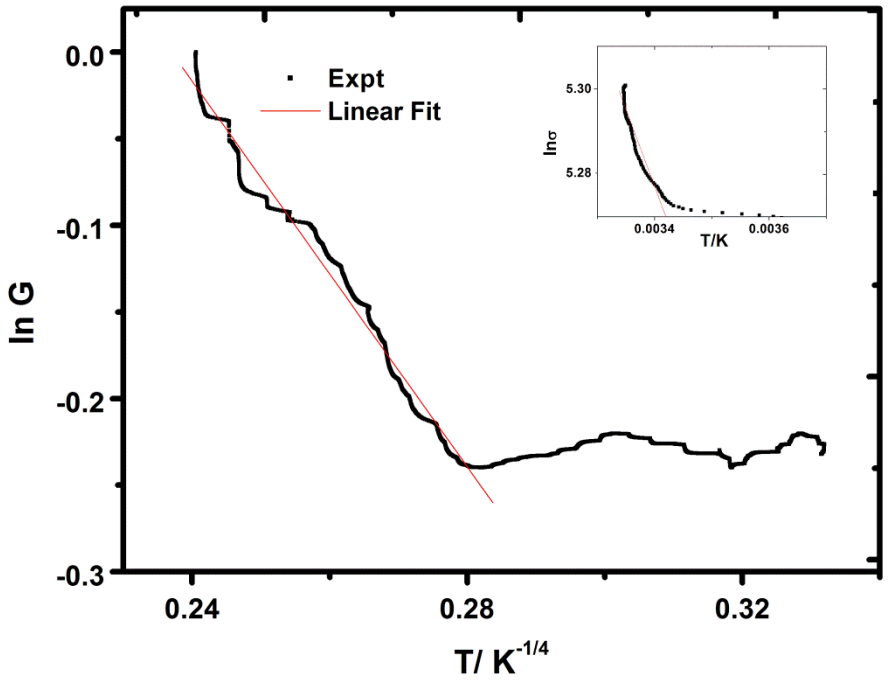

Figure 5.8. Variation of normalized conductance of ASN-6 with temperatures ($T^{-1/4}$) showing 3D variable range hopping characteristics

Further analyses on the compliance of the mechanisms of transport in the ASN-6 composites with the 3D varable range hopping (VRH) the normalized conductivity values (lnG) were plotted with temperature ($T^{-1/4}$) in **Figure 5.8**. It could be observed

that the hopping mechanism is not followed in the entire temperature range studied for ASN-6. The variation **Figure 5.8** could be approximated to an equation of the form suggested earlier [193,194],

$$G = G_0 \exp (T_0/T)^{1/(d+1)} + G_m + G_a \exp (E_a/RT) \quad (27)$$

Which is a modified Mott's equation for fluctuation aided tunnelling, metallic conduction and thermally activated conduction. G_0 is the prefactor for the variable range hopping, d is the dimensionality of conduction (1, 2 or 3), Ga is the prefactor for thermal activation term and T_0 is the hopping parameter.

Figure 5.8 shows that the variation of the conductance of ASN-6 could be divided into three parts. Below 175K the conductivity is almost constant with temperature. This type of behaviour (freezing of hopping characteristics) was observed for thin sheets of annealed SWCNTs in earlier studies where the dominance of metallic conduction has been found to prevail at lower temperature [194]. Thus, the temperature independent conductivity of ASN-6 at low temperature could be explained by the conduction through metallic tubes. The levelling off of the conductivity values of the composite starts from a higher temperature (175K in **Figure 5.8**) than that observed in case of annealed thin films in the earlier study [194]. The reason may be the presence of higher percentage of metallic tubes in the present composite (68% vs. 33%) where the contribution of hopping minimizes at a higher temperature. The junction between the metallic and semiconducting tubes in both the confined and axial direction should, therefore, play a significant role in controlling the conduction of the network at higher temperature. More metallic behaviour and non-linear relationship in the current-voltage plot above 423K were observed earlier in electrical behaviour of Si_3N_4-MWCNT composites when the tube contents were increased to 8.6vol% [109]. Rapid VRH conduction of ASN-6 above 175K is due to the hopping of carriers between metallic and semiconducting tubes. The hopping parameter (T_0) is determined from the slope of the intermediate linear portion of the curve **Figure 5.8** and found to be of the order of 10^3 K lower than that of the annealed SWCNT film (10^5K) [194]. Increase of localization length in the present nanotube ropes due to the high metallic tube content in the sample is, therefore, the reason for lower value of the hopping parameter (T_0). Another deviation from the VRH model at further high temperature showing higher conductivity values than that predicted by VRH model could be observed in the present experiments [**Figure 5.8** (inset)] similar

to those observed earlier [194]. Activation energy calculated for the high temperature data is 0.22eV, typical value obtained for Schottky like barrier between metallic and semiconducting tubes [18]. However, the activation energy for the high temperature portion in **Figure 5.8** inset is 0.039eV which may be considered as very low and may be due to the contribution from the conduction of more metallic tubes in ASN-6 sample or the conduction across small barriers between metal electrodes and metallic tubes [195].

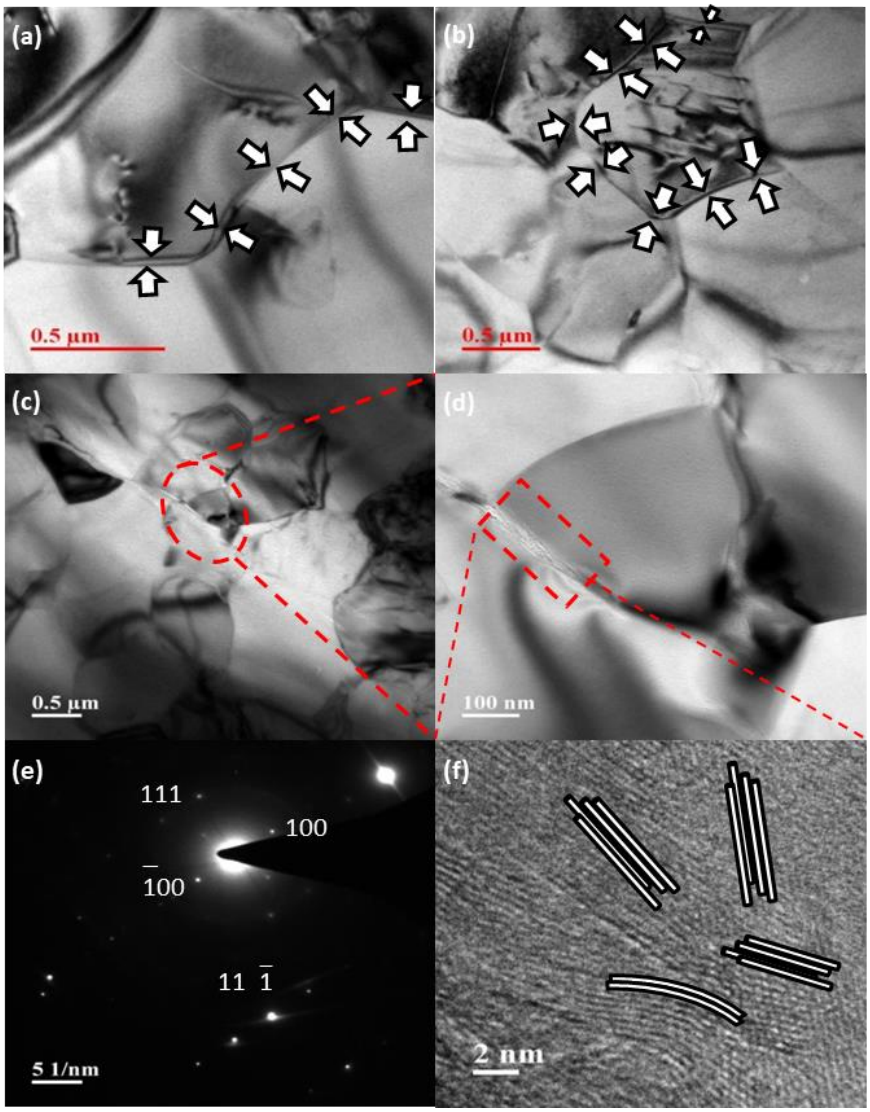

Figure 5.9. TEM images of cross section of ASN-6 cut (a) parallel and (b) perpendicular to the hot pressing direction. White arrows indicate the locations of the tubes at the grain boundaries; (c) SWCNT ropes/mats surrounding an individual grain of the sample shown in (a); (d) magnified image of the grain boundary marked by red circle in (c); (e) SAED pattern of the grain boundary marked by red rectangle in (d); (f) HRTEM of nanotube nets at the grain boundary marked in (d). Schematic diagrams have been inserted to show the orientations and bend contours of nanotubes within the net.

TEM images of thin foils of the composite samples in **Figure 5.9** show that SWCNT ropes are present along the grain boundaries of AlN. 3D connectivity of the ropes could be established from the images taken both in parallel and perpendicular to the hot pressing direction [**Figure 5.9**(a), (b) and (c)]. Higher magnification image and selected area diffraction (SAED) of grain boundary [**Figure 5.9** (d) and (e)] confirm the presence of SWCNT tubes (PDF Card No.00-058-1638). HRTEM of SWCNT nets at grain boundary show the different orientations and bending of the nanotubes in the net.

The results indicate that the high electrical conductivity of AlN-SWCNT composite prepared in the present study is due to the presence of 3D network of large quantity of SWCNT tubes in the grain interfaces of the material. The conduction behaviour is similar to those of thin sheets of SWCNTs usually prepared for transparent conductors. Dependence of dc electrical conductivity with temperature shows that 3D variable range hopping transport (VRH) between metallic and semiconducting tubes is the controlling mechanism of transport when the amount of SWCNT is low (1 and 3vol%). TEM examination of the cross sections of the composite containing 6vol% SWCNT in two directions perpendicular to each other confirms the presence of SWCNT networks in three dimensions. However, the hopping transport freezes showing no dependence with temperatures below 175K when the content of the nanotubes is increased to 6vol%. Low VRH parameter (T_0 - 10^3K) has been ascribed to the higher metallic tube content in the samples. Overall, high content of metallic SWCNTs has improved the electrical conductivities of the ceramic nanocomposite.

5.3.Dielectric Properties of the AlN-SWCNT Nanocomposites

5.3.1. Impedance and Reactance

Ceramic composites containing conducting particulates under AC applied field could be considered as circuits containing Resistor(R), Inductor (L) and Capacitor (C). Capacitor and Inductor act in opposite way to the applied field. **Figure 5.10** shows the frequency dependence of real value of the impedances of the samples.

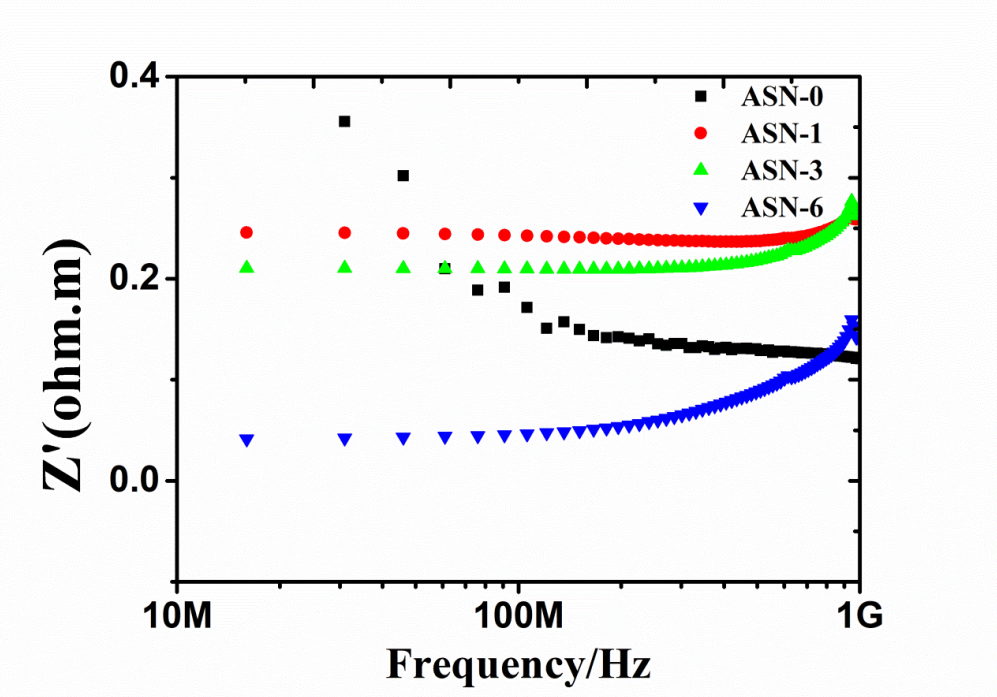

Figure 5.10. Variation of impedance (real) with frequency

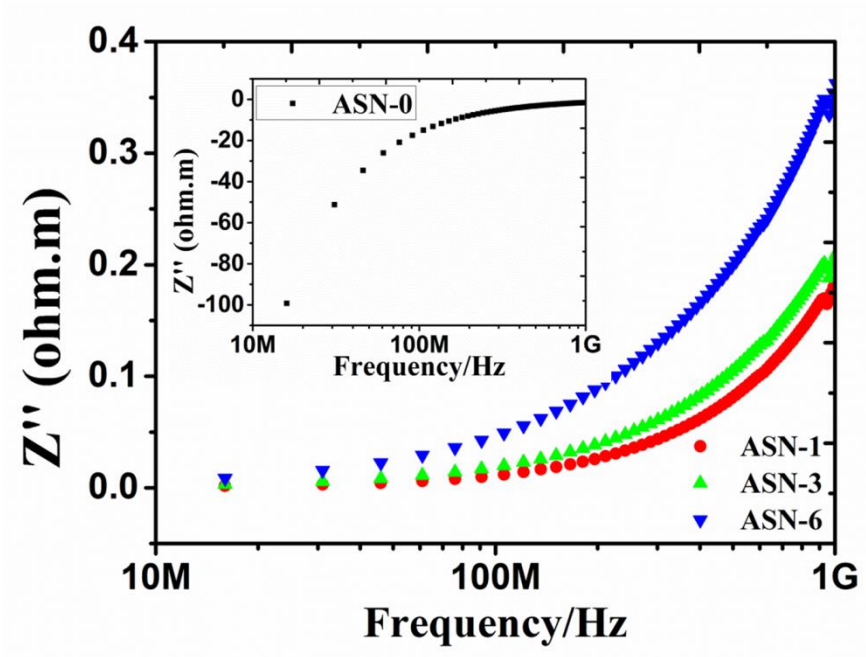

Figure 5.11. Variation of reactance (Z") with frequency

Figure 5.10 shows that the impedance values decreases with the amount of SWCNTs present in the material. This is the result of the increase in inductance in the materials with the increase in the concentration of SWCNTs in the composites. Addition of more SWCNTs in the material causes more network formation and the creation of

current loops under high frequencies of the AC-field, thus, reducing the impedance values.

Figure 5.11 shows the variation of total reactance (Z´´) of the composites with the frequencies. Reactance of the composites are shown in **Figure 5.11.** The total reactance could be expressed as

$$Z'' = X_L - X_C \quad (28)$$

inductive ($X_L = \omega L$) and capacitive ($X_C = 1/\omega C$) reactances [196]. Inductive reactance (X_L) becomes more than the capacitive reactance (X_C) when the concentration of SWCNT increases in the composite. The highest LC reactance value could be observed for ASN-6 **Figure 5.11** The best fit of $|Z|$ vs frequency shows that the equivalent circuit consists of resistors (R_1 and R_2), capacitor (C), and inductors (L_1 and L_2). This type of fitting had earlier been observed to work well for the composites containing percolating networks[137]. Positive Z´´ values could be observed in **Figure 5.11** similar to those in metacomposites containing percolating networks of Carbon in porous Si_3N_4 and CNTs in Al_2O_3 composites [137,197]. Almost invariant positive reactance (Z´´) values with frequencies had been observed in percolating AlN-Graphene platelet composites [138] and increasing values with the frequency with a resonance near 1GHz were observed for percolating networks of amorphous carbon dispersed porous Si_3N_4 architecture [197]. Inductive elements (L_1, L_2) are required to explain this type of positive behavior. R-L-C current loops are formed within the composites and positive values are observed within the test frequency range. A possible resonance and switching from inductive to capacitive behavior could also be noticed at higher frequencies near 1GHz in samples is another important observation in those studies [197].

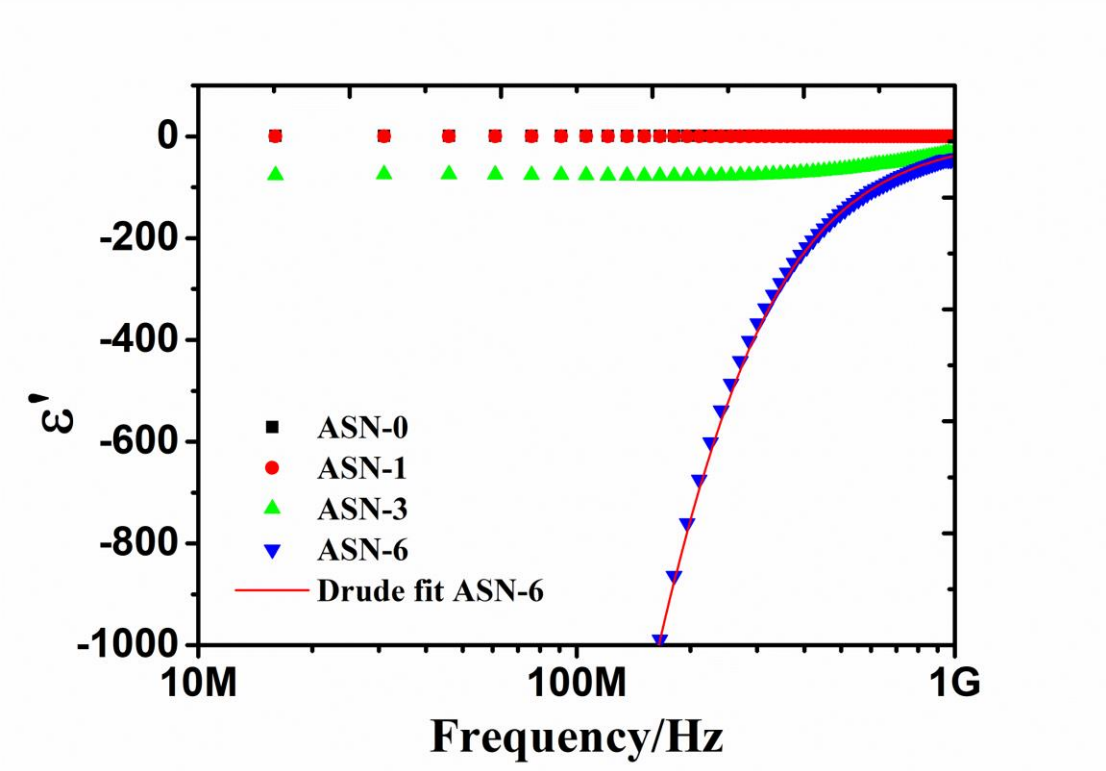

Figure 5.12. Variation of permittivity (real)(ε') with frequency vs ε'.

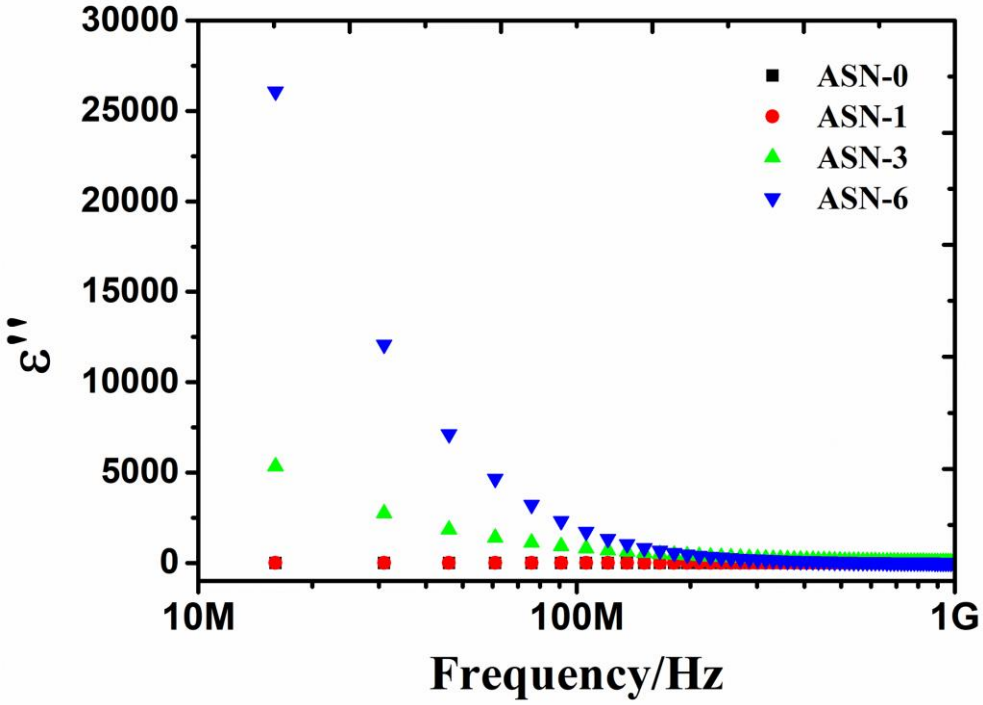

Figure 5.13. Variation of imaginary component of permittivity (ε") with frequency.

5.3.2. Permittivity and Loss

Complex permittivity could be expressed as

$$\varepsilon^* = \varepsilon' - i\varepsilon'' \quad (29)$$

Where ε′ and ε″ are the real and imaginary part of the permittivity respectively and calculated from the following relation [198].

$$\varepsilon' = (1/\omega C_0)[-Z''/(Z'^2+Z''^2)] \quad (30)$$

and

$$\varepsilon'' = (1/\omega C_0)[Z'/(Z'^2+Z''^2)] \quad (31)$$

Dielectric properties of the composite samples are presented in **Figure 5.12** which shows that the real values of permittivities (ε′) are negatives for all the composite samples within the tested frequency range. The values become more negative when more SWCNTs are present in the composite. The prime reason for the negative permittivity is the incorporation of SWCNTs in the ceramics. Interconnectivity of the ropes and building up of nanotube mats surrounding the grains (SEM and TEM micrographs, **Figure 6.5 Figure 5.14**) has ensured a high electrical conductivity and plasma like negative permittivity in the whole frequency range observed in all the composite samples. The electrical conductivities presented in **Figure 5.1** shows that all the samples tested in the present study contained percolating CNTs. Dispersion of the permittivities is usually explained with the Drude model as follows [197],

$$\varepsilon_r' = 1 - \omega_p{}^2/(\omega^2 + \omega_\tau{}^2) \quad (32)$$

Where 'ω' is the experimental applied angular frequency (2πf, where 'f' is the linear frequency), and 'ω_τ' is the damping parameter.

$$\omega_P = n_{eff}e^2/m_{eff}\varepsilon_0 \quad (33)$$

Where, n_{eff} = effective electron density,

m_{eff} = effective electron mass

e = electronic charge = 1.6 x 10^{-19} C

ε_0 = permittivity of vacuum = 8.85 x 10^{-12} F/m.

The plasma frequency value (ω_p) of ASN-6 calculated from Drude's law [Eqn (30)] has been found to be 6.2 x 10^9 s^{-1} while that of SWCNT mat was found to be 3.3 x

10^{13} s^{-1} [24]. Good fit of Eqn. (32) could be visible from the red line in **Figure 5.12**. The reason behind the lower ω_p in ceramic composite (ASN-6) could be assessed from the above relation Eqn. 32 Principally, a volume fraction of the composite material consists of SWCNT mat, thus, causing dilution of electron concentration in the material and reducing the value of 'n_{eff}'. Moreover, confinement of the SWCNT mats within grain boundaries should have caused the restriction in the movement of electrons and increasing the the effective mass 'm_{eff}'. Equation (32) and (33) also indicate that negative value of 'ε_r'' will increase with 'ω_p' which is directly related to the number of free electrons (n_{eff}) in the materials. In the present case the concentration of SWCNTs provides the number of free electrons and its increase is therefore, the reason for highest negative permittivity observed by ASN-6 sample. The values of (ε'') are positive and decreases with frequencies similar to those of AlN/Graphene platelet composites prepared by SPS [138]. Losses at difference frequency regimes (ε'') follow the relation [137],

$$\varepsilon'' = \varepsilon''C + \varepsilon''D + \varepsilon''P \qquad (34)$$

ε''_C is the ohmic conduction loss, ε''_D is the dipolar loss and ε''_p is the interfacial polarization loss. Interfacial polarization loss (ε''_P) is insignificant at frequencies higher than 1MHz since charges cannot build up at the interface as fast as the change in the alternative field. Therefore, conduction loss (ε''_C) and dipolar loss (ε''_D) are the main contributors to the overall dielectric loss. The conduction loss could be expressed as,

$$\varepsilon''C = \sigma_{dc}/2\pi f\varepsilon_0 \qquad (35)$$

where 'σ_{dc}' is the dc-electrical conductivity of the material , 'f' is the frequency of the ac-field. Thus, 'ε''_C' is proportional to 1/ f since all other parameters on the right hand side of the equation (35) is constant at a particular temperature.

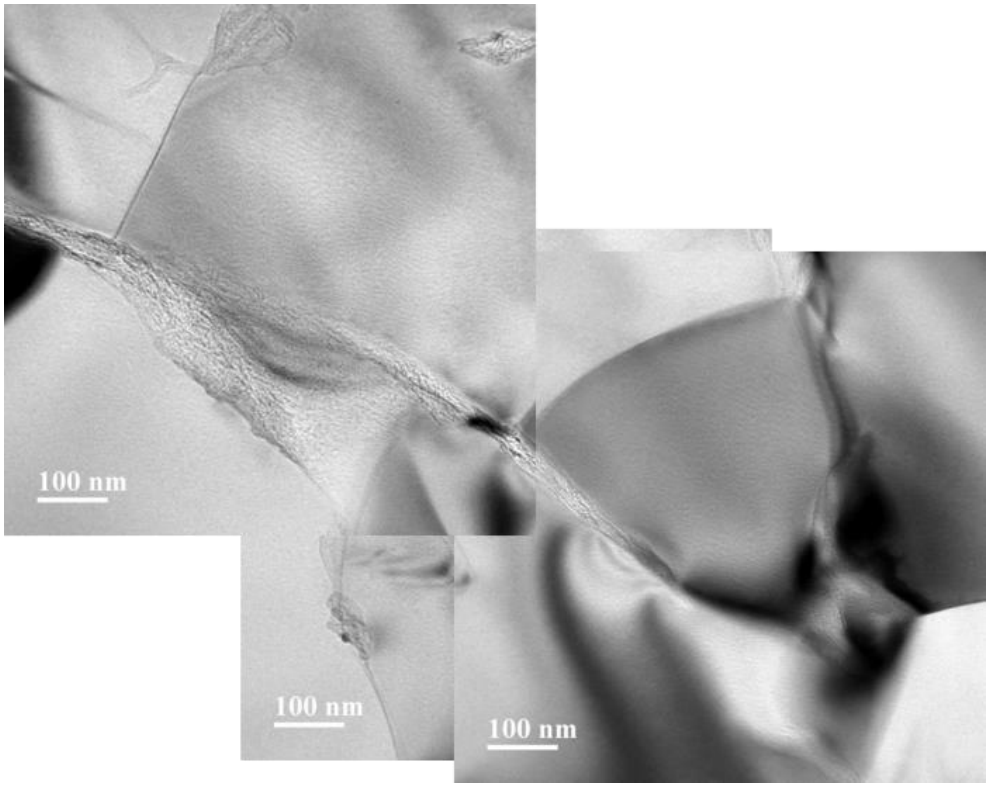

Figure 5.14. TEM image of interconnectivities of SWCNT ropes surrounding AlN grains (Montage).

The reason behind the stability of the structure of the tubes is primarily the chemical compatibility of CNTs with AlN under carbonaceous hot pressing atmosphere at the temperature of processing. AlN has been found to be chemically stable with Carbon even at high temperature (1600°C) under overpressure (0.4MPa) of nitrogen gas[199]. Rate of heating is also another factor which is fast enough to reduce the grain coarsening Moreover, increased densification rate by external pressure during hot pressing helped minimizing the exposure time of the CNTs with the external nitrogen atmosphere, a probable reactive species for the destruction of the structure of the tubes, if any, at high temperature by the formation of cyanogen or carbon nitrides [200]. Addition of sintering agent (3.8wt% Y_2O_3) in the present study helped the formation of liquid phase at high temperature which accelerated the sintering rate further by particle rearrangement and enhanced diffusion. Lastly, the pre-sintering processing of the constituent powders like homogenizing and mixing of sols and the method of ultrasonication and drying adopted in the present study had helped to disperse the CNTs to a great extent within the matrix and accelerate the densification resulting in the minimization of their exposure to nitrogen gas.

Chapter 6

Mechanical properties of AlN-SWCNT composite

A detailed literature review on mechanical properties of ceramic CNT composites is presented in Chapter 2. The role of CNTs on the mechanical properties of ceramic nanocomposites remains indecisive. This is because of the usage of different types and compositions of CNTs, inhomogeneous distribution of CNTs and differences in experimental conditions. Present work gives a detailed analysis of mechanical properties of AlN-SWCNT composite. Presence of SWCNT in AlN matrix is confirmed in chapter 4 by SEM, TEM, Raman characterization techniques. The mechanical properties of nanocomposite SWCNT reinforced in AlN. The outcomes of these comparisons are discussed in relation with their microstructures.

6.1. Vickers Hardness

Figure 6.1 shows the SEM micrograph of an hardness indent made by 1000gm load on the surface of ASN-6 sample. Cracks and damages associated with the indentation could be observed from **Figure 6.1**.

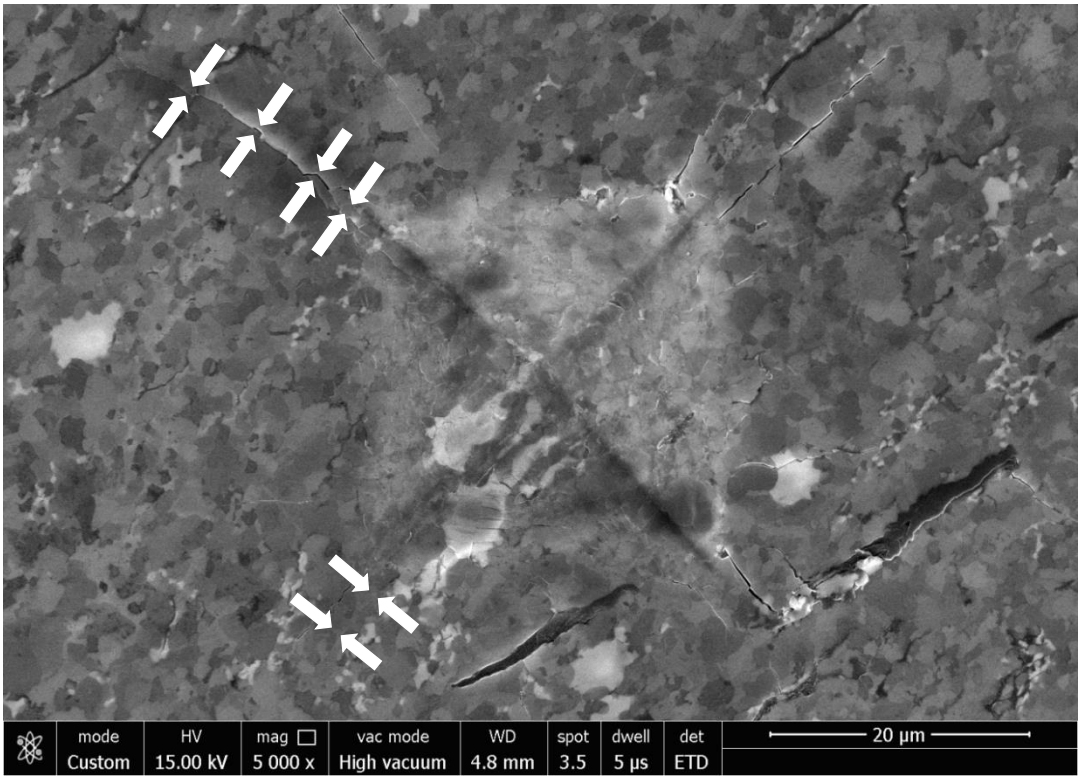

Figure 6.1. SEM micrograph of a Vickers indent made with 1000gm load on the surface of ASN-6 alongwith associated radial cracks marked by the arrows.

The hardness values of all the samples estimated through Vickers indentation method are shown in Figure 6.3. A modest increase in the hardness (≈15%) could be observed for samples containing 1 vol% SWCNT (ASN-1). However, a mild decrease in hardness was observed at higher concentrations of SWCNT in the composite (ASN-3 and ASN-6). Each hardness value presented in **Figure 6.3** is the average of 6 measurements at 1000 gm load. A similar trend had been noticed earlier in ZrO_2-MWCNT composites [201]. Zhan and Mukherjee [17] observed no change in the hardness of Al_2O_3-SWCNT composite with the addition of 5 and 7 vol% SWCNTs. However, the hardness decreased by 20% when the SWCNT content was increased to 10 vol %. Vicker's hardness of ceramic-SWCNT composite had been found to be lower [35,202–205] than that of the matrix material and the reason cited is the presence of softer SWCNT material in the grain boundaries acting like graphite lubricant [203]. However, it could be observed from **Figure 4.9** in Chapter 4 and the results from earlier investigations [206] that SWCNT forms entangled ropes in grain boundaries restricting the sliding of grains. Careful investigation on the microstructures **(Figure 4.9)** could suggest that the increase in SWCNT content shows increased SWCNT content around the grains which should increase the

plasticity of the material primarily due to higher strains in the confinement direction of the 1D SWCNT tubes present in the grain boundaries. Quantitative strains on radial compression of SWCNTs have been measured by several authors [207,208] and it has been observed that CNTs can accommodate considerable strain (0.40) in radial direction exhibiting high deformability [209]. Vicker's indentation compresses several grains and their boundaries consisting of SWCNT matts multiaxially (**Figure 6.2**).

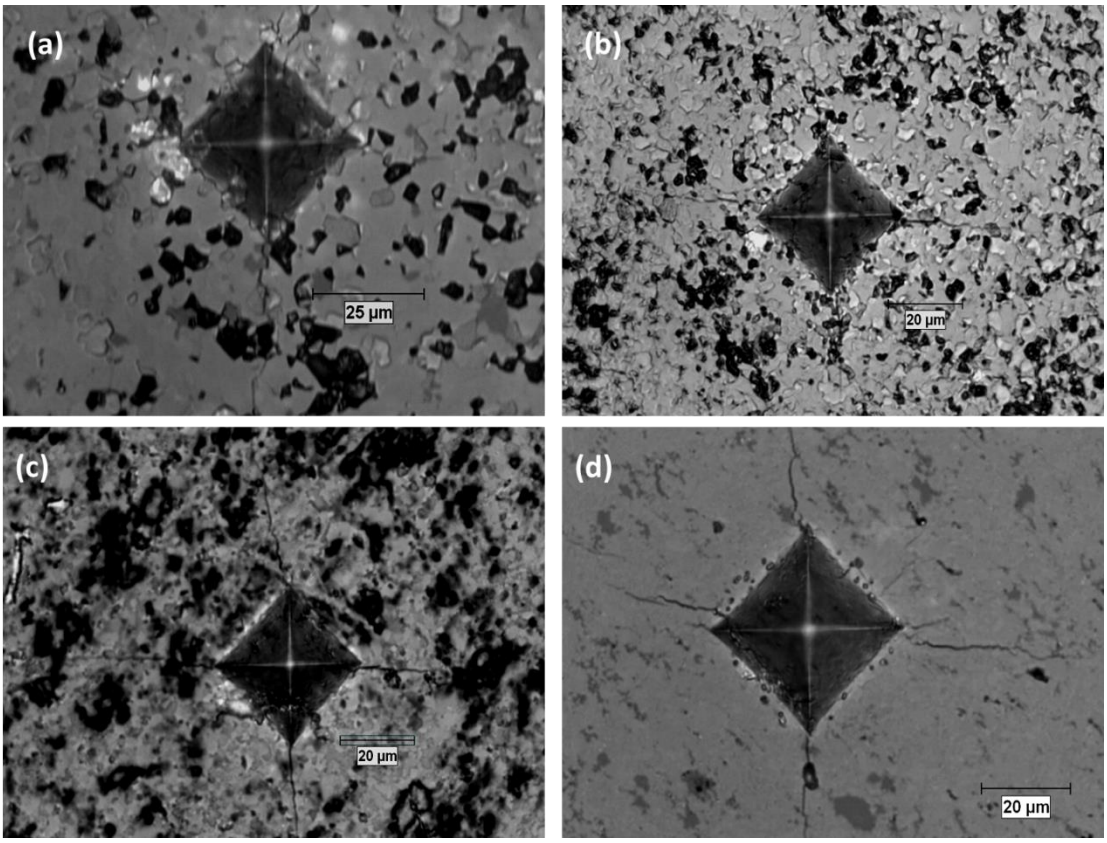

Figure 6.2. Optical micrographs of Vicker's indents showing clear indent formation and crack growth from the corners of the indents in (a) ASN-0, (b) ASN-1, (c) ASN-3 and (d) ASN-6.

The effect of the radial deformation of the tubes is not substantial in samples containing low amount of SWCNT such as 1 vol% in the ASN-1 sample in the present study. Presence of large volume percentage of SWCNTs in the grain boundaries, however, leads to higher deformation in the plastic zone surrounding the indenter and consequently decreases the hardness of the composite. However, grain sizes are reduced to a great extent **(Figure 4.10, Chapter 4 and Figure 4.9)** by the increase in the SWCNT content in the nanocomposite which should have increased the hardness in accordance with the Hall-Petch relation [210,211]. Grain size decrease has been observed in SiC-CNT composite prepared by liquid phase sintering method

implying decrease of solution reprecipitation rate during the sintering [35]. Compressive deformation of the tubes nullifies the effect of grain size reduction on hardness increase in AlN composite samples containing more than 1vol% SWCNT. As an extreme case, shear collapse of the tube forming shear bands and accommodating high deformation energies during indentation as suggested in an earlier publication [212] cannot be ruled out. The phenomena could be explained with a model presented in **Figure 6.4.**

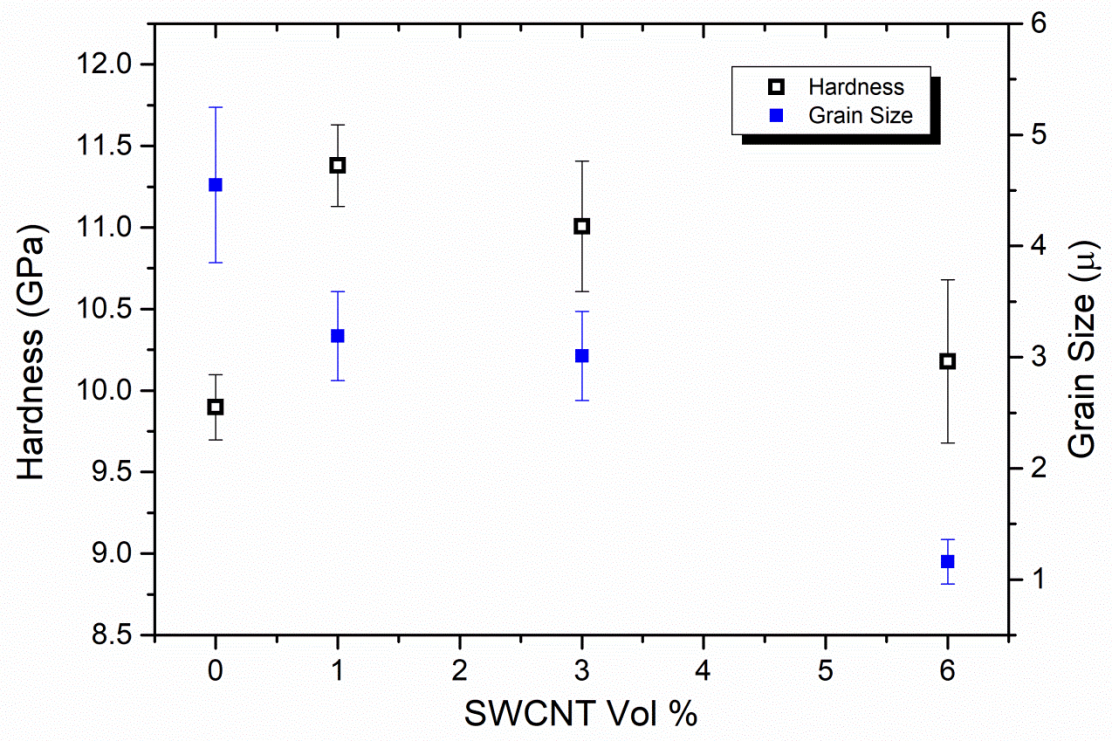

Figure 6.3. Variation of hardness and grain size with the SWCNT content.

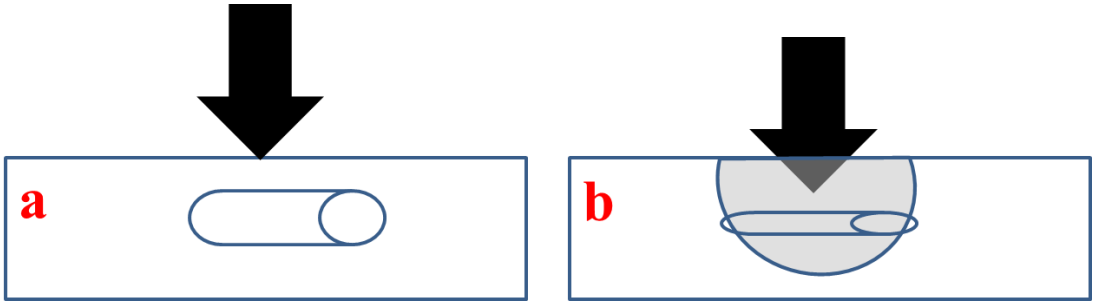

Figure 6.4. Compressive load transfer to the SWCNT and corresponding deformation along its radius. (a) Onset of Indentation load and (b) Applied load and its effect on the composite microstructure.

6.2.Fracture toughness

Fracture toughness is the significant characteristic of any structural material which indicates the resistance of the material to crack formation and propagation. Cho et al. [110] have shown that K_{IC} increases with the SWCNT content in glass ceramics system and measurement by indentation fracture method produced almost the same trend with the CNT content as those measured by Chevron notch method. However, the values obtained by indentation fracture method are overestimated by a factor of two and hence absolute value could not be produced by the indentation fracture method. Hence the fracture toughness values presented in **Table 6.1** can be taken for comparison and not for determination of the absolute values. Toughening mechanism of ceramic-CNT composites are explained from the similarity with that of fiber reinforced composite systems. CNT pull-out similar to the fiber pull-out in the macro system had been observed to be the dominant toughening mechanism for glass-ceramics- CNT composites alongwith other toughening mechanisms such as crack bridging and crack deflection [110]. FESEM micrographs of fracture surfaces **[Figure 6.5]** show transgranular fracture of the composites alongwith substantial load bearing capacities of the SWCNTs from the approximate large pull-out length of the tubes (max length >2μm). SWCNT pull-out should, therefore, be a contributing factor in toughening of the composites [177,213].

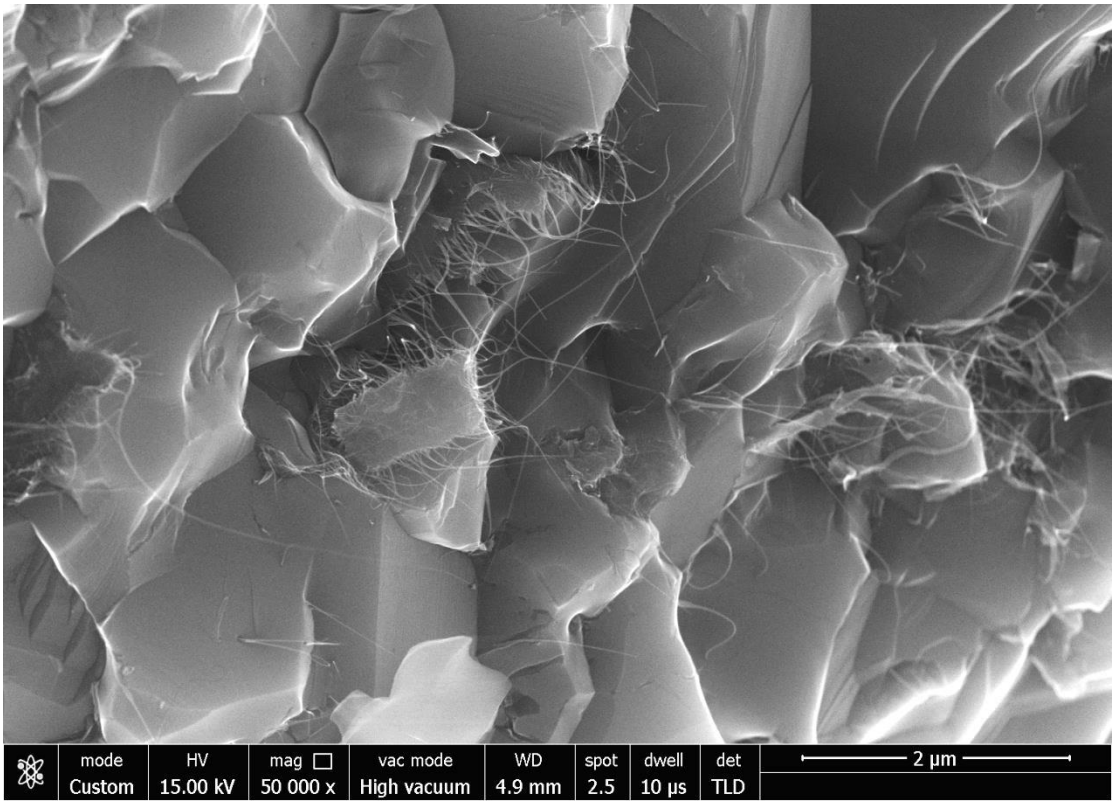

Figure 6.5. FESEM micrograph of fracture surface of ASN-6 showing very long SWCNT rope interwoven along several grain boundaries.

has been shown to be crack bridging was observed by FESEM of composites which shows the resistance to crack propagation. From the earlier studies on fracture toughness of ceramic-CNT composites

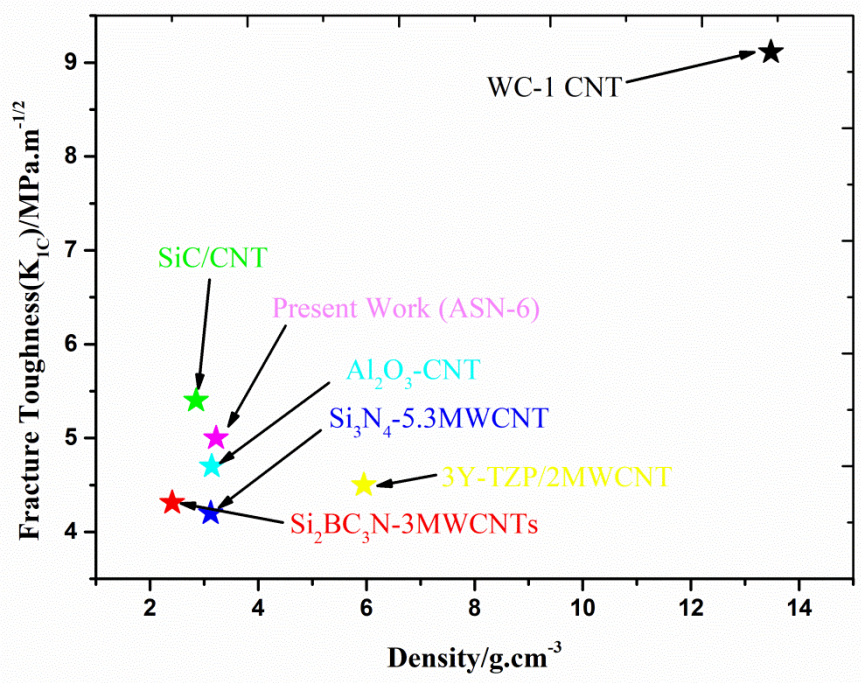

Figure 6.6. Density vs Fracture toughness of different ceramic CNT composite [84,93,100–102,185,214].

Table 6.1. Fracture toughness of samples.

Sr. No.	Sample	Fracture Toughness (MPa· $m^{1/2}$)
1.	ASN-0	2.9
2.	ASN-1	3.5
3.	ASN-3	3.98
4.	ASN-6	5

A detailed literature review on fracture toughness on ceramic CNT composites were discussed earlier in chapter 2. **Figure 6.7** shows also long pull out of the tubes indicating high load bearing capacity during the fracture. 60% fracture toughness increase from 2.9 MPa.$m^{1/2}$ in ASN-0 to 5 MPa.$m^{1/2}$ in ASN-6 is due to crack-bridging, pullout, debundling & uncoiling of SWCNT.

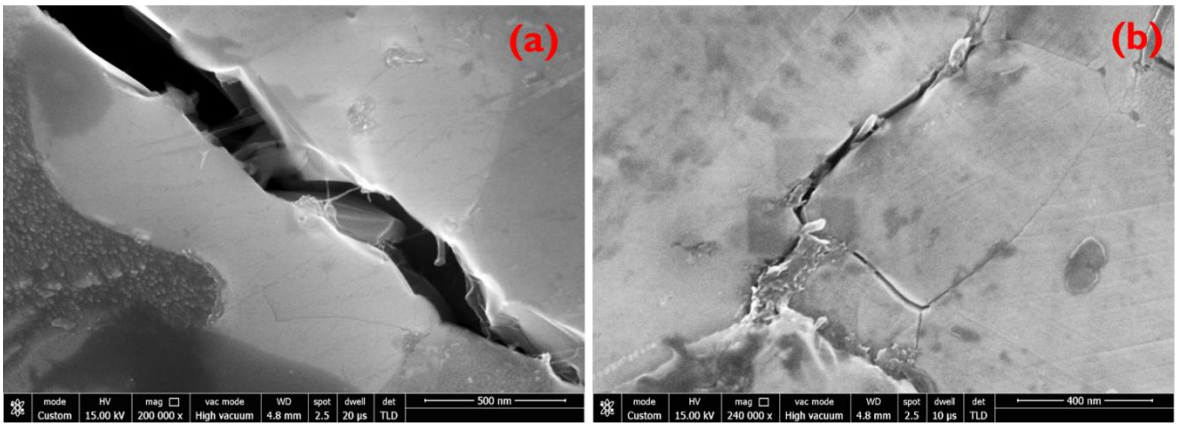

Figure 6.7. (a) Crack-bridging and (b) Uncoiling of SWCNT ropes in ASN-6 sample.

6.3.Raman micro stress mapping

Some authors have also mentions on the residual stress toughening of the composites due to the thermal expansion mismatch between ceramics like Al_2O_3 and CNT [81]. Moreover, there is also a difference in thermal expansion coefficients between the axial and radial directions of the tubes and inter tube gaps creating high residual stress in Al_2O_3. We have carried out a stress analysis with the help of Raman microprobe and present the results below;

He-Ne laser operating at a wavelength of 530 nm (with a power of 25 mW) was used as the excitation source in confocal Raman optical microscope. The recorded spectra were examined by fitting with a Gauss –Lorentz mixed-function using origin software. Wavenumber shifts were obtained from the difference between the peak center under stress and that as monitored in a reference stress-free body [215]. A variety of internal microscopic stress fields existing in AlN-SWCNT composites have been calculated using Raman spectroscopy technique. Shifts of AlN Raman Peak ($656cm^{-1}$) in ASN-0, 1 & 6 could be observed in **Figure 6.8** and is the result of residual stresses in the samples arising out of processing conditions and differences in the co-efficients of thermal expansions. Effect of micro indent as well as the incorporation of SWCNTs in the creation of local stress zones have been assessed in ASN-6 composite and shown in **Figure 6.9**. Effect of micro indent as well as incorporation of SWCNT in AlN ceramic observed. However, stresses were recorded both at zero and critical (external) load for crack propagation and, from the shift of the Raman peak between the latter and the former loading condition, a ‘bridging stress’ field was calculated.

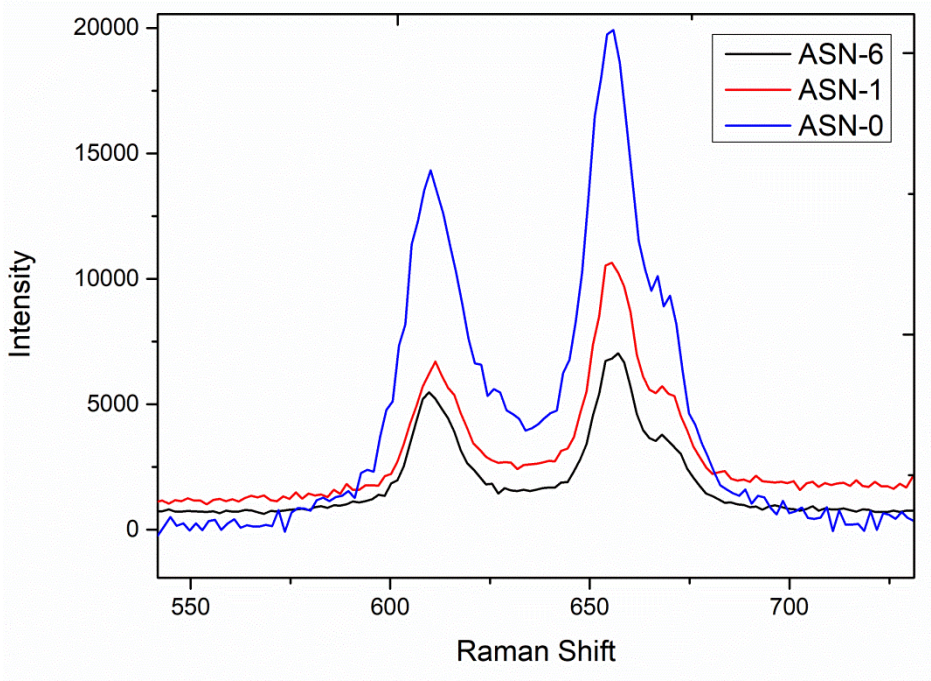

Figure 6.8. Raman spectra of for residual stress.

Based on the piezo-spectroscopic effect [215,216], Raman peaks shifts upon stress, were engaged for the characterization of microscopic stresses in the composite. Applied or Residual Stresses change the vibrational and electronic levels of the materials. The piezo-spectroscopic relation can be generally expressed by the following tensorial equation

$$\sigma_{ii} = {}^{\Delta\nu}/_{3\pi} \qquad (36)$$

Where σ_{ii} – Residual Stress, $\Delta\nu$ - Raman Peak shift, and π - Uniaxial Piezo-spectroscopic Coefficient

Changes in stress levels have been mapped on an indentation area. Localized pockets of stressed zones (pink, green and red areas) due to the presence of agglomerated SWCNTs could be noticed in **Figure 6.9**. Cracks should have been deflected from these sites increasing the fracture toughness of the composites.

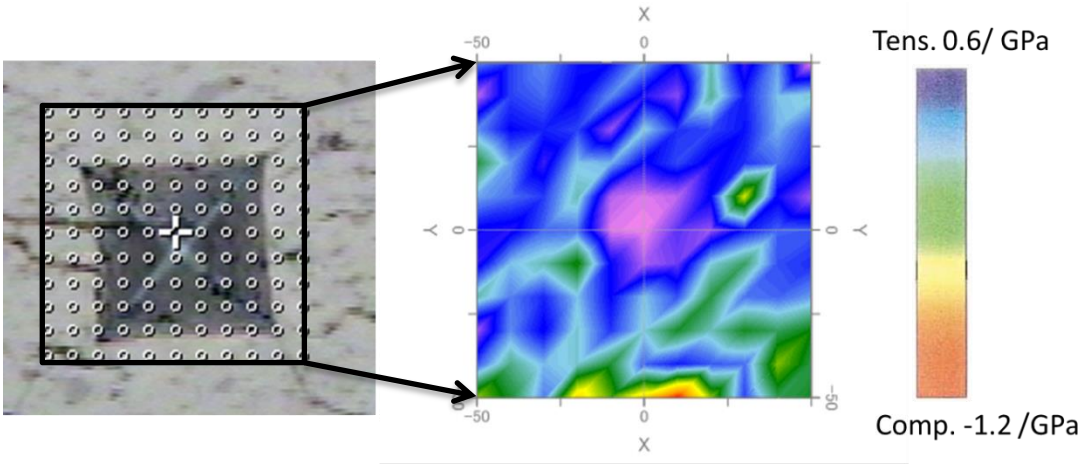

Figure 6.9. Mapping Raman Spectral shift on ASN-6 sample.

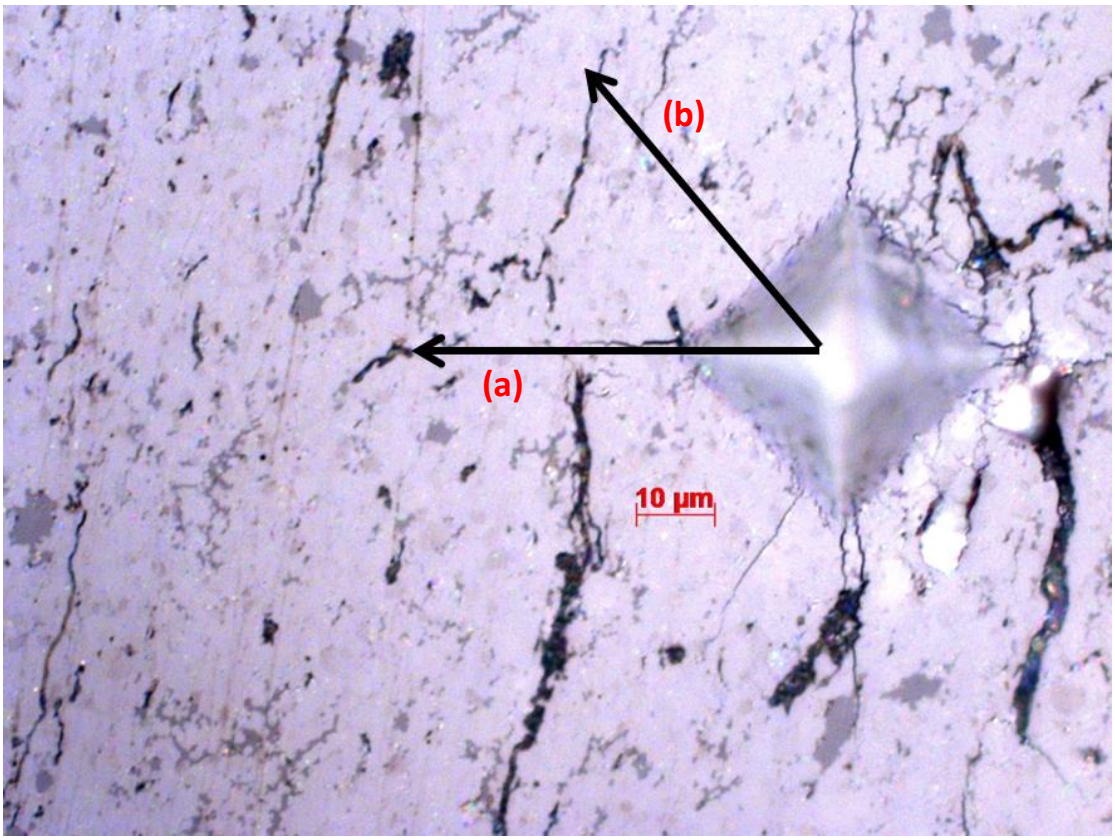

Figure 6.10. Raman spectra on the side and diagonal direction.

Raman probe shifted from the center of the indent **Figure 6.10** (a) parallel to diagonal and (b) perpendicular to the edge of the indent made by 9.8N load

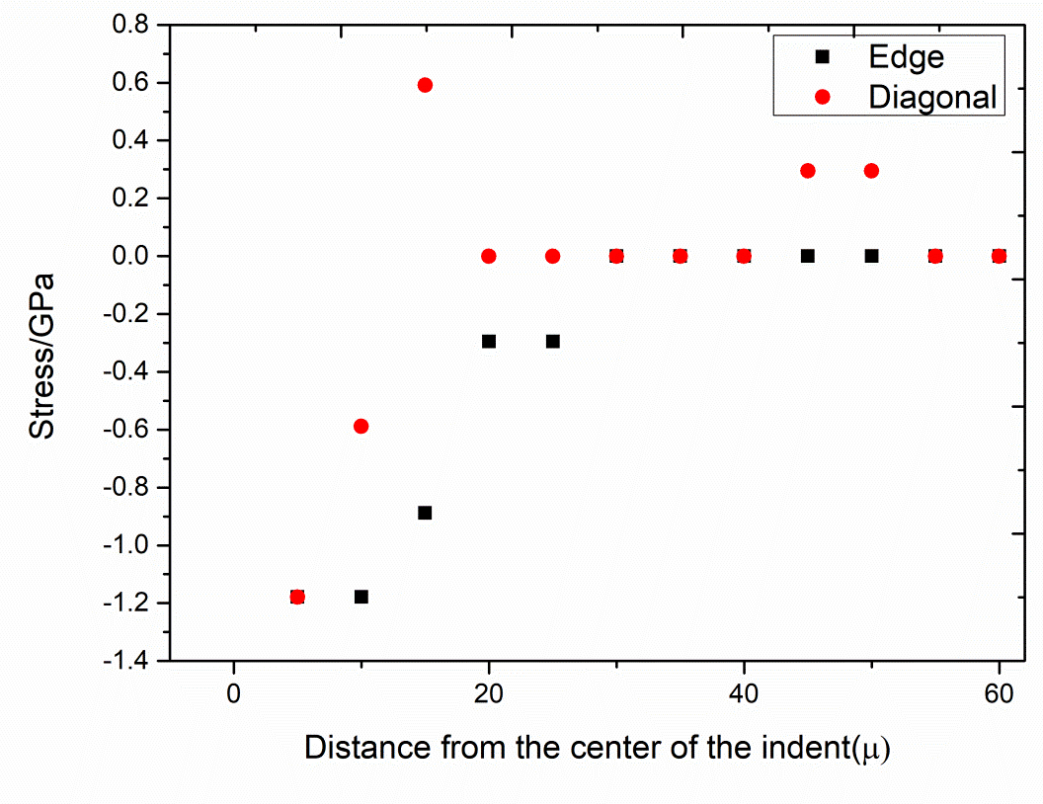

Figure 6.11. Variation of stress after indentation.

Figure 6.11 shows the variation of stress from the center of the indent. It can be observed that stress becomes compressive towards the edge of the indent. Stress relaxation occurs over a shorter distance along the direction of the diagonal because of stress relief at the corners of the diagonal by creation of crack.

Thus, the study has ensured a considerable compressive stress in the matrix and presence of pockets of tensile stresses in the areas of SWCNT agglomerates. Further studies are, therefore, needed to quantify the stresses and its contribution to the toughening of the composites.

Chapter 7

Thermal properties of AlN-SWCNT composite

7.1.Thermal Conductivity

The thermal conductivity (κ) at room temperature were calculated for each sample using the equation [217]

$$\kappa = \alpha C_P \rho \quad (37)$$

Where α = thermal diffusivity, Cp = specific heat capacity, and ρ = density.

A graphical representation of the thermal conductivity values of the samples at room temperature is shown in **Figure 7.1**. **Table 7.1** shows the values of thermal conductivities of the samples. These thermal conductivity values were determined simultaneously with the diffusivities and specific heats in the Flashline 4010 apparatus. The specific heat of the materials were determined from the comparison of specific heats with a standard graphite sample and the internal software of the instrument. The thermal conductivity of ASN-0 sample at rt is much lower than normally found earlier in case of liquid phase sintered sample of the same AlN powder with the same amount of Y_2O_3 in CGCRI (127 W/m-K) mainly due to the presence of pores in the hot pressed sample. Pores in ASN-0 samples were shown in FESEM micrograph **Figure 4.9**. A high thermal resistance at grain-pore interface contributes to the decrease in thermal diffusivity of hot pressed AlN without SWCNT addition (ASN-0). However, the values are highest among all the samples in the present study. Thermal conductivity of the nanocomposites at room temperature decreases drastically (27% in ASN-1) with the increasing content of SWCNTs inspite of the densification of the samples **Table 7.1**. Addition of SWCNT reduces the thermal conductivity values further. Increase of thermal resistance comes from the large interfaces of the SWCNTs present in the samples similar to earlier results inspite of more densification on addition of SWCNTs [17,144,154,218]. Thermal resistances from the tube bundles and inter-tube scattering of phonons are the additional factors for the decrease of thermal difusivities of the composites with SWCNT. TEM image in **Figure 5.9** shows bends and twists in the nanotubes within bundles along the AlN grain boundaries. These bends and twists have their roles in the scattering of phonons as observed by earlier studies [17,154,218]. Weak atomic bonding present in the

interfaces had been found to be the reason for the high thermal resistances prevalent in composites [219]. Moreover, the grain size reduction with the amount of SWCNT added to the composite increases the total grain boundary areas which are the source of increasing Kapitza thermal resistances in any polycrystalline materials. Temperature dependences of the thermal diffusivities are presented in **Figure 7.2**. It could be observed that the differences of diffusivities with temperature is maximum in ASN-0 samples and it decreases with the increase in SWCNT contents in the composite showing a minimum in ASN-6. This type of minimum difference in thermal conductivity values have earlier been detected in samples of Al_2O_3 –SWCNT composites containing high amount of SWCNTs (15 vol%) [17]. Almost a horizontal variation of the thermal diffusivity values could be observed in ASN-6 (**Figure 7.2**). The reason for the decrease in thermal conductivity values is the scattering of phonons by phonon-phonon collision (Umklapp scattering) with the rise in temperature. Minimum difference in thermal diffusivity values in ASN-6 is a result of higher contribution from phonon transport in SWCNT mats present in the grain boundaries signifying a possibility of a saturation or minimum value for a composite architecture.

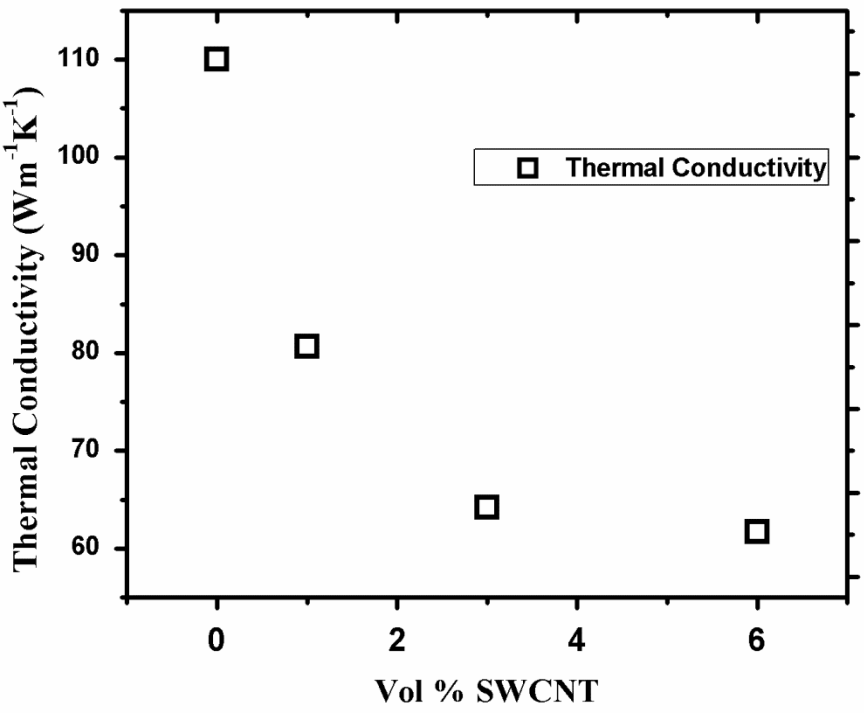

Figure 7.1. Thermal conductivity of samples.

Table 7.1. Thermal conductivity.

Sr. No.	Sample	Thermal Conductivity ($W.m^{-1}K^{-1}$)	Bulk Density (gm/c^3)
1.	ASN-0	110	3.27
2.	ASN-1	80.63	3.28
3.	ASN-3	64.22	3.26
4.	ASN-6	61.69	3.22

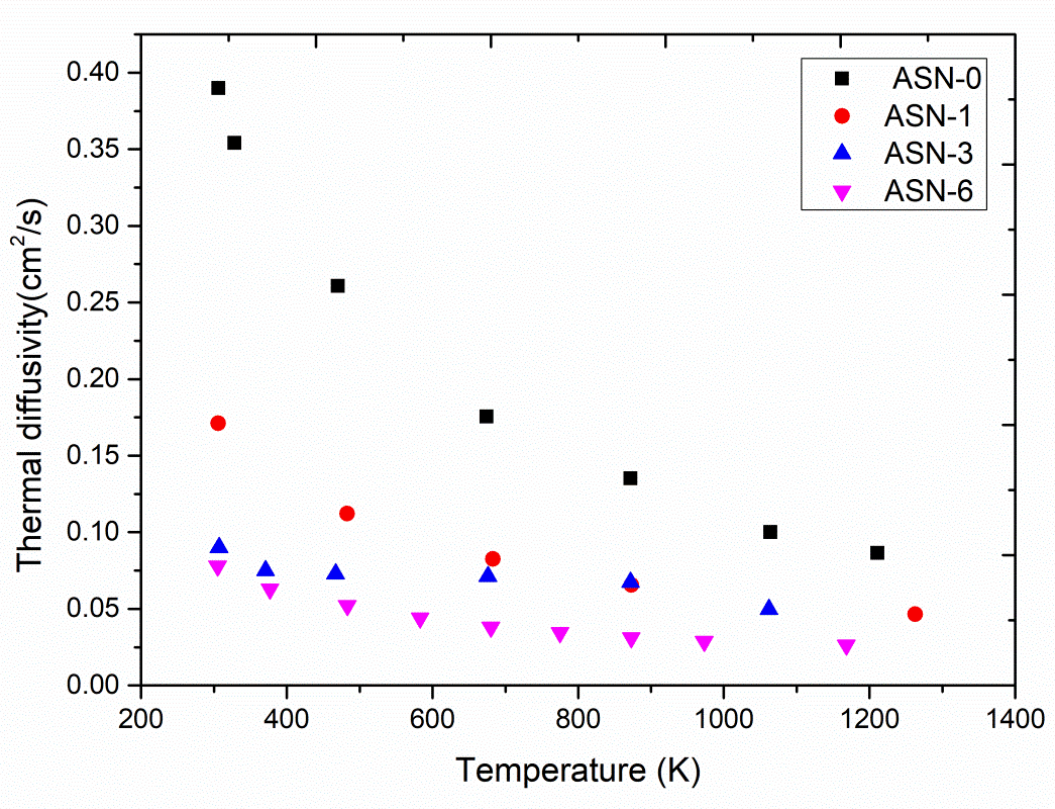

Figure 7.2. Temperature dependence of thermal diffusivities of AlN-SWCNT composite.

7.2. Thermoelectric properties

Our interest to look at the thermoelectric effect of AlN-SWCNT nanocomposite originated from the earlier studies on thermoelectric power of CNT and its composites [70,79,121,220]. It had been observed earlier that polycrystalline AlN sample had a Seebeck co-efficient value of 142 µV/K at 100^0C which increases to 165 µV/K in a composite with SiC (50 mol%) [220]. Moreover, **Figure 7.2** shows that substantial reduction in thermal diffusivity is possible when 6 vol% SWCNT could be

incorporated in the composite. We analysed the Seebeck Coefficient and electrical conductivity values of the composites from rt to 878K and present the report below.

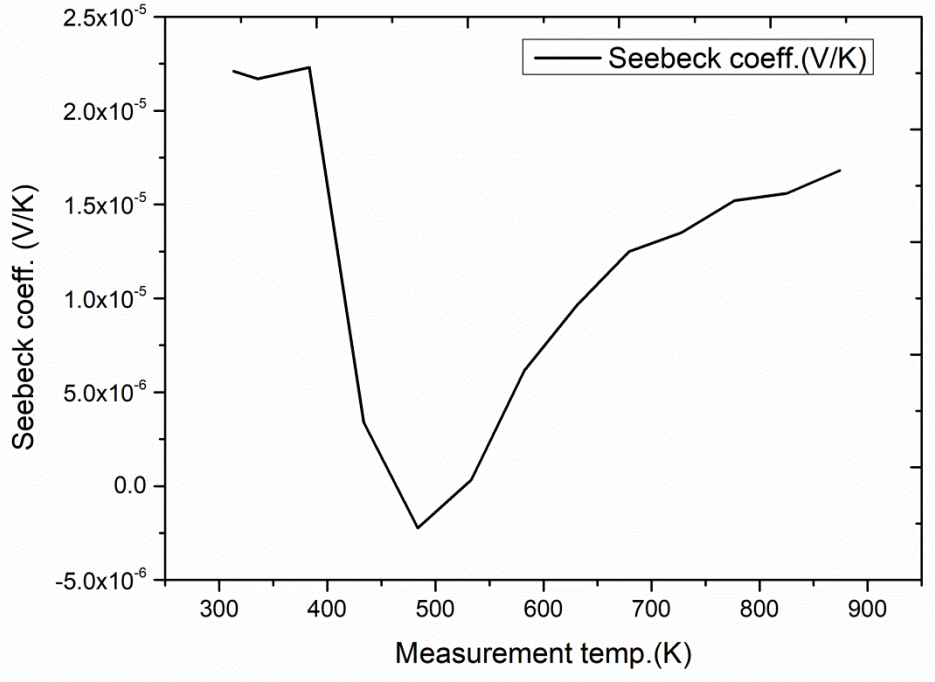

Figure 7.3. Seebeck coefficient of ASN-6 at variable temperature.

Figure 7.3 shows the variation of thermoelectric power with temperature. It could be observed that initially the composite behaves like *p*-type semiconductor at rt with a flattened portion initially with the rise of temperature and then a decrease upto a temperature of 480^{o}C. The Seebeck co-efficient increases with further rise of temperature and reaches 17 µV/K at 838K. Seebeck coefficient value at rt is about 22 µV/K. Comparing with earlier results for metallic SWCNT [140] it could be ascertained that the low thermopower value is related to the high thermal conductivity of the material (62W/m-K) even though the enrichment with metallic nanotubes in the present composite and slight increase of electrical conductivity above room temperature (**Figure 7.4**). Since the thermal diffusivity does not diminish much with the rise of temperature **Figure 7.2** the values of Seebeck co-efficient did not increase with temperature. **Figure 7.3** shows positive thermopower values at rt indicating *p*-type charge carriers prevalent in the material. The decrease of seebeck co-efficient value with the temperature indicating the dominant effect of free electrons in the material (**Figure 7.3**). Similar type of behaviour had been noticed earlier in Ti_4AlN_3 and Ti [221]. Switching to hole dependency again with the further rise of temperature above 480^{o}C is interesting and needs further exploration in future. Erratic increase of

electrical conductivity with temperature could be explained with mixed nature of the nanotubes, junction resistances and bend and twist present with-in the SWCNT network **Figure 5.9**(f).

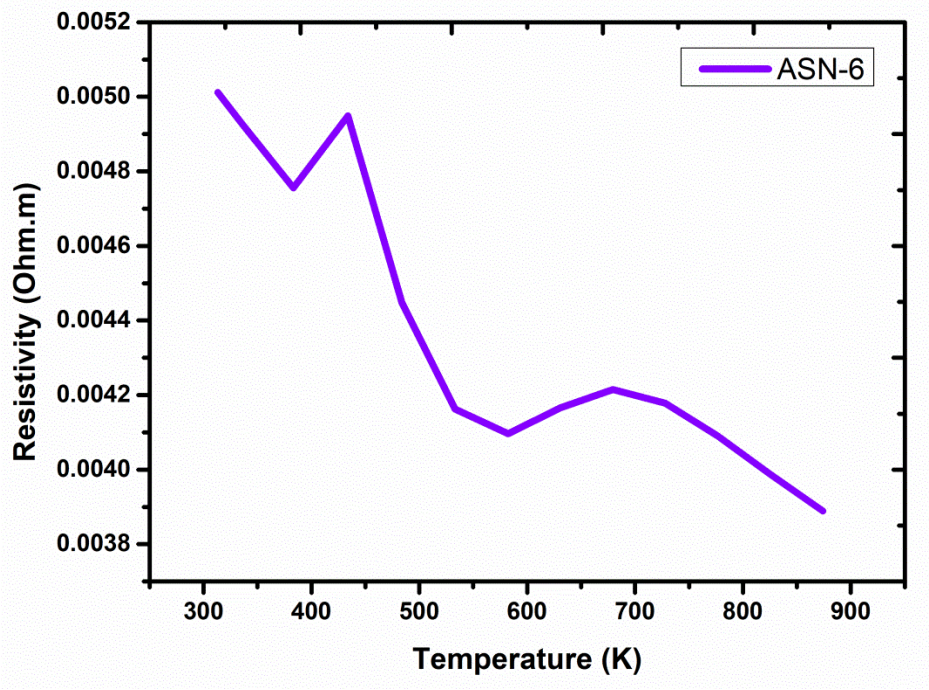

Figure 7.4. Resistivity of ASN-6 at variable temperature.

Chapter 8

Conclusion and future scope of work

The following conclusions could be made from the present study:

1. Raman spectra, microstructural and XRD analyses of AlN-SWCNT nanocomposites show that the SWCNT is chemically compatible with AlN matrix and retain its structure even at high temperature processing under nitrogen atmosphere during consolidation by hot pressing.

2. SWCNT helps densification of the material primarily by inhibiting the grain growth of AlN.

3. FESEM micrographs and TEM images show good dispersion of SWCNTs in AlN matrix confirm the presence of networks and 3D connectivities in web like structures in the mat of SWCNTs surrounding the grains in the polycrystalline AlN composites leading to the increase in electrical conductivity, negative permittivity and fracture toughness (K_{IC}).

4. A decrease in (a) the hardness due to high compressibility of the tubes and (b) thermal conductivity values due to Kapitza resistances between ceramic grain-nanotube interface and nanotube-nanotube interfaces are on the downside of the results.

5. High electrical conductivity of the composite is due to the presence of metallic character of the nanotubes identified by the invariable conduction with temperature when the content of the SWCNTs increases to 6vol%, thus, deviating from variable range hopping to fluctuation induced tunneling mechanism.

6. Thus, a high electrical and thermal conducting AlN-SWCNT composite ceramics could be prepared by hot pressing method. The material has the potential for applications in several mechanical, electrical and electronic devices. Plasma like tunable negative permittivity is a key attractive feature observed in these nanocomposites characteristic of random metamaterials and should have different sensing and electromagnetic shielding applications.

Future Work Scopes

- Attempts should be made to disperse the SWCNTs more uniformly and incorporate more SWCNTs (>6 vol%) in the composites and compare the properties.
- Tribological properties and EDM machinability of the composites are needed to be carried out.
- Compatibility with biological systems are needed to be observed for application biomedical engineering.
- High strain rate deformation characteristics of the composites are needed to be carried out in future since damage tolerant indentation could be observed during the hardness testing of the material and high elastic deformation of SWCNT reported recently in the literature.

References

[1] G.A. Slack, Nonmetallic crystals with high thermal conductivity, J. Phys. Chem. Solids. 34 (1973) 321–335. doi:10.1016/0022-3697(73)90092-9.

[2] L.M. Sheppard, Aluminum nitride. A versatile but challenging material, Am. Ceram. Soc. Bull. (1990).

[3] M.J. Pawar, A. Patnaik, S.K. Biswas, U. Pandel, I.K. Bhat, S. Chatterjee, A.K. Mukhopadhyay, R. Banerjee, B.P. Babu, Comparison of ballistic performances of Al_2O_3 and AlN ceramics, Int. J. Impact Eng. 98 (2016) 42–51.

[4] S. Burkhardt, R. Riedel, G. Müller, Processing and properties of AlN matrix composite ceramics containing dispersed hard materials, J. Eur. Ceram. Soc. 17 (1997) 3–12.

[5] O. Sbaizero, G. Pezzotti, Residual stresses and R-curve behavior of AlN/Mo composite, J. Eur. Ceram. Soc. 21 (2001) 269–275.

[6] M. Tajika, H. Matsubara, W. Rafaniello, Microstructures and properties in aluminum nitride–titanium nitride composite ceramics, Mater. Lett. 41 (1999) 139–144.

[7] H.A. Toutanji, D. Friel, T. El-Korchi, R.N. Katz, G. Wechsler, W. Rafaniello, Room temperature tensile and flexural strength of ceramics in AlN-SiC system, J. Eur. Ceram. Soc. 15 (1995) 425–434.

[8] S.M. Olhero, S. Novak, M. Oliveira, K. Krnel, T. Kosmac, J.M.F. Ferreira, A thermo-chemical surface treatment of AlN powder for the aqueous processing of AlN ceramics, J. Mater. Res. 19 (2004) 746–751.

[9] M.P. Thompson, G.W. Auner, T.S. Zheleva, K.A. Jones, S.J. Simko, J.N. Hilfiker, Deposition factors and band gap of zinc-blende AlN, J. Appl. Phys. 89 (2001) 3331–3336.

[10] M.M.J. Treacy, T.W. Ebbesen, J.M. Gibson, Exceptionally high Young's modulus observed for individual carbon nanotubes, Nature. 381 (1996) 678.

[11] M.-F. Yu, B.S. Files, S. Arepalli, R.S. Ruoff, Tensile loading of ropes of single wall carbon nanotubes and their mechanical properties, Phys. Rev. Lett. 84 (2000) 5552.

[12] Y. Ando, X. Zhao, H. Shimoyama, G. Sakai, K. Kaneto, Physical properties of multiwalled carbon nanotubes, Int. J. Inorg. Mater. 1 (1999) 77–82.

[13] A. Thess, R. Lee, P. Nikolaev, H. Dai, P. Petit, J. Robert, C. Xu, Y.H. Lee,

S.G. Kim, A.G. Rinzler, D.T. Colbert, G.E. Scuseria, D. Tomanek, J.E. Fischer, R.E. Smalley, Crystalline Ropes of Metallic Carbon Nanotubes, Science (80-.). 273 (1996) 483–487. doi:10.1126/science.273.5274.483.

[14] R.H. Baughman, A.A. Zakhidov, W.A. De Heer, Carbon nanotubes--the route toward applications, Science (80-.). 297 (2002) 787–792.

[15] M.J. Biercuk, M.C. Llaguno, M. Radosavljevic, J.K. Hyun, A.T. Johnson, J.E. Fischer, Carbon nanotube composites for thermal management, Appl. Phys. Lett. 80 (2002) 2767–2769.

[16] E. Zapata-Solvas, D. Gómez-García, A. Domínguez-Rodríguez, Towards physical properties tailoring of carbon nanotubes-reinforced ceramic matrix composites, J. Eur. Ceram. Soc. 32 (2012) 3001–3020. doi:10.1016/j.jeurceramsoc.2012.04.018.

[17] G.. Zhan, A.K. Mukherjee, Carbon nanotube reinforced alumina-based ceramics with novel mechanical, electrical, and thermal properties, Int. J. Appl. Ceram. Technol. (2004). doi:10.1111/j.1744-7402.2004.tb00166.x.

[18] S. Berber, Y.-K. Kwon, D. Tománek, Unusually high thermal conductivity of carbon nanotubes, Phys. Rev. Lett. 84 (2000) 4613.

[19] E. Bekyarova, M.E. Itkis, N. Cabrera, B. Zhao, A. Yu, J. Gao, R.C. Haddon, Electronic properties of single-walled carbon nanotube networks, J. Am. Chem. Soc. (2005). doi:10.1021/ja043153l.

[20] F. Li, H.M. Cheng, S. Bai, G. Su, M.S. Dresselhaus, Tensile strength of single-walled carbon nanotubes directly measured from their macroscopic ropes, Appl. Phys. Lett. (2000). doi:10.1063/1.1324984.

[21] A. Meyer-Plath, G. Orts-Gil, S. Petrov, F. Oleszak, H.E. Maneck, I. Dörfel, O. Haase, S. Richter, R. MacH, Plasma-thermal purification and annealing of carbon nanotubes, Carbon N. Y. (2012). doi:10.1016/j.carbon.2012.04.049.

[22] Y. Maeda, S. Kimura, M. Kanda, Y. Hirashima, T. Hasegawa, T. Wakahara, Y. Lian, T. Nakahodo, T. Tsuchiya, T. Akasaka, Large-scale separation of metallic and semiconducting single-walled carbon nanotubes, J. Am. Chem. Soc. 127 (2005) 10287–10290.

[23] S. Frank, P. Poncharal, Z.L. Wang, W.A. De Heer, Carbon nanotube quantum resistors, Science (80-.). (1998). doi:10.1126/science.280.5370.1744.

[24] O. Hilt, H.B. Brom, M. Ahlskog, Localized and delocalized charge transport in single-wall carbon-nanotube mats, Phys. Rev. B. 61 (2000) R5129.

[25] S.A. Hodge, M.K. Bayazit, K.S. Coleman, M.S.P. Shaffer, Unweaving the rainbow: a review of the relationship between single-walled carbon nanotube molecular structures and their chemical reactivity, Chem. Soc. Rev. 41 (2012) 4409–4429.

[26] D. V Matthew, Advanced materials and powders handbook. Aluminium Nitride(AlN), Am. Ceram. Soc. Bull. 78 (1999) 69–71.

[27] J.A. Kohn, P.G. Cotter, R.A. Potter, Synthesis of aluminum nitride monocrystals, (1956).

[28] G.A. Slack, S.F. Bartram, Thermal expansion of some diamondlike crystals, J. Appl. Phys. 46 (1975) 89–98. doi:10.1063/1.321373.

[29] P.J. Rutkowski, D. Kata, Thermal properties of AlN polycrystals obtained by pulse plasma sintering method, J. Adv. Ceram. 2 (2013) 180–184. doi:10.1007/s40145-013-0059-8.

[30] R. Hahn, V. Glaw, A. Ginolas, M. Töpfer, K. Wittke, H. Reichl, High performance liquid cooled aluminium nitride heat sinks, Microelectron. Int. 16 (1999) 21–26. doi:10.1108/13565369910250050.

[31] J.P. Freedman, J.H. Leach, E.A. Preble, Z. Sitar, R.F. Davis, J.A. Malen, Universal phonon mean free path spectra in crystalline semiconductors at high temperature, Sci. Rep. 3 (2013). doi:10.1038/srep02963.

[32] R. Kato, J. Hama, First-principles calculation of the elastic stiffness tensor of aluminium nitride under high pressure, J. Phys. Condens. Matter. 6 (1999) 7617–7632. doi:10.1088/0953-8984/6/38/004.

[33] M. Radwan, Y. Miyamoto, Self-propagating high-temperature synthesis of AlN nanostructures and their sintering properties, TRANSACTIONS-JWRI. 35 (2006) 43–46. http://www.jwri.osaka-u.ac.jp/publication/trans-jwri/pdf/352-08.pdf.

[34] G.A. Jeffrey, G.S. Parry, R.L. Mozzi, Study of the wurtzite-type binary compounds. I.*Structures of aluminum nitride and beryllium oxide, J. Chem. Phys. 25 (1956) 1024–1031. doi:10.1063/1.1743091.

[35] R. Kato, J. Hama, G.A. Slack, S.F. Bartram, P.J. Rutkowski, D. Kata, S. Loughin, R. French, W. Ching, G.A. Jeffrey, G.S. Parry, D.P. Dandekar, A. Abbate, J. Frankel, G.A. Slack, R. Hahn, V. Glaw, A. Ginolas, M. Töpfer, K. Wittke, H. Reichl, G.A. Jeffrey, G.S. Parry, R.L. Mozzi, A.R.L. Mozzlt, M. Radwan, Y. Miyamoto, J.P. Freedman, J.H. Leach, E.A. Preble, Z. Sitar, R.F.

Davis, J.A. Malen, P. Handbook, A. Geuther, Crystal Structure of Aluminum Nitride, J. Appl. Phys. 25 (1999) 21–26. doi:10.1063/1.1600519.

[36] D.P. Dandekar, A. Abbate, J. Frankel, Equation of state of aluminum nitride and its shock response, J. Appl. Phys. 76 (1994) 4077–4085. doi:10.1063/1.357357.

[37] R. Mukhopadhyay, Study on Sintering of Aluminum Nitride Compacts, Ph.D.(Tech) Thesis, University of Culcutta, 2005.

[38] X. Fu, Aluminum Nitride Wide Band-gap Semiconductor and Its Basic Characteristics, in: 6th Int. Conf. Electron. Mech. Inf. Manag. Soc., Atlantis Press, 2016.

[39] M. Ramisetty, S. Sastri, U. Kashalikar, Manufacturing of aluminum nitride powder for advanced applications, Am. Ceram. Soc. Bull. 93 (2014) 28–31.

[40] W. Callister, D. Rethwisch, Materials science and engineering: an introduction, 2007. doi:10.1016/0025-5416(87)90343-0.

[41] T.B. Troczynski, P.S. Nicholson, Effect of Additives on the Pressureless Sintering of Aluminum Nitride between 1500o and 1800oC, J. Am. Ceram. Soc. 72 (1989) 1488–1491. doi:10.1111/j.1151-2916.1989.tb07684.x.

[42] A.W. Weimer, G.A. Cochran, G.A. Eisman, J.P. Henley, B.D. Hook, L.K. Mills, T.A. Guiton, A.K. Knudsen, N.R. Nicholas, J.E. Volmering, W.G. Moore, Rapid Process for Manufacturing Aluminum Nitride Powder, J. Am. Ceram. Soc. 77 (1994) 3–18. doi:10.1111/j.1151-2916.1994.tb06951.x.

[43] P.E.J.E. Evans, United States Patent (19) Best Available Copy Date of Patent :, (1985).

[44] T.B. Jackson, A. V Virkar, K.L. More, R.B. Dinwiddie Jr, R.A. Cutler, High-thermal-conductivity aluminum nitride ceramics: the effect of thermodynamic, kinetic, and microstructural factors, J. Am. Ceram. Soc. 80 (1997) 1421–1435.

[45] M.N. Rahaman, Ceramic processing and sintering, CRC press, 2003.

[46] S. Iijima, Helical microtubules of graphitic carbon, Nature. 354 (1991) 56–58. doi:10.1038/354056a0.

[47] P.M. Ajayan, Nanotubes from Carbon, Chem. Rev. 99 (1999) 1787–1800. doi:10.1021/cr970102g.

[48] S. Mallakpour, E. Khadem, Carbon nanotube–metal oxide nanocomposites: Fabrication, properties and applications, Chem. Eng. J. 302 (2016) 344–367.

[49] D. Qian, G.J. Wagner, W.K. Liu, M.-F. Yu, R.S. Ruoff, Mechanics of carbon

nanotubes, Appl. Mech. Rev. 55 (2002) 495–533.

[50] R. Saito, G. Dresselhaus, M.S. Dresselhaus, Magnetic energy bands of carbon nanotubes, Phys. Rev. B. 50 (1994) 14698.

[51] N. Hamada, S. Sawada, A. Oshiyama, New one-dimensional conductors: graphitic microtubules, Phys. Rev. Lett. 68 (1992) 1579.

[52] C. Kittel, P. McEuen, P. McEuen, Introduction to solid state physics, Wiley New York, 1996.

[53] J.W. Mintmire, B.I. Dunlap, C.T. White, Are fullerene tubules metallic?, Phys. Rev. Lett. 68 (1992) 631.

[54] D.J. Hornbaker, Electronic structure of carbon nanotube systems measured with scanning tunneling microscopy, University of Illinois at Urbana-Champaign, 2003.

[55] L. Langer, L. Stockman, J.P. Heremans, V. Bayot, C.H. Olk, C. Van Haesendonck, Y. Bruynseraede, J.-P. Issi, Electrical resistance of a carbon nanotube bundle, J. Mater. Res. 9 (1994) 927–932.

[56] P.G. Collins, P. Avouris, The electronic properties of carbon nanotubes, Contemp. Concepts Condens. Matter Sci. 3 (2008) 49–81.

[57] P.R. Bandaru, Electrical Properties and Applications of Carbon Nanotube Structures, J. Nanosci. Nanotechnol. 7 (2007) 1239–1267. doi:10.1166/jnn.2007.307.

[58] J.W.G. Wilder, L.C. Venema, A.G. Rinzler, R.E. Smalley, C. Dekker, Electronic structure of atomically resolved carbon nanotubes, Nature. 391 (1998) 59.

[59] T.W. Odom, J.-L. Huang, P. Kim, C.M. Lieber, Atomic structure and electronic properties of single-walled carbon nanotubes, Nature. 391 (1998) 62.

[60] G. Gao, T. Cagin, W.A. Goddard III, Energetics, structure, mechanical and vibrational properties of single-walled carbon nanotubes, Nanotechnology. 9 (1998) 184.

[61] A. Krishnan, E. Dujardin, T.W. Ebbesen, P.N. Yianilos, M.M.J. Treacy, Young's modulus of single-walled nanotubes, Phys. Rev. B. 58 (1998) 14013.

[62] E. Hernández, A. Rubio, Nanotubes: Mechanical and Spectroscopic Properties, Sci. Highlight Mon. 4 (1999) 20–23.

[63] P.F. Schewe, B. Stein, J. Riordon, Physics news update, Am. Inst. Phys. Bull. Phys. News. 279 (1996).

[64] P. Avouris, a nanotube researcher at the IBM labs, Lect. given Michigan State Univ. (2000).

[65] A.F. Ávila, G.S.R. Lacerda, Molecular mechanics applied to single-walled carbon nanotubes, Mater. Res. 11 (2008) 325–333.

[66] H. Dai, A. Javey, E. Pop, D. Mann, W. Kim, Y. Lu, Electrical transport properties and field effect transistors of carbon nanotubes, Nano. 1 (2006) 1–13.

[67] V. Skákalová, A.B. Kaiser, Y.-S. Woo, S. Roth, Electronic transport in carbon nanotubes: From individual nanotubes to thin and thick networks, Phys. Rev. B. 74 (2006) 85403.

[68] A. Javey, J. Guo, Q. Wang, M. Lundstrom, H. Dai, Ballistic carbon nanotube field-effect transistors, Nature. 424 (2003) 654.

[69] S.J. Tans, M.H. Devoret, H. Dai, A. Thess, R.E. Smalley, L.J. Geerligs, C. Dekker, Individual single-wall carbon nanotubes as quantum wires, Nature. 386 (1997) 474.

[70] A.A. Balandin, Thermal properties of graphene and nanostructured carbon materials, Nat. Mater. 10 (2011) 569.

[71] P. Kim, L. Shi, A. Majumdar, P.L. Mceuen, Thermal Transport Measurements of Individual Multiwalled Nanotubes, (2001) 19–22. doi:10.1103/PhysRevLett.87.215502.

[72] Thermal Conductivity, (n.d.). http://hyperphysics.phy-astr.gsu.edu/hbase/Tables/thrcn.html (accessed February 16, 2019).

[73] A.M. Marconnet, M.A. Panzer, K.E. Goodson, Thermal conduction phenomena in carbon nanotubes and related nanostructured materials, Rev. Mod. Phys. 85 (2013) 1295.

[74] S. Bhattacharya, R. Amalraj, S. Mahapatra, Physics-based thermal conductivity model for metallic single-walled carbon nanotube interconnects, IEEE Electron Device Lett. 32 (2011) 203–205.

[75] E. Pop, D. Mann, Q. Wang, K. Goodson, H. Dai, Thermal conductance of an individual single-wall carbon nanotube above room temperature, Nano Lett. 6 (2006) 96–100.

[76] M.C.H. Wu, J.-Y. Hsu, Thermal conductivity of carbon nanotubes with quantum correction via heat capacity, Nanotechnology. 20 (2009) 145401.

[77] M. Fujii, X. Zhang, H. Xie, H. Ago, K. Takahashi, T. Ikuta, H. Abe, T.

Shimizu, Measuring the thermal conductivity of a single carbon nanotube, Phys. Rev. Lett. 95 (2005) 65502.

[78] T.-W. Chou, E.T. Thostenson, Z. Ren, Recent Advancements in Carbon Nanotubes and Their Composites, Society of Manufacturing Engineers, 2000.

[79] M. Piao, M.-K. Joo, J. Na, Y.-J. Kim, M. Mouis, G. Ghibaudo, S. Roth, W.-Y. Kim, H.-K. Jang, G.P. Kennedy, Effect of intertube junctions on the thermoelectric power of monodispersed single walled carbon nanotube networks, J. Phys. Chem. C. 118 (2014) 26454–26461.

[80] A. Mukhopadhyay, B.T.T. Chu, M.L.H. Green, R.I. Todd, Understanding the mechanical reinforcement of uniformly dispersed multiwalled carbon nanotubes in alumino-borosilicate glass ceramic, Acta Mater. 58 (2010) 2685–2697.

[81] G. Lin Hwang, K. Chu Hwang, Carbon nanotube reinforced ceramics, J. Mater. Chem. 11 (2001) 1722–1725. doi:10.1039/b101294k.

[82] Y. Morisada, Y. Miyamoto, Y. Takaura, K. Hirota, N. Tamari, Mechanical properties of SiC composites incorporating SiC-coated multi-walled carbon nanotubes, Int. J. Refract. Met. Hard Mater. 25 (2007) 322–327. doi:10.1016/j.ijrmhm.2006.08.005.

[83] V.M. Candelario, R. Moreno, Z. Shen, F. Guiberteau, A.L. Ortiz, Liquid-phase assisted spark-plasma sintering of SiC nanoceramics and their nanocomposites with carbon nanotubes, J. Eur. Ceram. Soc. 37 (2017) 1929–1936. doi:10.1016/j.jeurceramsoc.2016.12.050.

[84] P. Chen, S. Jing, Y. Chu, P. Rao, Improved fracture toughness of CNTs/SiC composites by HF treatment, J. Alloys Compd. 730 (2018) 42–46. doi:10.1016/j.jallcom.2017.09.265.

[85] N. Saheb, K. Mohammad, Microstructure and mechanical properties of spark plasma sintered Al2O3-SiC-CNTs hybrid nanocomposites, Ceram. Int. 42 (2016) 12330–12340. doi:10.1016/j.ceramint.2016.05.005.

[86] D. Jiang, K. Thomson, J.D. Kuntz, J.W. Ager, A.K. Mukherjee, Effect of sintering temperature on a single-wall carbon nanotube-toughened alumina-based nanocomposite, Scr. Mater. 56 (2007) 959–962. doi:10.1016/j.scriptamat.2007.02.007.

[87] J.H. Shin, J. Choi, M. Kim, S.H. Hong, Comparative study on carbon nanotube- and reduced graphene oxide-reinforced alumina ceramic composites,

Ceram. Int. 44 (2018) 8350–8357. doi:10.1016/j.ceramint.2018.02.024.

[88] O.S. Asiq Rahman, M. Sribalaji, B. Mukherjee, T. Laha, A.K. Keshri, Synergistic effect of hybrid carbon nanotube and graphene nanoplatelets reinforcement on processing, microstructure, interfacial stress and mechanical properties of Al2O3nanocomposites, Ceram. Int. 44 (2018) 2109–2122. doi:10.1016/j.ceramint.2017.10.160.

[89] M.H. Bocanegra-Bernal, C. Dominguez-Rios, J. Echeberria, A. Reyes-Rojas, A. Garcia-Reyes, A. Aguilar-Elguezabal, Spark plasma sintering of multi-, single/double- and single-walled carbon nanotube-reinforced alumina composites: Is it justifiable the effort to reinforce them?, Ceram. Int. 42 (2016) 2054–2062. doi:10.1016/j.ceramint.2015.09.060.

[90] A. Kasperski, A. Weibel, C. Estournès, C. Laurent, A. Peigney, Preparation-microstructure-property relationships in double-walled carbon nanotubes/alumina composites, Carbon N. Y. 53 (2013) 62–72. doi:10.1016/j.carbon.2012.10.030.

[91] G.D. Zhan, J.D. Kuntz, J. Wan, A.K. Mukherjee, Single-wall carbon nanotubes as attractive toughening agents in alumina-based nanocomposites, Nat. Mater. 2 (2003) 38–42. doi:10.1038/nmat793.

[92] S.C. Zhang, W.G. Fahrenholtz, G.E. Hilmas, E.J. Yadlowsky, Pressureless sintering of carbon nanotube–Al2O3 composites, J. Eur. Ceram. Soc. 30 (2010) 1373–1380. doi:10.1016/J.JEURCERAMSOC.2009.12.005.

[93] T. Zhang, L. Kumari, G.H. Du, W.Z. Li, Q.W. Wang, K. Balani, A. Agarwal, Mechanical properties of carbon nanotube–alumina nanocomposites synthesized by chemical vapor deposition and spark plasma sintering, Compos. Part A Appl. Sci. Manuf. 40 (2009) 86–93.

[94] M. Sribalaji, B. Mukherjee, A. Islam, A. Kumar Keshri, Microstructural and mechanical behavior of spark plasma sintered titanium carbide with hybrid reinforcement of tungsten carbide and carbon nanotubes, Mater. Sci. Eng. A. 702 (2017) 10–21. doi:10.1016/j.msea.2017.06.108.

[95] R. Poyato, A. Gallardo-López, F. Gutiérrez-Mora, A. Morales-Rodríguez, A. Muñoz, A. Domínguez-Rodríguez, Effect of high SWNT content on the room temperature mechanical properties of fully dense 3YTZP/SWNT composites, J. Eur. Ceram. Soc. 34 (2014) 1571–1579.

[96] A. Gallardo-López, A. Morales-Rodríguez, J. Vega-Padillo, R. Poyato, A.

Muñoz, A. Domínguez-Rodríguez, Enhanced carbon nanotube dispersion in 3YTZP/SWNTs composites and its effect on room temperature mechanical and electrical properties, J. Alloys Compd. 682 (2016) 70–79. doi:10.1016/j.jallcom.2016.04.262.

[97] J. Yi, W. Xue, T. Wang, Z. Xie, Mechanical and electrical properties of chemically modified MWCNTs/3Y-TZP composites, Ceram. Int. 41 (2015) 9157–9162. doi:10.1016/j.ceramint.2015.03.008.

[98] J. Lin, Y. Huang, H. Zhang, Y. Yang, N. Li, Microstructure and mechanical properties of spark plasma sintered ZrB2-SiC-MWCNT composites, Ceram. Int. 41 (2015) 15261–15265. doi:10.1016/j.ceramint.2015.07.207.

[99] C.Y. Tian, H. Jiang, Preparation and mechanical properties of carbon nanotube-silicon nitride nano-ceramic matrix composites, IOP Conf. Ser. Mater. Sci. Eng. 292 (2018) 012076. doi:10.1088/1757-899X/292/1/012076.

[100] M.I. Osendi, F. Gautheron, P. Miranzo, M. Belmonte, Dense and homogenous silicon nitride composites containing carbon nanotubes, J. Nanosci. Nanotechnol. 9 (2009) 6188–6194.

[101] T. Cao, X. Li, J. Li, M. Zhang, H. Qiu, Effect of sintering temperature on phase constitution and mechanical properties of WC-1.0 wt% carbon nanotube composites, Ceram. Int. 44 (2018) 164–169. doi:10.1016/j.ceramint.2017.09.154.

[102] N. Liao, D. Jia, Z. Yang, Y. Zhou, Y. Li, X. Jia, Strengthening and toughening effects of MWCNTs on Si2BC3N ceramics sintered by SPS technique, Mater. Sci. Eng. A. 710 (2018) 142–150. doi:10.1016/j.msea.2017.10.089.

[103] J. Lin, Y. Yang, H. Zhang, J. Gong, Effects of CNTs content on the microstructure and mechanical properties of spark plasma sintered TiB2-SiC ceramics, Ceram. Int. 43 (2017) 1284–1289. doi:10.1016/j.ceramint.2016.10.078.

[104] M. Mazaheri, D. Mari, Z.R. Hesabi, R. Schaller, G. Fantozzi, Multi-walled carbon nanotube/nanostructured zirconia composites: Outstanding mechanical properties in a wide range of temperature, Compos. Sci. Technol. 71 (2011) 939–945.

[105] G.D. Zhan, J.D. Kuntz, J. Wan, A.K. Mukherjee, Single-wall carbon nanotubes as attractive toughening agents in alumina-based nanocomposites, Nat. Mater. 2 (2003) 38–42. doi:10.1038/nmat793.

[106] R.Z. Ma, J. Wu, B.Q. Wei, J. Liang, D.H. Wu, Processing and properties of carbon nanotubes–nano-SiC ceramic, J. Mater. Sci. 33 (1998) 5243–5246.

[107] E. Flahaut, A. Peigney, C. Laurent, C. Marlière, F. Chastel, A. Rousset, Carbon nanotube-metal-oxide nanocomposites: Microstructure, electrical conductivity and mechanical properties, Acta Mater. 48 (2000) 3803–3812. doi:10.1016/S1359-6454(00)00147-6.

[108] A. Peigney, C. Laurent, F. Dobigeon, A. Rousset, Carbon nanotubes grown in situ by a novel catalytic method, J. Mater. Res. 12 (1997) 613–615.

[109] J. González-Julián, Y. Iglesias, A.C. Caballero, M. Belmonte, L. Garzón, C. Ocal, P. Miranzo, M.I. Osendi, Multi-scale electrical response of silicon nitride/multi-walled carbon nanotubes composites, Compos. Sci. Technol. 71 (2011) 60–66.

[110] J. Cho, F. Inam, M.J. Reece, Z. Chlup, I. Dlouhy, M.S.P. Shaffer, A.R. Boccaccini, Carbon nanotubes: do they toughen brittle matrices?, J. Mater. Sci. 46 (2011) 4770–4779.

[111] S. Dolati, A. Azarniya, A. Azarniya, H. Eslami-shahed, H.R.M. Hosseini, A. Simchi, Toughening mechanisms of SiC-bonded CNT bulk nanocomposites prepared by spark plasma sintering, Int. J. Refract. Met. Hard Mater. 71 (2018). doi:10.1016/j.ijrmhm.2017.10.024.

[112] N.P. Padture, Multifunctional Composites of Ceramics and Single-Walled Carbon Nanotubes, Adv. Mater. 21 (2009) 1767–1770.

[113] Y. Liu, C. Ramirez, L. Zhang, W. Wu, N.P. Padture, In situ direct observation of toughening in isotropic nanocomposites of alumina ceramic and multiwall carbon nanotubes, Acta Mater. 127 (2017) 203–210.

[114] E.L. Corral, H. Wang, J. Garay, Z. Munir, E. V. Barrera, Effect of single-walled carbon nanotubes on thermal and electrical properties of silicon nitride processed using spark plasma sintering, J. Eur. Ceram. Soc. 31 (2011) 391–400. doi:10.1016/j.jeurceramsoc.2010.10.020.

[115] D. Hanaoka, Y. Fukuzawa, C. Ramirez, P. Miranzo, M.I. Osendi, M. Belmonte, Electrical discharge machining of ceramic/carbon nanostructure composites, Procedia CIRP. 6 (2013) 95–100.

[116] D. Stauffer, A. Aharony, Introduction to Percolation Theory, (1994).

[117] S. Rul, F. Lefèvre-Schlick, E. Capria, C. Laurent, A. Peigney, Percolation of single-walled carbon nanotubes in ceramic matrix nanocomposites, Acta Mater.

52 (2004) 1061–1067. doi:10.1016/j.actamat.2003.10.038.

[118] G.D. Zhan, J.D. Kuntz, J.E. Garay, A.K. Mukherjee, Electrical properties of nanoceramics reinforced with ropes of single-walled carbon nanotubes, Appl. Phys. Lett. 83 (2003) 1228–1230. doi:10.1063/1.1600511.

[119] K. Ahmad, W. Pan, S. Shi, Electrical conductivity and dielectric properties of multiwalled carbon nanotube and alumina composites, Appl. Phys. Lett. 89 (2006) 133122. doi:10.1063/1.2357920.

[120] L.P. Rajukumar, M. Belmonte, J.E. Slimak, A.L. Elías, E. Cruz-Silva, N. Perea-Lõpez, A. Morelos-Gõmez, H. Terrones, M. Endo, P. Miranzo, M. Terrones, 3D Nanocomposites of Covalently Interconnected Multiwalled Carbon Nanotubes with SiC with Enhanced Thermal and Electrical Properties, Adv. Funct. Mater. 25 (2015) 4985–4993. doi:10.1002/adfm.201501696.

[121] G.D. Zhan, J.D. Kuntz, A.K. Mukherjee, P. Zhu, K. Koumoto, Thermoelectric properties of carbon nanotube/ceramic nanocomposites, Scr. Mater. 54 (2006) 77–82. doi:10.1016/j.scriptamat.2005.09.003.

[122] R. Poyato, J. Macías-Delgado, A. García-Valenzuela, Á. Gallardo-López, A. Morales-Rodríguez, A. Muñoz, A. Domínguez-Rodríguez, Mechanical and electrical properties of low SWNT content 3YTZP composites, J. Eur. Ceram. Soc. 35 (2015) 2351–2359.

[123] P. Hvizdoš, V. Puchý, A. Duszová, J. Dusza, C. Balázsi, Tribological and electrical properties of ceramic matrix composites with carbon nanotubes, Ceram. Int. 38 (2012) 5669–5676. doi:10.1016/j.ceramint.2012.04.010.

[124] N. Saheb, U. Hayat, Electrical conductivity and thermal properties of spark plasma sintered Al2O3-SiC-CNT hybrid nanocomposites, Ceram. Int. 43 (2017) 5715–5722. doi:10.1016/j.ceramint.2017.01.112.

[125] A.R. Boccaccini, B.J.C. Thomas, G. Brusatin, P. Colombo, Mechanical and electrical properties of hot-pressed borosilicate glass matrix composites containing multi-wall carbon nanotubes, J. Mater. Sci. 42 (2007) 2030–2036. doi:10.1007/s10853-006-0540-7.

[126] E.T. Thostenson, P.G. Karandikar, T.W. Chou, Fabrication and characterization of reaction bonded silicon carbide/carbon nanotube composites, J. Phys. D. Appl. Phys. 38 (2005) 3962–3965. doi:10.1088/0022-3727/38/21/020.

[127] T. Ukai, T. Sekino, A.T. Hirvonen, N. Tanaka, T. Kusunose, T. Nakayama, K. Niihara, Preparation and Electrical Properties of Carbon Nanotubes Dispersed

Zirconia Nanocomposites, Key Eng. Mater. 317–318 (2006) 661–664. doi:10.4028/www.scientific.net/KEM.317-318.661.

[128] A. Duszová, J. Dusza, K. Tomášek, G. Blugan, J. Kuebler, Microstructure and properties of carbon nanotube/zirconia composite, J. Eur. Ceram. Soc. 28 (2008) 1023–1027. doi:10.1016/j.jeurceramsoc.2007.09.011.

[129] S. Guo, R. Sivakumar, H. Kitazawa, Y. Kagawa, Electrical properties of silica-based nanocomposites with multiwall carbon nanotubes, J. Am. Ceram. Soc. 90 (2007) 1667–1670. doi:10.1111/j.1551-2916.2007.01636.x.

[130] C. Balázsi, B. Fényi, N. Hegman, Z. Kövér, F. Wéber, Z. Vértesy, Z. Kónya, I. Kiricsi, L.P. Biró, P. Arató, Development of CNT/Si3N4composites with improved mechanical and electrical properties, Compos. Part B Eng. 37 (2006) 418–424. doi:10.1016/j.compositesb.2006.02.006.

[131] J. Tatami, T. Katashima, K. Komeya, T. Meguro, T. Wakihara, Electrically conductive CNT-dispersed silicon nitride ceramics, J. Am. Ceram. Soc. 88 (2005) 2889–2893. doi:10.1111/j.1551-2916.2005.00539.x.

[132] P. Ge, K. Sun, A. Li, G. Pingji, Improving the electrical and microwave absorbing properties of Si3N4ceramics with carbon nanotube fibers, Ceram. Int. 44 (2018) 2727–2731. doi:10.1016/j.ceramint.2017.10.233.

[133] N. Sun, L.P.H. Jeurgens, Z. Burghard, J. Bill, Ionic liquid assisted fabrication of high performance SWNTs reinforced ceramic matrix nano-composites, Ceram. Int. 43 (2017) 2297–2304. doi:10.1016/j.ceramint.2016.11.013.

[134] B. Trawiński, B. Bochentyn, N. Gostkowska, M. Łapiński, T. Miruszewski, B. Kusz, Structure and thermoelectric properties of bismuth telluride—Carbon composites, Mater. Res. Bull. 99 (2018) 10–17. doi:10.1016/j.materresbull.2017.10.043.

[135] A. Mukhopadhyay, G. Otieno, B.T.T. Chu, A. Wallwork, M.L.H. Green, R.I. Todd, Thermal and electrical properties of aluminoborosilicate glass–ceramics containing multiwalled carbon nanotubes, Scr. Mater. 65 (2011) 408–411.

[136] R. Poyato, J. Macías-Delgado, A. Gallardo-López, A. Muñoz, A. Domínguez-Rodríguez, Microstructure and impedance spectroscopy of 3YTZP/SWNT ceramic nanocomposites, Ceram. Int. 41 (2015) 12861–12868.

[137] C. Cheng, R. Fan, Y. Ren, T. Ding, L. Qian, J. Guo, X. Li, L. An, Y. Lei, Y. Yin, Radio frequency negative permittivity in random carbon nanotubes/alumina nanocomposites, Nanoscale. 9 (2017) 5779–5787.

[138] R. Yin, Y. Zhang, W. Zhao, X. Huang, X. Li, L. Qian, Graphene platelets/aluminium nitride metacomposites with double percolation property of thermal and electrical conductivity, J. Eur. Ceram. Soc. 38 (2018) 4701–4706.

[139] R. Kubo, M. Toda, N. Hashitsume, Statistical physics II: Nonequilibrium stastical mechanics, 1991. doi:10.1007/BF01011313.

[140] J.L. Blackburn, A.J. Ferguson, C. Cho, J.C. Grunlan, Carbon-Nanotube-Based Thermoelectric Materials and Devices, Adv. Mater. 30 (2018) 1704386.

[141] J. Che, T. Cagin, W.A. Goddard III, Thermal conductivity of carbon nanotubes, Nanotechnology. 11 (2000) 65.

[142] B. Lanfant, Y. Leconte, N. Debski, G. Bonnefont, M. Pinault, M. Mayne-L'Hermite, A. Habert, Y. Jorand, V. Garnier, G. Fantozzi, S. Le Gallet, F. Bernard, Mechanical, thermal and electrical properties of nanostructured CNTs/SiC composites, Ceram. Int. 45 (2018) 2566–2575. doi:10.1016/j.ceramint.2018.10.187.

[143] J. Hu, S. Dong, B. Wu, X. Zhang, Z. Wang, H. Zhou, P. He, J. Yang, Q. Li, Mechanical and thermal properties of Cf/SiC composites reinforced with carbon nanotube grown in situ, Ceram. Int. 39 (2013) 3387–3391. doi:10.1016/J.CERAMINT.2012.08.072.

[144] N. Saheb, U. Hayat, Electrical conductivity and thermal properties of spark plasma sintered Al2O3-SiC-CNT hybrid nanocomposites, Ceram. Int. 43 (2017) 5715–5722. doi:10.1016/J.CERAMINT.2017.01.112.

[145] S. Kumar, D. Chaudhary, P. Kumar Dhawan, R.R. Yadav, N. Khare, Bi2Te3-MWCNT nanocomposite: An efficient thermoelectric material, Ceram. Int. 43 (2017) 14976–14982. doi:10.1016/j.ceramint.2017.08.017.

[146] K.T. Kim, S.Y. Choi, E.H. Shin, K.S. Moon, H.Y. Koo, G.-G. Lee, G.H. Ha, The influence of CNTs on the thermoelectric properties of a CNT/Bi2Te3 composite, Carbon N. Y. 52 (2013) 541–549. doi:10.1016/J.CARBON.2012.10.008.

[147] O. Hanzel, J. Sedláček, E. Hadzimová, P. Šajgalík, Thermal properties of alumina–MWCNTs composites, J. Eur. Ceram. Soc. 35 (2015) 1559–1567. doi:10.1016/J.JEURCERAMSOC.2014.11.032.

[148] K. Ahmad, P. Wei, C. Wan, Thermal conductivities of alumina-based multiwall carbon nanotube ceramic composites, J. Mater. Sci. 49 (2014) 6048–6055.

[149] S.R. Bakshi, K. Balani, A. Agarwal, Thermal conductivity of plasma-sprayed aluminum oxide - Multiwalled carbon nanotube composites, in: J. Am. Ceram. Soc., 2008. doi:10.1111/j.1551-2916.2007.02081.x.

[150] Q. Huang, L. Gab, Y. Liu, J. Sun, Sintering and thermal properties of multiwalled carbon nanotube-BaTiO3composites, J. Mater. Chem. 15 (2005) 1995–2001. doi:10.1039/b503444b.

[151] R. Sivakumar, S. Guo, T. Nishimura, Y. Kagawa, Thermal conductivity in multi-wall carbon nanotube/silica-based nanocomposites, Scr. Mater. 56 (2007) 265–268. doi:10.1016/j.scriptamat.2006.10.025.

[152] L. Jiang, L. Gao, Densified multiwalled carbon nanotubes – titanium nitride composites with enhanced thermal properties, 34 (2008) 231–235. doi:10.1016/j.ceramint.2006.09.011.

[153] T. Kobayashi, K. Yoshida, T. Yano, Microstructure, mechanical and thermal properties of B4C/CNT composites with Al additive, J. Nucl. Mater. 440 (2013) 524–529. doi:10.1016/J.JNUCMAT.2013.02.061.

[154] P. Miranzo, E. García, C. Ramírez, J. González-Julián, M. Belmonte, M.I. Osendi, Anisotropic thermal conductivity of silicon nitride ceramics containing carbon nanostructures, J. Eur. Ceram. Soc. 32 (2012) 1847–1854.

[155] P. Ge, Y. Cheng, K. Sun, Structure and performance of Si3N4/SiC/CNT composite fibres, Ceram. Int. (2019). doi:10.1016/J.CERAMINT.2019.03.099.

[156] J.-H. Pöhls, F. Schütt, C. O'Neill, S. Shree, M.B. Johnson, Y.K. Mishra, R. Adelung, M.A. White, Thermal and electrical transport properties in multi-walled carbon nanotube-coated ZnO tetrapods and self-entangled multi-walled carbon nanotube tubes, Carbon N. Y. 144 (2019) 423–432. doi:10.1016/J.CARBON.2018.12.047.

[157] C. Dreßler, R. Löhnert, J. Gonzalez-Julian, O. Guillon, J. Töpfer, S. Teichert, Effect of Carbon Nanotubes on Thermoelectric Properties in Zn 0.98 Al 0.02 O, J. Electron. Mater. 45 (2016) 1459–1463.

[158] W. Gao, H. Chai, F. Wu, X. Li, X. Hu, H. Song, Enhanced thermoelectric properties of CNT dispersed and Na-doped Bi2Ba2Co2Oy composites, Ceram. Int. 43 (2017) 5723–5727. doi:10.1016/J.CERAMINT.2017.01.113.

[159] S.K. Biswas, F.L. Riley, Gas pressure sintering of silicon nitride powder coated with Al2O3 and TiO2, J. Am. Ceram. Soc. 86 (2003) 212–216.

[160] S.K. Biswas, F.L. Riley, Gas pressure sintering of silicon nitride—current

status, Mater. Chem. Phys. 67 (2001) 175–179.

[161] M. Kumar, S. Yellampalli, Carbon Nanotubes–Synthesis, Characterization, Applications, Carbon Nanotub. Synth. Growth Mech. [Online]. (2011).

[162] H. Hu, B. Zhao, M.E. Itkis, R.C. Haddon, Nitric acid purification of single-walled carbon nanotubes, J. Phys. Chem. B. 107 (2003) 13838–13842.

[163] A. Chakravarty, S.K. Biswas, Enrichment of metallic single-walled carbon nanotubes with simultaneous purification by nitric acid treatment, Fullerenes Nanotub. Carbon Nanostructures. 23 (2015) 542–548. doi:10.1080/1536383X.2014.885955.

[164] J. de P. P.Atkins, Physical Chemistry, Oxford University Press, UK, 2002.

[165] Spectrum 100 User's guide Perkin Elmer, UK, (n.d.).

[166] Malvern instruments, M. Instruments, Malvern instruments, Zetasizer Nano Series User Manual, Dep. Biochem. Biophys. Facil. , Univ. Chambridge. (2004) 207. doi:10.1016/S0294-3506(99)80105-7.

[167] C.G. Salzmann, S.A. Llewellyn, G. Tobias, M.A.H. Ward, Y. Huh, M.L.H. Green, The role of carboxylated carbonaceous fragments in the functionalization and spectroscopy of a single-walled carbon-nanotube material, Adv. Mater. 19 (2007) 883–887.

[168] AIRIX, (n.d.). http://airix.jp/e/product/product02.html# (accessed February 13, 2019).

[169] Q. Lu, G. Keskar, R. Ciocan, R. Rao, R.B. Mathur, A.M. Rao, L.L. Larcom, Determination of carbon nanotube density by gradient sedimentation., J. Phys. Chem. B. 110 (2006) 24371–24376. doi:10.1021/jp063660k.

[170] B.D. Cullity, Elements of X-ray diffraction, 2nd edition, 1978. doi:10.1119/1.1934486.

[171] Bragg's Law, (n.d.). http://hyperphysics.phy-astr.gsu.edu/hbase/quantum/bragg.html (accessed February 18, 2019).

[172] D.V.S. Rao, K. Muraleedharan, C.J. Humphreys, TEM specimen preparation techniques, Microsc. Sci. Technol. Appl. Educ. (2010) 1232–1244.

[173] Argon ion polishing of focused ion beam specimens in PIPS II system | Gatan, Inc., (n.d.). http://www.gatan.com/argon-ion-polishing-focused-ion-beam-specimens-pips-ii-system (accessed February 20, 2019).

[174] K. Strecker, S. Ribeiro, M.-J. Hoffmann, Fracture toughness measurements of LPS-SiC: a comparison of the indentation technique and the SEVNB method,

Mater. Res. 8 (2005) 121–124.

[175] G.R. Antis, P. Chantikul, B.R.R. LAWN, M, G.R. ANSTIS, P. Chantikul, B.R.R. LAWN, D.B. MARSHALL, A Critical Evaluation of Indenation Techniques for Measuring Fracture Toughness: I, Direct Crack Measurements, J. Am. Ceram. Soc. 46 (1981) 533–538. doi:10.1111/j.1151-2916.1981.tb10320.x.

[176] J.W. An, D.-S. Lim, Effect of carbon nanotube additions on the microstructure of hot-pressed alumina, J. Ceram. Process. Res. 3 (2002) 201–204.

[177] F. Inam, H. Yan, T. Peijs, M.J. Reece, The sintering and grain growth behaviour of ceramic–carbon nanotube nanocomposites, Compos. Sci. Technol. 70 (2010) 947–952.

[178] B. Milsom, H. Porwal, G. Viola, Z. Gao, M.J. Reece, Understanding and quantification of grain growth mechanism in ZrO2-carbon nanotube composites, Mater. Des. (2017). doi:10.1016/j.matdes.2017.07.040.

[179] A. Jorio, A.G. Souza Filho, G. Dresselhaus, M.S. Dresselhaus, A.K. Swan, M.S. Ünlü, B.B. Goldberg, M.A. Pimenta, J.H. Hafner, C.M. Lieber, G-band resonant Raman study of 62 isolated single-wall carbon nanotubes, Phys. Rev. B. 65 (2002) 155412.

[180] A. Jorio, R. Saito, J.H. Hafner, C.M. Lieber, D.M. Hunter, T. McClure, G. Dresselhaus, M.S. Dresselhaus, Structural (n, m) determination of isolated single-wall carbon nanotubes by resonant Raman scattering, Phys. Rev. Lett. 86 (2001) 1118.

[181] F. Inam, H. Yan, T. Peijs, M.J. Reece, The sintering and grain growth behaviour of ceramic-carbon nanotube nanocomposites, Compos. Sci. Technol. 70 (2010) 947–952. doi:10.1016/j.compscitech.2010.02.010.

[182] P.S. de Baranda, A.K. Knudsen, E. Ruh, Effect of yttria on the thermal conductivity of aluminum nitride, J. Am. Ceram. Soc. 77 (1994) 1846–1850.

[183] Q. Li, Z. Wang, C. Wu, X. Cheng, Microstructure and mechanical properties of aluminum nitride co-doped with cerium oxide via hot-pressing sintering, J. Alloys Compd. 640 (2015) 275–279.

[184] K. Jankowski, P. Rutkowski, D. Kata, M. Rączka, M. Ziąbka, Microstructural analysis of aluminum nitride–GPLs composites, Ceram. Int. 42 (2016) 9025–9031.

[185] A. Chakravarty, R. Singh, S. Roy, U. Chowdhury, S. Basu, S.K. Biswas,

Aluminum nitride-single walled carbon nanotube nanocomposite with superior electrical and thermal conductivities, J. Am. Ceram. Soc. 100 (2017) 3360–3364. doi:10.1111/jace.14992.

[186] W.Y. Sun, Z.K. Huang, T.Y. Tien, T.S. Yen, Phase relationships in the system Y-A1-ON, Mater. Lett. 11 (1991) 67–69.

[187] M. Belmonte, S.M. Vega-Díaz, A. Morelos-Gómez, P. Miranzo, M.I. Osendi, M. Terrones, Nitrogen-doped-CNTs/Si3N4 nanocomposites with high electrical conductivity, J. Eur. Ceram. Soc. 34 (2014) 1097–1104.

[188] A.M. Zahedi, J. Gonzalez-Julian, M. Mazaheri, J. Javadpour, H.R. Rezaie, O. Guillon, Field-assisted/spark plasma sintering behavior of CNT-reinforced zirconia composites: A comparative study between model and experiments, J. Eur. Ceram. Soc. 35 (2015) 4241–4249.

[189] N.F. Mott, Conduction in non-crystalline materials, Philos. Mag. (1969). doi:10.1080/14786436908216338.

[190] H.M. Kim, M.S. Choi, J. Joo, S.J. Cho, H.S. Yoon, Complexity in charge transport for multiwalled carbon nanotube and poly(methyl methacrylate) composites, Phys. Rev. B - Condens. Matter Mater. Phys. (2006). doi:10.1103/PhysRevB.74.054202.

[191] D. Stauffer, Scaling theory of percolation clusters, Phys. Rep. (1979). doi:10.1016/0370-1573(79)90060-7.

[192] F.C. Fonseca, R. Muccillo, D.Z. de Florio, L.O. Ladeira, A.S. Ferlauto, Mixed ionic-electronic conductivity in yttria-stabilized zirconia/carbon nanotube composites, Appl. Phys. Lett. 91 (2007) 243107.

[193] A.B. Kaiser, V. Skakalova, Electronic conduction in polymers, carbon nanotubes and graphene, Chem. Soc. Rev. 40 (2011) 3786–3801.

[194] S. Ravi, A.B. Kaiser, C.W. Bumby, Improved conduction in transparent single walled carbon nanotube networks drop-cast from volatile amine dispersions, Chem. Phys. Lett. 496 (2010) 80–85.

[195] T. Hunger, B. Lengeler, J. Appenzeller, Transport in ropes of carbon nanotubes: Contact barriers and Luttinger liquid theory, Phys. Rev. B. 69 (2004) 195406.

[196] D. Halliday, R. Resnick, J. Walker, Fundamentals of physics extended, John Wiley & Sons, 2010.

[197] C. Cheng, K. Yan, R. Fan, L. Qian, Z. Zhang, K. Sun, M. Chen, Negative

permittivity behavior in the carbon/silicon nitride composites prepared by impregnation-carbonization approach, Carbon N. Y. 96 (2016) 678–684.

[198] Y. Xi, Y. Bin, C.K. Chiang, M. Matsuo, Dielectric effects on positive temperature coefficient composites of polyethylene and short carbon fibers, Carbon N. Y. 45 (2007) 1302–1309.

[199] S.A. Chowdhury, H.S. Maiti, S. Biswas, Synthesis of spherical Al2O3 and AlN powder from C@Al2O3 composite powder, J. Mater. Sci. 41 (2006) 4699–4705. doi:10.1007/s10853-006-0039-2.

[200] C.F. Cullis, J.G. Yates, Reaction of carbon with nitrogen, Trans. Faraday Soc. 60 (1964) 141–148. doi:10.1039/tf9646000141.

[201] K. Ahmad, W. Pan, Microstructure-toughening relation in alumina based multiwall carbon nanotube ceramic composites, J. Eur. Ceram. Soc. 35 (2015) 663–671. doi:10.1016/j.jeurceramsoc.2014.08.044.

[202] J. Shin, S. Hong, Microstructure and mechanical properties of single wall carbon nanotube reinforced yttria stabilized zircona ceramics, Mater. Sci. Eng. A. 556 (2012) 382–387. doi:10.1016/j.msea.2012.07.001.

[203] F. Inam, T. Peijs, M.J. Reece, The production of advanced fine-grained alumina by carbon nanotube addition, J. Eur. Ceram. Soc. 31 (2011) 2853–2859.

[204] M.H. Bocanegra-Bernal, J. Echeberria, J. Ollo, A. Garcia-Reyes, C. Dominguez-Rios, A. Reyes-Rojas, A. Aguilar-Elguezabal, A comparison of the effects of multi-wall and single-wall carbon nanotube additions on the properties of zirconia toughened alumina composites, Carbon N. Y. 49 (2011) 1599–1607.

[205] A. Kasperski, A. Weibel, D. Alkattan, C. Estournès, V. Turq, C. Laurent, A. Peigney, Microhardness and friction coefficient of multi-walled carbon nanotube-yttria-stabilized ZrO2 composites prepared by spark plasma sintering, Scr. Mater. 69 (2013) 338–341.

[206] E. Zapata-Solvas, R. Poyato, D. Gómez-García, A. Domínguez-Rodríguez, V. Radmilovic, N.P. Padture, Creep-resistant composites of alumina and single-wall carbon nanotubes, Appl. Phys. Lett. 92 (2008) 111912.

[207] X.-F. Wang, Z.-J. Xu, Z.-Y. Zhu, Reversible mechanical bistability of carbon nanotubes under radial compression, Chem. Phys. 334 (2007) 144–147.

[208] M.-F. Yu, T. Kowalewski, R.S. Ruoff, Investigation of the radial deformability

of individual carbon nanotubes under controlled indentation force, Phys. Rev. Lett. 85 (2000) 1456.

[209] Z.R. Abrams, Y. Hanein, Radial deformation measurements of isolated pairs of single-walled carbon nanotubes, Carbon N. Y. 45 (2007) 738–743. doi:10.1016/j.carbon.2006.11.024.

[210] E.O. Hall, The deformation and ageing of mild steel: III discussion of results, Proc. Phys. Soc. Sect. B. 64 (1951) 747.

[211] N.J. Petch, The cleavage strength of polycrystals, J. Iron Steel Inst. 174 (1953) 25–28.

[212] Z. Xia, L. Riester, W.A. Curtin, H. Li, B.W. Sheldon, J. Liang, B. Chang, J.M. Xu, Direct observation of toughening mechanisms in carbon nanotube ceramic matrix composites, Acta Mater. 52 (2004) 931–944.

[213] S.I. Cha, K.T. Kim, K.H. Lee, C.B. Mo, S.H. Hong, Strengthening and toughening of carbon nanotube reinforced alumina nanocomposite fabricated by molecular level mixing process, Scr. Mater. 53 (2005) 793–797.

[214] R.K. Chintapalli, F.G. Marro, B. Milsom, M. Reece, M. Anglada, Processing and characterization of high-density zirconia–carbon nanotube composites, Mater. Sci. Eng. A. 549 (2012) 50–59.

[215] H. Ichimaru, G. Pezzotti, Raman microprobe mapping of residual and bridging stress fields in AlN ceramics, Mater. Sci. Eng. A. 326 (2002) 261–269. doi:10.1016/S0921-5093(01)01525-8.

[216] G. Pezzotti, In situ study of fracture mechanisms in advanced ceramics using fluorescence and Raman microprobe spectroscopy, J. Raman Spectrosc. 30 (1999) 867–875. doi:10.1002/(sici)1097-4555(199910)30:10<867::aid-jrs466>3.0.co;2-0.

[217] W.J. Parker, R.J. Jenkins, C.P. Butler, G.L. Abbott, Flash method of determining thermal diffusivity, heat capacity, and thermal conductivity, J. Appl. Phys. (1961). doi:10.1063/1.1728417.

[218] S. Zhai, P. Zhang, Y. Xian, J. Zeng, B. Shi, Effective thermal conductivity of polymer composites: Theoretical models and simulation models, Int. J. Heat Mass Transf. 117 (2018) 358–374.

[219] L. Xue, P. Keblinski, S.R. Phillpot, S.-S. Choi, J.A. Eastman, Two regimes of thermal resistance at a liquid–solid interface, J. Chem. Phys. 118 (2003) 337–339.

[220] R. Kobayashi, J. Tatami, T. Wakihara, T. Meguro, K. Komeya, Temperature dependence of the electrical properties and seebeck coefficient of AlN–SiC ceramics, J. Am. Ceram. Soc. 89 (2006) 1295–1299.

[221] M.W. Barsoum, H.-I. Yoo, I.K. Polushina, V.Y. Rud, Y. V Rud, T. El-Raghy, Electrical conductivity, thermopower, and hall effect of Ti 3 AlC 2, Ti 4 AlN 3, and Ti 3 SiC 2, Phys. Rev. B. 62 (2000) 10194.

[222] E.E. Underwood, Quantitative stereology for microstructural analysis, in: Microstruct. Anal., Springer, 1973: pp. 35–66.

Appendix

Grain Size measurement

Grain sizes were measured from FESEM micrographs by using Image J software using lineal intercept method [222]. Procedure for image processing and measuring grain size is given below

a. To enhance the grain boundaries ion beam polishing were done using GATAN PIPS II instrument by calibrating the values of voltage and ion gun angle.

b. Grain boundary was enhanced by improving the image contrast and adjusting brightness between the neighbor regions.

c. Subtract background was used attain the same shading distribution at different picture region.

d. Shadow is used to clearly see the grain boundary and grains in the SEM image.

e. Grain size is measured by using linear intercept method.

f. We used Adobe Photoshop for drawing the grid and measuring the intersection point and no. of phases on a calibrated line. The technique gives not only the grain sizes of composites but also the porosity of the material and average pore sizes.

Average values of grain sizes (d_{50}) are presents in **Figure 6.3**

Average values of grain size are calculated as follows

$$\text{Average Grain size}(L0) = \pi\,(A_A)_\alpha/(L_A)_\alpha(\text{mm}) \tag{38}$$

$$(L_A)_\alpha = \pi\ N_L \tag{39}$$

$$\text{Average } P_L = 2\ X\ N_L \tag{40}$$

$$\text{Average } N_L = (\text{total } N_L)/(\text{total horizontal lines X length of a line}) \tag{41}$$

$$(V_V)_\alpha = (A_A)_\alpha = (L_L)_\alpha = (\text{total points on } \alpha \text{ phase})/(\text{total intersecting points}) \tag{42}$$

List of publications

- **R. Singh**, A. Chakravarty, S. Mishra, R.C. Prajapati, J. Dutta, I.K. Bhat, U. Pandel, S.K. Biswas, K. Muraleedharan, "AlN–SWCNT metacomposites having tunable negative permittivity in radio and microwave frequencies" *ACS Appl. Mater. Interfaces*. (2019). doi:10.1021/acsami.9b15909.

- **R.Singh**, A.Chakravarty, U.Chowdhury, D.Bhattacharya, S.K.Biswas, "Electrical conduction in aluminum nitride-single -walled carbon nanotube Nanocomposites" *Materials Letters* 215 (2018): 144-147.

- A.Chakravarty, **R.Singh**, S.Roy, U.Chowdhury, S.Basu, S.K.Biswas, "Aluminum nitride-single walled carbon nanotube nanocomposite with superior electrical and thermal conductivities" *J.Am.Ceram. Soc*.100 (2017) 3360-3364.

- **R.Singh**, A.Chakravarty, U.Pandel and S.K.Biswas "Microstructure and properties of AlN-SWCNT advanced ceramic composite" ORAL PRESENTATION at *ICAMEES 2018*.

- **R. Singh**, A.Chakravarty, U. Pandel, S.K. Biswas "Properties of AlN-SWCNT advance ceramic composite" selected for Poster presentation at 6th Nano Today Conference.